



THE HONG KONG
POLYTECHNIC UNIVERSITY

香港理工大學

Pao Yue-kong Library

包玉剛圖書館

Copyright Undertaking

This thesis is protected by copyright, with all rights reserved.

By reading and using the thesis, the reader understands and agrees to the following terms:

1. The reader will abide by the rules and legal ordinances governing copyright regarding the use of the thesis.
2. The reader will use the thesis for the purpose of research or private study only and not for distribution or further reproduction or any other purpose.
3. The reader agrees to indemnify and hold the University harmless from and against any loss, damage, cost, liability or expenses arising from copyright infringement or unauthorized usage.

IMPORTANT

If you have reasons to believe that any materials in this thesis are deemed not suitable to be distributed in this form, or a copyright owner having difficulty with the material being included in our database, please contact lbsys@polyu.edu.hk providing details. The Library will look into your claim and consider taking remedial action upon receipt of the written requests.

Pao Yue-kong Library, The Hong Kong Polytechnic University, Hung Hom, Kowloon, Hong Kong

<http://www.lib.polyu.edu.hk>

**ALL OPTICAL FIBER
PHOTOTHERMAL SPECTROSCOPIC
SENSORS FOR HIGH SENSITIVITY
GAS DETECTION**

TAN YANZHEN

Ph.D

The Hong Kong Polytechnic University

2018

The Hong Kong Polytechnic University

Department of Electrical Engineering

**ALL OPTICAL FIBER
PHOTOTHERMAL SPECTROSCOPIC
SENSORS FOR HIGH SENSITIVITY
GAS DETECTION**

TAN YANZHEN

A thesis submitted in partial fulfillment of the requirements for
the degree of *Doctor of Philosophy*

August 2017

CERTIFICATE OF ORIGINALITY

I hereby declare that this thesis is my own work and that, to the best of my knowledge and belief, it reproduces no material previously published or written, nor material that has been accepted for the award of any other degree or diploma, except where due acknowledgement has been made in the text.

..... (Signed)

.....TAN Yanzhen..... (Name of student)

Abstract

Detection of trace gases sensitively and selectively is of importance in many fields such as environmental monitoring, safety and industrial process control as well as national security applications. Laser absorption spectroscopy (LAS) is a powerful technique for trace gas detection with characteristics of high selectivity and sensitivity. Optical fiber-based technologies have been employed for trace gas detection due to the advantages of compact size, remote interrogation and sensor networking. However, the performance of direct absorption based optical fiber gas sensors, including those made of micro-optic lenses with fiber pigtails and solid or hollow core microstructured optical fibers, is limited to 1 to 10 parts-per-million (ppm).

The detection sensitivity of LAS sensors can be improved by using longer absorption cell. Using of a longer length of hollow-core photonic bandgap fiber (HC-PBF) as absorption cell could improve the detection sensitivity. However, it is very difficult to achieve parts-per-billion (ppb) level detection because it would require a very long length of HC-PBF (e.g., 100 meters). This will also make the sensor response extremely slow because of the very long time needed to fill gas sample into the hollow-core. So the current direct absorption gas sensors are difficult to achieve high sensitivity and fast response simultaneously.

In this thesis, we aim to investigate all optical fiber gas sensors based on photothermal (PT) spectroscopy which can achieve high sensitivity and fast response. PT spectroscopy is an alternative indirect method which can provide high sensitivity for gas detection. Trace gas detection based on photothermal effect has been investigated by many instrumental methods such as photoacoustic spectroscopy (PAS) and photothermal interferometry (PTI). These methods have demonstrated sub-ppb level detection sensitivity.

The basic process of the PAS involves the conversion of light absorption of the target gas into the acoustic pressure wave via the photoacoustic effect. The generated acoustic pressure wave can be detected by the acoustic detector which can achieve fast response. Here we propose a fiber Fabry-Perot (F-P) interferometer with graphene diaphragm as the acoustic detector. It is made by attaching a multilayer graphene diaphragm to a hollow cavity at the end of a single mode optical fiber. As an acoustic detector, its pressure and frequency responses are firstly investigated. By operating at one of the mechanical resonances of the diaphragm, the sensitivity for acoustic detection is enhanced and a noise equivalent minimum detectable pressure of $\sim 2 \mu\text{Pa}/\text{Hz}^{1/2}$ at ~ 10 kHz is demonstrated. To our knowledge, this is a very sensitive result since it is better than the commercial B&K4189 microphone ($\sim 8 \mu\text{Pa}/\text{Hz}^{1/2}$).

Then the acetylene detection by optical fiber photoacoustic gas sensor is demonstrated by using the proposed acoustic detector. A lower detection limit of ~ 120 ppb can be achieved when the modulation frequency is operating at one of the mechanical resonances of the diaphragm. Theoretical analysis shows that the detection sensitivity can be further improved by increasing the Q -factor of the resonator at low gas pressures.

In order to improve the detection sensitivity and achieve faster response, we also propose a novel resonating HC-PBF photonic microcell for high performance gas detection. This absorption cell is formed by jointing a piece of HC-PBF with two single mode fibers (SMFs) with mirrored ends, and light travels back and forth through the absorbing gas in the absorption cell and the effective absorption path length can be enhanced by a factor proportional to the cavity finesse. The finesse of a resonating absorption cell made with 6.75-cm-long HC-1550-06 fiber is measured to be 128, corresponding to an effective optical path length of ~ 5.5 m. So such a resonating gas cell enables us to use a shorter HC-PBF (e.g., a few to tens of centimeters) to achieve high

sensitivity, overcoming the problem of slow response associated with the use of long HC-PBF.

Gas detection experiments based on direct absorption with a resonating HC-PBF microcell are conducted. With a cavity length of 9.4 cm and a finesse of 68, a detection limit of 7 ppm can be achieved. Compared with a single-path non-resonating HC-PBF, the use of a resonating HC-PBF microcell can improve the detection sensitivity.

We also conduct cavity enhanced PT gas detection experiments with the resonating HC-PBF microcell. Experiments with a 6.2-cm-long resonating microcell with a finesse of 45 for pump beam and 41 for probe beam demonstrated a detection limit of 126 ppb acetylene, 1-2 orders of magnitude better than the same gas cell based on direct absorption. The cavity enhancement of such a resonating HC-PBF microcell can simultaneously amplify the intracavity build-up intensity for the pump beam inside the HC-PBF and improve the slope of the operating point for the probe beam by a factor proportional to the cavity finesse.

Publications

Journal articles

1. **Y. Tan**, W. Jin, F. Yang, Y. Qi, C. Zhang, Y. Lin, and H. L. Ho, "Hollow-core fiber-based high finesse resonating cavity for high sensitivity gas detection," *Journal of Lightwave Technology* **35**(14), 2887-2893 (2017).
2. **Y. Tan**, C. Zhang, W. Jin, F. Yang, H. L. Ho, and J. Ma, "Optical fiber photoacoustic gas sensor with graphene nano-mechanical resonator as the acoustic detector," *IEEE Journal of Selected Topics in Quantum Electronics*, **23**(2), 1-11 (2017).
3. F. Yang, **Y. Tan**, W. Jin, Y. Lin, Y. Qi, and H. L. Ho, "Hollow-core fiber Fabry-Perot photothermal gas sensor," *Optics letters*, **41**(13), 3025-3028 (2016).
4. Y. Lin, W. Jin, F. Yang, **Y. Tan**, and H. L. Ho, "Performance optimization of hollow-core fiber photothermal gas sensors," *Optics letters*, **42**(22), 4712-4715 (2017).
5. F. Yang, W. Jin, Y. Lin, C. Wang, H. L. Ho, and **Y. Tan**, "Hollow-core microstructured optical fiber gas sensors," *Journal of Lightwave Technology* **35**(16), 3413-3424 (2017).
6. Y. Lin, F. Liu, X. He, W. Jin, M. Zhang, F. Yang, H. L. Ho, **Y. Tan**, and L. Gu, "Distributed gas sensing with optical fibre photothermal interferometry," *Optics express*, **25**(25), 31568-31585 (2017).

Conference proceedings

1. **Y. Tan**, F. Yang, J. Ma, H. L. Ho and W. Jin, "All-fiber photoacoustic gas sensor with graphene nano-mechanical resonator as the acoustic detector," *Proc. SPIE 9634*, 24th International Conference on Optical Fibre Sensors (2015).
2. **Y. Tan**, W. Jin, F. Yang, and H. L. Ho, "High finesse hollow-core fiber resonating cavity for high sensitivity gas sensing application," *Proc. SPIE 10323*, 25th International Conference on Optical Fibre Sensors (2017).
3. C. Zhang, Y. Yang, **Y. Tan**, J. Ma, H. L. Ho, and W. Jin, "Multi-layer Graphene Diaphragm-based Fabry-Perot Interferometer for Acoustic Detection with Long Term Stability," In *Asia-Pacific Optical Sensors Conference*, Optical Society of America (2016).

Acknowledgements

I would like to express my deep gratitude to my supervisor, Professor Wei Jin, for his invaluable encouragement, support and suggestion during the past three years. His conscientious research attitude and insightful view set an excellent example for me in my academic research and my daily life. This attitude and spirit will also remain as precious asset to me in my future career. His patience and encouragement to the student also make us feel warm and full of positive energy.

Special thanks go to Dr. Fan Yang, Dr. Hoi Lut Ho, Dr. Jun Ma, Dr. Chao Wang and Dr. Wa Jin for your useful discussion and kindly help especially when I just started my PhD study.

I would also acknowledge Mr. Yuechuan Lin, Mr. Congzhe Zhang, Dr. Yiping Miao, Mr. Yun Qi, Mr. Yan Zhao, Mr. Haihong Bao, Dr. Haipeng Luo, and Mr. Pengcheng Zhao for your kindly help and support in my study and life.

Finally, I would give special gratitude to my beloved family. Their continuous support keeps encouraging me to move forward during my entire study period.

Table of contents

Abstract	I
Publications	IV
Acknowledgements	V
List of Figures	IX
List of Tables	XIX
List of Acronyms	XX
Chapter 1 Introduction	1
1.1 Background.....	1
1.1.1 Direct absorption optical fiber gas sensors	2
1.1.2 Photothermal spectroscopic optical fiber gas sensors.....	7
1.2 Motivation and significance of this work	14
1.3 Thesis outline	16
References of Chapter 1	18
Chapter 2 Basics of gas absorption spectroscopy	27
2.1 Introduction.....	27
2.2 Principle of direct absorption spectroscopy	27
2.2.1 Beer-Lambert law	27
2.2.2 Absorption lineshape.....	29
2.2.3 The detector signal	31
2.2.4 Noise and detection limit	32
2.3 Wavelength modulation spectroscopy (WMS)	33
2.4 Summary	38
References of Chapter 2	38
Chapter 3 Acoustic detector based on optical fiber Fabry-Perot interferometer	40
3.1 Introduction.....	40
3.2 The construction of a low finesse Fabry-Perot cavity.....	40
3.3 Mechanical properties of graphene diaphragm	42
3.3.1. Deflections under static pressure	43
3.3.2. Deflections under dynamic pressure	44

3.4 Signal demodulation	46
3.5 Acoustic detector with multilayer graphene diaphragm.....	50
3.5.1 Fabrication of the acoustic detector	52
3.5.2 Sensitivity and frequency response to acoustic pressure	58
3.5.3 Mechanical thermal noise limited equivalent pressure level	65
3.5.4 Long term stability and design of feedback control.....	67
3.6 Summary	74
References of Chapter 3	75
Chapter 4 Optical fiber photoacoustic gas sensor with graphene nano-mechanical resonator as the acoustic detector	77
4.1 Introduction.....	77
4.2 Basics of PAS gas detection.....	77
4.3 Gas detection experiments	80
4.3.1 Resonant and non-resonant detection.....	80
4.3.2 Operating at different acoustic resonances	85
4.4 Improvement of detection sensitivity.....	87
4.5 Summary	89
References of Chapter 4	89
Chapter 5 Resonating hollow-core fiber photonic microcell	91
5.1 Introduction.....	91
5.2 Resonating hollow-core fiber photonic microcell.....	91
5.2.1 Construction of a resonating HC-PBF photonic microcell	91
5.2.2 Fabrication of a resonating HC-PBF photonic microcell.....	93
5.2.3 Characterization of a resonating HC-PBF photonic microcell	103
5.3 Summary	108
References of Chapter 5	108
Chapter 6 Resonating HC-PBF microcell DAS gas sensor	110
6.1 Introduction.....	110
6.2 Cavity enhancement of a resonating HC-PBF microcell for gas absorption	110
6.3 Gas detection experiments based on direct absorption	112
6.3.1 Experimental setup.....	112
6.3.2 Gas detection results	115
6.3.3 Comparison with a single-path non-resonating HC-PBF gas cell	118

6.4 Summary	120
References of Chapter 6.....	120
Chapter 7 Resonating HC-PBF photonic microcell PT gas sensor	122
7.1 Introduction.....	122
7.2 Basics of cavity-enhanced PT spectroscopy with a resonating HC-PBF microcell	122
7.3 Cavity-enhanced PT gas experiments with a resonating HC-PBF photonic microcell	124
7.3.1 Experimental setup.....	124
7.3.2 Experimental results for gas detection.....	127
7.3.3 Comparison with a resonating HC-PBF photonic microcell based on DAS.....	136
7.4 Summary.....	137
References of Chapter 7.....	137
Chapter 8 Conclusion and future work	139
8.1 Conclusion	139
8.2 Future work.....	140

List of Figures

- Fig. 1.1 (a) A 2.5 cm long open path fiber pigtailed GRIN lenses absorption cell [23] and (b) a 6 m-long cell by connecting 60 pairs of fiber pigtailed GRIN lenses [25].
- Fig. 1.2 (a) Side-polished fiber, (b) Tapered fiber, and (c) D-fiber [10].
- Fig. 1.3 Scanning electronic microscope (SEM) images of HC-1550-02 fiber from NKT Photonics.
- Fig. 1.4 (a) Construction of a multi-segment HC-PBF gas sensor; (b) HC-PBGFs butt-coupling by mechanical splicing where standard zirconia ferrules are connected with a standard zirconia sleeve [11, 45, 46].
- Fig. 1.5 (a) Schematic of a HC-PBF with multiple micro-channels. (b) SEM image of a micro-channel drilled on a HC-1550-02 fiber [47].
- Fig. 1.6 Transmission spectrums of a 3.2-m-long HC-PBF with multiple drilled micro-channels [47].
- Fig. 1.7 Basic process in photothermal spectroscopy [22].
- Fig. 1.8 Schematic of PA wave generation by a tapered microfiber and PA detection with a quartz tuning fork [89].
- Fig. 1.9 (a) Schematic of acoustic detector formed between the fiber end of the diaphragm. (b) Experimental setup of the fiber-tip PAS gas detection system [93].
- Fig. 1.10 (a) PT phase modulation in a HC-PBF where pump and probe light beams propagate through the same gas-filled HC-PBF. (b) Experimental set-up for PT gas detection with 10-m-long HC-PBF [103].

- Fig. 2.1 Schematic of an optical absorption sensor.
- Fig. 2.2 Absorption spectrums of several gas in the near-infrared region [4].
- Fig. 2.3 Peak normalized Lorentzian and Gaussian lineshapes.
- Fig.2.4. (a) The basic process of WMS [3]. (b) Schematic of the general setup of WMS.
- Fig. 2.5 The first four harmonic coefficients for different modulation depth.
- Fig. 3.1 Schematic of the acoustic detector based on multilayer graphene diaphragm.
- Fig. 3.2 Schematic of a diaphragm based F-P cavity under an external pressure.
- Fig. 3.3 The calculated deformation of the diaphragm with different parameters of (a) thickness h , (b) radius r and (c) pre-stress σ_0 .
- Fig. 3.4 Resonant frequency as functions of the pressure for membranes with different radius r .
- Fig. 3.5 (a) Schematic of diaphragm based F-P cavity under acoustic wave. (b) Modulated reflected power spectrum.
- Fig. 3.6 Schematic of the demodulation system for diaphragm based F-P cavity.
- Fig. 3.7 Illustration of a linear operating range of the signal demodulation [9, 10].
- Fig. 3.8 (a) Interference fringes for different reflectance, and (b) corresponding sensitivity curves for each fringe.
- Fig. 3.9 Schematic diagram of the fiber FPI acoustic detector. (a) a graphene diaphragm with diameter of 2.5 mm covering the endface of a sleeve; (b) a graphene diaphragm with diameter of 125 μm covering the endface of a zirconia ferrule.

- Fig. 3.10 Fabrication process of the 100 nm-thick, 125- μ m-diameter MLG diaphragm-based FPI acoustic detector.
- Fig. 3.11 Fabrication process of the 100 nm-thick, 2.5-mm-diameter MLG diaphragm-based FPI acoustic detector.
- Fig. 3.12 Experimental setup for reflection spectrum measurement of the fabricated acoustic detector.
- Fig. 3.13 Measured reflection spectrum of the graphene diaphragm-based F-P cavity.
- Fig. 3.14 Schematic of a linear operating range of the sensor response curve. linear scale of the measured reflection spectrum of the FPI in Fig. 3.13.
- Fig. 3.15 Experimental setup for testing the performance of the optical fiber acoustic detector.
- Fig. 3.16 Frequency response of the fiber FPI with 125- μ m-diameter graphene diaphragm.
- Fig. 3.17 Power spectrum of the photo-detector output when an acoustic pressure level of (a) 35 mPa at 3.8 kHz and (b) 49.5 mPa at 7.4 kHz is applied.
- Fig. 3.18 Frequency response of the FPI with 2.5-mm-diameter graphene diaphragm.
- Fig. 3.19 Power spectrum of the photo-detector output when an acoustic pressure level of (a) 10.55 mPa at 10.1 kHz and (b) 12.05 mPa at 16.0 kHz is applied.
- Fig. 3.20 Calculated mechanical thermal noise P_N for different operation frequency of the diaphragm.
- Fig. 3.21 (a) Q -point drifts due to environmental perturbation. (b) The basic process of the Q -point tracking.

- Fig. 3.22 Experimental setup for testing the long term stability of the acoustic detector.
- Fig. 3.23 Without feedback control system: (a) DC output voltage of the F-P acoustic detector over 12 hours. (b) Power spectrum of the AC component for an applied acoustic pressure of 10 mPa at 10 kHz over 12 hours.
- Fig. 3.24 With feedback control system: (a) DC output voltage of the FP acoustic detector over 12 hours. (b) Power spectrum of the AC component for an applied acoustic pressure of 10 mPa at 10 kHz over 12 hours.
- Fig. 4.1 (a) The basic principle of PAS for gas detection. (b) Processes of PA wave generation. (c) a resonating PA cell for signal enhancement [4].
- Fig. 4.2 Experimental setup of the PAS system for acetylene detection.
- Fig. 4.3 Experimental results for the acetylene detection. (a) Second harmonic lock-in output (signal) when pump laser is tuned across the P(13) line of acetylene at 1,532.83 nm under different pump power levels. (b) Second harmonic lock-in output (noise) when the pump wavelength is tuned away from absorption and to 1,532.93nm. (c) Second harmonic signal and the s.d. of the noise as functions of pump power level.
- Fig. 4.4 Second harmonic lock-in output under different modulation frequencies when the pump laser is tuned to the P(13) absorption line and fixed to 1532.83 nm.
- Fig. 4.5 Experimental results for the acetylene detection at two specific resonances around (a, b) 5 kHz and (c, d) 22 kHz. (a) Second harmonic lock-in output (signal) at resonance of 5.545 kHz (black curve) and off resonance of 4.95 kHz (red curve). (b) Second harmonic lock-in output (noise) when the pump wavelength is tuned away from the absorption peak to 1,530.26 nm at

acoustic resonance of 5.545 kHz (black curve) and off acoustic resonance of 4.95 kHz (red curve). (c) Second harmonic lock-in output (signal) at resonance of 22.79 kHz (black curve) and off resonance of 21.05 kHz (blue curve). (d) Second harmonic lock-in output (noise) when the pump wavelength is tuned away from the absorption peak to 1,530.26 nm at resonance of 22.79 kHz (black curve) and off resonance of 21.05 kHz (blue curve).

Fig. 5.1 (a) Schematic of the proposed resonating HC-PBF photonic microcell. (b) Scanning electron microscopy (SEM) image of the HC-1550-06 fiber's cross-section.

Fig. 5.2 Schematic of the dielectric mirrors.

Fig. 5.3 Fabrication process of the dielectric mirror.

Fig. 5.4 The photos showing (a) the cross-section of the dielectric mirror and (b) a bundle of SMF pigtails coated with dielectric mirror.

Fig. 5.5 Experimental setup for mirror reflectivity measurement.

Fig. 5.6 The measured reflectivity of the dielectric mirrors.

Fig. 5.7 Extrinsic F-P cavity made by aligning two SMFs with mirrored ends.

Fig. 5.8 Fabrication procedures of an extrinsic F-P cavity.

Fig. 5.9 Experimental setup for F-P cavity transmission measurement.

Fig. 5.10 Different finesse values for different cavity lengths.

Fig. 5.11 Measured transmission spectrum of the FP cavity (a) wavelength from 1465 nm to 1570 nm, (b) wavelength from 1558 nm to 1562 nm.

- Fig. 5.12 Fabrication process of a resonating HC-PBF photonic microcell.
- Fig. 5.13 Schematics showing (a) the two cavity resonances sweeping across a fixed laser wavelength and (b) the transmission of the cavity when the cavity length is swept periodically with a triangular wave.
- Fig. 5.14 A photo of the HC-PBF microcell fixed on the PZT. (b) Experimental setup for transmission measurement of the microcell.
- Fig. 5.15 Measured transmission spectrums of HC-PBF microcells with cavity length of (a) 9.4 cm and (b) 6.75 cm.
- Fig. 5.16 Transmission spectrums of the proposed cavity when the PC is adjusted continuously. (b) Peak values for Peaks 1 and 2 in (a). (c) Transmission spectrums when the polarization is on one of the eigenstates.
- Fig. 6.1 Basics of cavity enhancement with a resonating HC-PBF photonic microcell for gas absorption. P_{in} , P_r and P_t denote respectively the cavity input, reflected and transmitted light powers.
- Fig. 6.2 Experimental setup for gas detection with the proposed resonating HC-PBF microcell.
- Fig. 6.3 Aligning process of a cavity resonance to the gas absorption line center. (a) Cavity resonances are not tuned to the absorption line center, (b) one of the resonances (Resonance A) is aligned to the center of an absorption line. Resonance B is away from the gas absorption line center. The wavelength of the DFB laser is tuned across to observe the resonances.
- Fig. 6.4 Experimental results. (a) Second harmonic lock-in output signals when laser is scanned across a resonance at the gas absorption line center at 1,532.83 nm indicated as Resonance A. (b) Second harmonic lock-in output signals when

laser is tuned across a F-P resonance away from gas absorption line center at 1,532.95 nm indicated as Resonance B. The black and red curves are respectively for the cavity filled with air and 550 p.p.m. acetylene balanced by nitrogen.

Fig. 6.5 Experimental results. (a) Second harmonic lock-in output signals when laser is tuned across a Fabry-Perot resonance at the gas absorption line center at 1,532.83 nm indicated as Resonance A. (b) Second harmonic lock-in output signals when laser is tuned across a Fabry-Perot resonance away from the gas absorption line center at 1532.89 nm indicated as Resonance B. The black and red curves are respectively for the cavity filled with air and 357 p.p.m. acetylene balanced by nitrogen.

Fig. 6.6 Experimental results. (a) Second harmonic lock-in output signals when laser is tuned across a F-P resonance at the gas absorption line center at 1,532.83 nm indicated as Resonance A. (b) Second harmonic lock-in output signals when laser is tuned across a Fabry-Perot resonance away from the gas absorption line center at 1532.88 nm indicated as Resonance B. The black and red curves are respectively for the cavity filled with air and 725 p.p.m. acetylene balanced by nitrogen.

Fig. 6.7 Absorption signal as function of gas concentration.

Fig. 6.8 Second harmonic lock-in output when the DFB laser wavelength is swept across the resonance at 1532.83 nm for ~500 s duration.

Fig. 6.9 (a) Experimental setup for measuring the transmission spectrum of a single-path cell. (b) Measured transmission spectrum of the HC-PBF cell. (c) Fourier transform of the spectrum in (b).

- Fig. 7.1 Basics of cavity-enhanced PT spectroscopy. (a) Sketch of the resonating HC-PBF photonic microcell. (b) Basic processes involved in producing phase modulation in a resonating HC-PBF photonic microcell.
- Fig. 7.2 Measured transmission spectrums of resonating HC-PBF photonic microcell at wavelength of (a) 1532.83 nm and (b) 1550.02 nm.
- Fig. 7.3 Basic process for cavity-enhanced photothermal gas experiments. The pump laser is tuned to a cavity resonance (Resonance A) which is aligned to the center of the gas absorption line, while the probe laser is tuned to the highest slope point of another cavity resonance (Resonance B) which is away from the center of the gas absorption line.
- Fig. 7.4 Experimental setup of the PT gas detection with a HCF Fabry-Perot resonating waveguide. Blue line, optical fiber; greenline, electrical cable; ECDL, external cavity diode laser; DFB, distributed feedback laser; PC, polarization controller; PZT, piezoelectric stack; WDM, wavelength division multiplexer; PD, photo-detector; DAQ, data acquisition
- Fig. 7.5 Second harmonic lock-in output when pump laser is tuned across the P(13) line of acetylene and the corresponding cavity resonances. The gas cell is filled with (a) 100 ppm acetylene balanced by nitrogen and (b) nitrogen, respectively.
- Fig. 7.6 (a) Second harmonic output when pump laser is tuned across the cavity resonance at the center of the absorption line when the gas cell is filled with 100 ppm acetylene. (b) Second harmonic output when pump laser is tuned across the one of the cavity resonances near the absorption line when the gas cell is filled with nitrogen. (c) Second harmonic output when the pump is tuned to the off cavity resonance.

- Fig. 7.7 (a) The peak values of the second harmonic signal in Fig. 7.5 (a). (b) The normalized peak values in Fig. 7.5 (a) and Fig. 7.6 (a). Blue squares: the normalized peak values; red dashed line: Lorentz fitting of the normalized peak values; Black solid line: normalized P(13) absorption line of acetylene.
- Fig. 7.8 (a) The second harmonic outputs (signal) for different pump power levels delivered to the HC-PBF cavity when the pump wavelength was tuned across the cavity resonance at the center of P(13) absorption line. (b) The peak values of second harmonic signal (red squares) and the s.d. of the noise (blue circles) as functions of pump power level.
- Fig. 7.9 Schematic showing the wavelength of the probe beam operating at five different points (Point 1-5). Blue line: cavity resonance at 1550 nm (Resonance B); Brown line: 1st order derivative of Resonance B.
- Fig. 7.10 (a) The second outputs (signal) for the wavelength of the probe beam operating at five different points (1-5) when the pump wavelength was tuned across Resonance A at the center of P(13) absorption line. (b) The peak values of second harmonic signal (green squares) and the s.d. of the noise (blue circles) when the probe wavelength operating at different points.
- Fig. 7.11 (a) Theoretical calculation of the 1st order derivative of a HC-PBF resonating waveguide with different finesse. (b) Peak values of 1st order derivative as functions of cavity finesse.
- Fig. 7.12 Schematic of an extrinsic fiber Fabry Perot cavity.
- Fig. 7.13 The measured transmission of an extrinsic F-P cavity at (a) wavelength of 1465~1560 nm and (b) wavelength of 1552~1560 nm.
- Fig. 7.14 (a) The calculated enhancement factor E as a function of on-resonance

cavity transmission T_{res} for a given finesse of 307. (b) The calculated relationship between the enhancement factor E and the cavity finesse for a given T_{res} of 0.9.

List of Tables

- Table 1.1 Detection limit of DAS HC-PBF gas sensors
- Table 1.2 Detection technique in photothermal spectroscopy [22].
- Table 1.3 Detection limit of PAS gas sensors [88].
- Table 1.4 Detection limit of PTI HC-PBF gas sensors
- Table 2.1 Noise that may affect the gas detected signal
- Table 3.1 Values of a_{mn}
- Table 3.2 Resonant frequency (kHz) for different vibration modes
- Table 3.3 Characteristic parameters of the graphene diaphragms
- Table 3.4 MDP value of the 125 μm -diameter optical fiber acoustic detector operating at Q -point
- Table 3.5 MDP value of the 2.5 mm-diameter optical fiber acoustic detector operating at Q -point
- Table 3.6 Measured MDP and calculated mechanical thermal noise of graphene diaphragm based acoustic detector
- Table 4.1 Performance of gas sensor for two different modulation frequencies
- Table 4.2 Detection limits of graphene diaphragm based PAS gas sensors
- Table 4.3 Physical parameters of graphene diaphragm and air
- Table 5.1 Losses of different methods for alignment.
- Table 7.1 Parameters of the current HC-PBF resonating waveguide

List of Acronyms

LAS laser absorption spectroscopy

ppm parts-per-million

ppb parts-per-billion.

HC-PBF hollow-core photonic bandgap fiber

PT photothermal

PAS photoacoustic spectroscopy

PTI photothermal interferometry

F-P Fabry-Perot

SMF single mode fiber

DAS Direct absorption spectroscopy

sub-ppb sub parts-per-billion

D-fibers D-shaped optical fibers

IG-PCF Index-guiding photonic crystal fiber

SCF suspended-core fiber

NEC noise equivalent concentration

NEA noise equivalent absorption coefficient

SEM Scanning electronic microscope

PA photoacoustic

sub-ppm sub-parts-per-million

NNEA normalized noise equivalent absorption coefficient

QTF quartz tuning fork

FPI Fabry-Perot interferometer

MZI Mach-Zehnder interferometer

WMS wavelength modulation spectroscopy

RAM residual amplitude modulation

IM intensity modulation

RIM residual intensity modulation

SNR signal-to-noise ratio

RMS root-mean-square

DFB distributed feedback semiconductor

ECDL external cavity diode laser

OC optical circulator

PD photo-detector

ESA electrical spectrum analyzer

Q point quadrature point

MLG/Ni/MLG film multilayer graphene/Nickel(Ni)/ multilayer graphene film

CVD chemical vapor deposition

DI de-ionized

UV ultraviolet

BBS broadband light source

OSA optical spectrum analyzer

MDP minimum detectable pressure

DAQ data acquisition card

FWHM full width at half maximum

HWHM half width at half maximum

FSR free spectral range

PC polarization controller

PZT piezoelectric stack

MI modal interference

Chapter 1

Introduction

1.1 Background

Trace gas detection plays an important role in many fields such as environmental monitoring, safety and industrial process control as well as national security applications [1]. Traditional gas sensors based on different mechanisms have been demonstrated and developed widely for many years, such as gas chromatographs [2], catalytic combustion gas sensors [3], semiconductor gas sensors [4, 5], and electrochemical gas sensors [6]. Catalytic combustion gas sensors perform well in detecting flammable gases but have low response with unflammable gases, limiting its applications and having potential hazardous in explosive circumstances. Semiconductor gas sensors can achieve high sensitivity but with low selectivity, moreover, their instability makes them susceptible to the external environments. Electrochemical gas sensors can achieve high sensitivity and selectivity but with short lifetime of one or two years. Apart from the conventional sensors, optical fiber gas sensors based on laser absorption spectroscopy (LAS) can offer an effective method to identify and detect the trace gas, showing outstanding characteristics including compact size, remote interrogation, immunity to electromagnetic interference and safety in hazardous environments [7-11].

Conventional optical fiber gas sensors based on Beer-Lambert Law of the direct absorption spectroscopy (DAS) use an open-path absorption cell with fiber pigtails to measure the transmitted light intensity for gas absorption, which provides a simple method in the harsh environment [7, 12, 13]. Increasing absorption path length can improve the detection sensitivity of the absorption based gas sensor intuitively. However, the absorption path length in free space or open-path optics is intrinsically restricted

since the inevitable light diffraction between these optics may decrease the light intensity as it propagates. Longer absorption path length may be achieved by using multi-pass absorption cells such as the White cells [14], Herriott cells [15] and cavity enhanced optical cells [16, 17]. However, these gas cells are somehow bulky in free space and need complex alignment.

In order to develop optical fiber gas sensors with high sensitivity and better responsivity, many indirect instrumental methods were investigated, such as wavelength modulation spectroscopy (WMS) [18-20], photoacoustic spectroscopy (PAS) [21] and photothermal interferometry (PTI) [22]. These methods have demonstrated sub-parts-per-billion (sub-ppb) level detection sensitivity.

1.1.1 Direct absorption optical fiber gas sensors

Figure 1.1(a) shows a typical open path gas cell made by a pair of pigtailed collimated lenses (GRIN lenses) with a optical distance of 2.5 cm where the fiber is only used for light transmission [23]. Gas absorption takes place between two lenses, achieving a detection sensitivity of 75 ppm acetylene with this absorption cell. Since the transparent window of the standard silica fibers is from ~ 0.5 to ~ 2 μm , covering the relatively weak absorption lines of gas molecules, long absorption path length is required for better detection sensitivity. To implement longer absorption path length, 60 pairs of fiber pigtailed GRIN lenses were cascaded to achieve an absorption path length of 6 m as shown in Figure 1.1(b) [24, 25]. However, these cells are bulky and the length is limited by the increase of the insertion loss of the cascaded GRIN lenses.

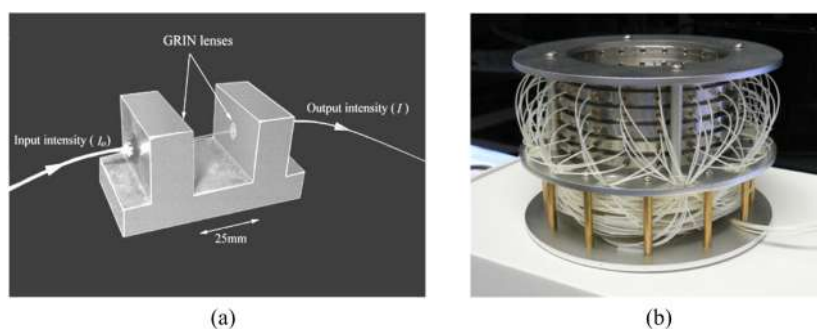


Fig. 1.1 (a) A 2.5 cm long open path fiber pigtailed GRIN lenses absorption cell [23] and (b) a 6 m-long cell by connecting 60 pairs of fiber pigtailed GRIN lenses [25].

All fiber evanescent-wave absorption based gas sensors were proposed to enhance the light-gas interaction with optical fibers, including side-polished fibers [26], tapered micro/nano fibers [27, 28] and D-shaped optical fibers (D-fibers) [29], as shown in Figure 1.2. In this situation, optical fibers are not only used for light transmission but also as the critical sensing elements for gas detection. For the side-polished fibers, tapered micro/nano fibers and D-fibers, the gas absorption is measured by exposing propagating mode to the surrounding gas outside the fiber, and the portion of evanescent-wave power exposed to the environment is small. So it is impractical to build up high detection sensitivity sensors with these three types of fibers.

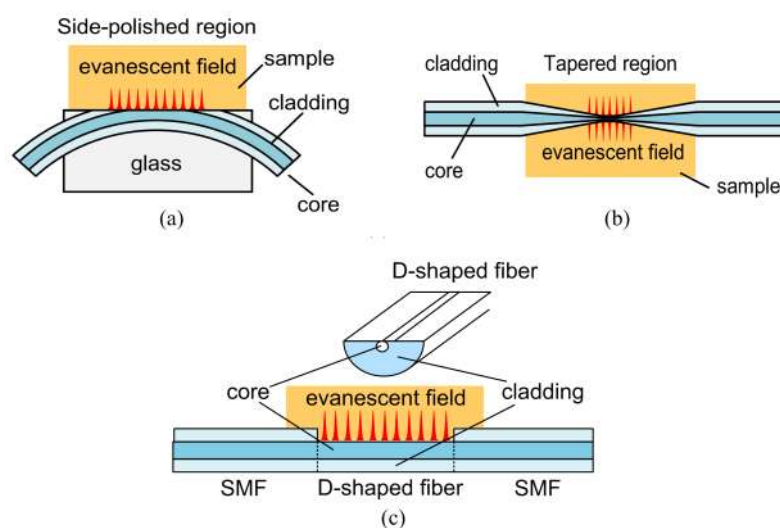


Fig. 1.2 (a) Side-polished fiber, (b) Tapered fiber, and (c) D-fiber [10].

Compared to the D-fibers, small-core index-guiding (IG) photonic crystal fibres (PCFs) and suspended-core fibres (SCFs) have a larger percentage of optical power (e.g., 1 to 30% at 1.5 μm) located in the air-holes in the cladding region, so they offer a good platform for gas detection via evanescent field absorption [30, 31]. 10 cm-long IG-PCF gas cell was firstly used for gas detection experiments by Hoo et al. [30, 32], and the detection limit of 5.6 ppm with 4.87-m-long PCF was predicted. In order to have faster gas filling to the evanescent field, introduction of multiple side-openings along the fiber was also proposed [33, 34].

Having most of the optical power (e.g., 95%) inside the central hollow-cores, HC-PBFs offer excellent platform for strong light-gas interaction inside the fiber cores [35, 36], which is much higher than the IG-PCF and SCF. HC-PBF has a hollow-core diameter of $\sim 11 \mu\text{m}$ as shown in Figure 1.3 and its transmission window is from 1500 nm to 1700 nm with transmission loss of $< 24 \text{ dB/km}$, covering different gas absorption lines such as CO, CO₂, NH₃, H₂S, C₂H₂ and CH₄. Cregan et al. firstly proposed that HC-PBFs can be used for gas detection in 1999 [37]. Then Hoo et al. investigated the gas diffusion measurement in a HC-PBF in 2005 [38], which was followed by Ritari et al. who demonstrated gas absorption experiments using HC-PBFs in the transmission windows of 1300 and 1500 nm, covering the absorption line of acetylene, hydrogen cyanide, methane and ammonia [39]. Table 1.1 summarizes the lower detection limits of some of the reported HC-PBF gas sensing systems based on DAS. It lists the system performance in terms of noise equivalent concentration (NEC) and noise equivalent absorption coefficient (NEA).

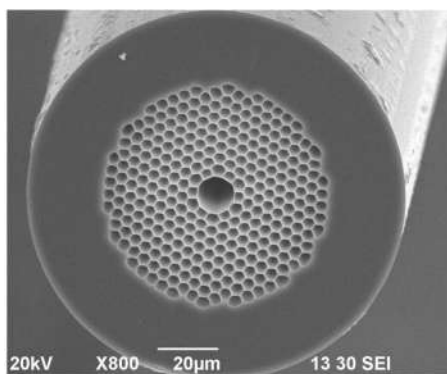


Fig. 1.3 Scanning electronic microscope (SEM) images of HC-1550-02 fiber from NKT Photonics

Table 1.1 Detection limit of DAS HC-PBF gas sensors

Gas type	Wavelength(μ m)	Length of HC-PBF	Integration time(s)	NEC(ppm)	NEA(cm^{-1})
CH ₄ [40]	1.645	5.1 m	Not stated	10	1.6×10^{-9}
CH ₄ [41]	1.665	7 cm	Not stated	647	7.4×10^{-5}
C ₂ H ₆ [42]	3.35	5.69 m	Not stated	0.9	4.6×10^{-5}
CO ₂ [43]	2.005	5.27 m	0.018	311	2.6×10^{-3}
C ₂ H ₂ [44]	1.53037	27 m	Not stated	50	5.8×10^{-5}

DAS, direct absorption spectroscopy.

Using long length of HC-PBF could improve the gas detection sensitivity, however, it is impractical to use very long length of HC-PBF (e.g., 100 metres to kilometres), since it will also make the sensor response extremely slow because of the very long time needed to load gas into the hollow-core [30]. Different approaches for improving the response time of the HC-PBF sensors have been reported. A pressure-driven gas-filling method was reported by Wynne [44], where a pressure differential was applied between two ends of the sensing fiber. Parry et al. [45] and Carvalho et al. [46] reported that multiple segments of HC-PBF could be combined and connected by butt-couplings shown in Figure 1.4, where gas sample can diffuse into the hollow core inside the fiber via the small slit of the sleeve. However, the coupling loss between the HC-PBF may

limit the number of segments.

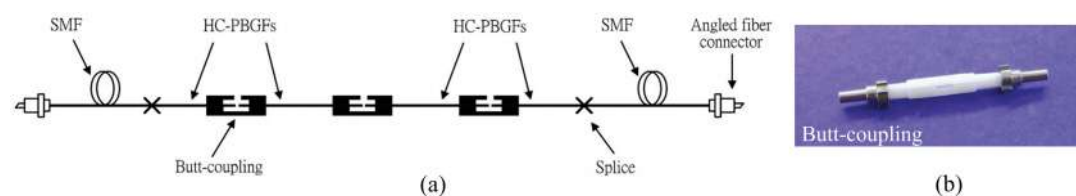


Fig. 1.4 (a) Construction of a multi-segment HC-PBF gas sensor; (b) HC-PBGFs butt-coupling by mechanical splicing where standard zirconia ferrules are connected with a standard zirconia sleeve [11, 45, 46].

Drilling of micro-channels along the HC-PBF by a femtosecond laser is an alternative technique to improve the response time [33, 34, 41], as shown in Figure 1.5. Six micro-channels in a 33-cm-long HC-PBF by a femtosecond laser was demonstrated by Hensley, and the loss caused by each channel was as low as 0.35 dB [33]. Yang et al. fabricated 144 micro-channels along 3.2-m-long HC-PBF sample by a femtosecond laser, and the mean loss of the micro-channels is less than 0.027 dB per channel shown in Figure 1.6 [47].

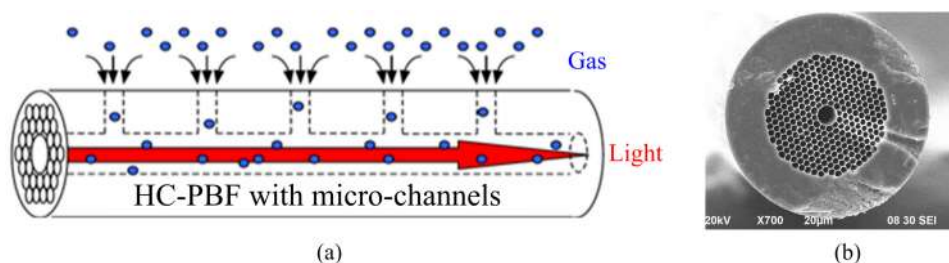


Fig. 1.5 (a) Schematic of a HC-PBF with multiple micro-channels. (b) SEM image of a micro-channel drilled on a HC-1550-02 fiber [47].

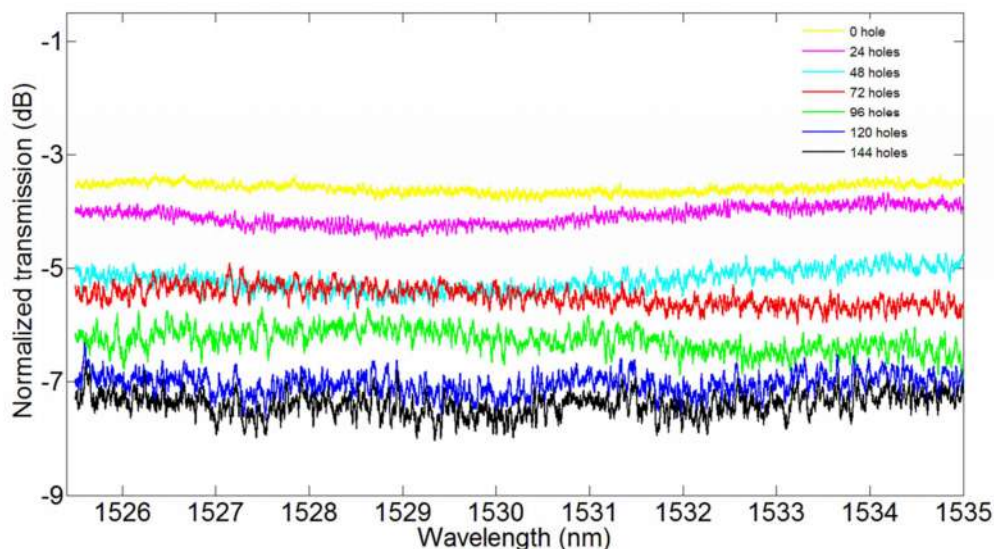


Fig. 1.6 Transmission spectrums of a 3.2-m-long HC-PBF with multiple drilled micro-channels. [47].

1.1.2 Photothermal spectroscopic optical fiber gas sensors

Compared with the conventional direct absorption fiber optic gas sensors, photothermal (PT) spectroscopy is an indirect method for high sensitivity gas detection. Figure 1.7 shows the basic process of the photothermal spectroscopy [22]. The basis of photothermal spectroscopy is a photo-induced change in the thermal state of the target sample. When a modulated optical laser source is used to excite the absorbing gas sample, the gas sample will absorb the optical energy and its internal energy will increase, inducing a temperature change of the gas or the surrounding fluid. The rapid temperature change will result in a density change and pressure change, and hence the refractive index change of the gas. Measurements of the temperature, pressure, or refractive index changes that occur due to optical absorption are the basis for different photothermal detection methods. Table 1.2 summarizes different detection techniques used in photothermal spectroscopy [22]. Here we mainly introduced the photoacoustic spectroscopy (PAS) and photothermal interferometry (PTI). Detection sensitivity down to ppb concentration level has been demonstrated.

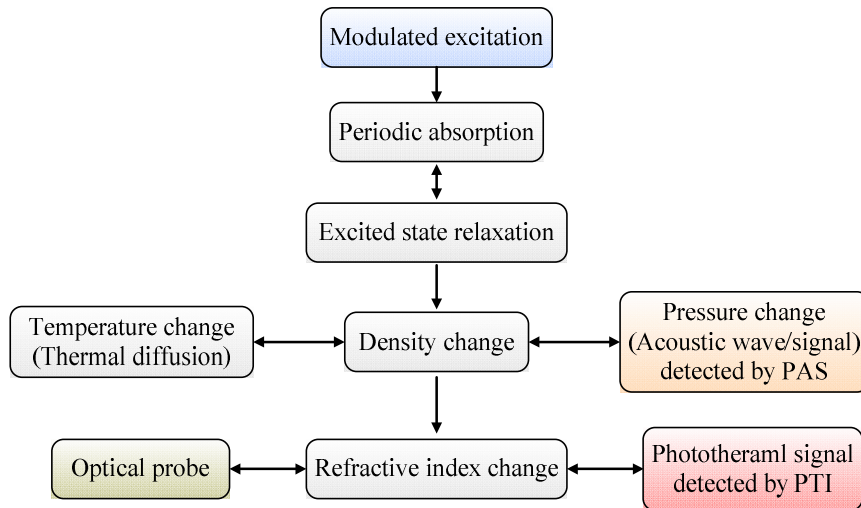


Fig. 1.7 Basic process in photothermal spectroscopy [22].

Table 1.2 Detection technique in photothermal spectroscopy [22].

Thermodynamic parameter	Measured Property	Detection technique
Temperature	Temperature	Calorimetry
	Infrared emission	Photothermal radiometry
Pressure	Acoustic wave	Photoacoustic spectroscopy
Density	Refractive index	Photothermal lens
		Photothermal interferometry
		Photothermal deflection
		Photothermal refraction
	Photothermal diffraction	
Surface deformation	Surface deflection	

1.1.2.1 Fiber based photoacoustic spectroscopy

Photoacoustic spectroscopy (PAS), in which periodic light absorption of gas molecules is converted into acoustic pressure wave via the photoacoustic (PA) effect, is a powerful

spectroscopic technique for trace gas analysis [48-50]. Gas detection based on PAS may be dated back to 1938 where a blackbody emitter was used as the light source to excite the generation of acoustic wave [51]. In 1968, a CO₂ laser was used as the light source for PA detection of carbon dioxide [52]. Since then, various laser-based systems with wavelength ranging from mid- to near-infrared have been reported for the detection of different gases [53-56]. These systems use a PA cell in which light absorption of gas takes place, and the acoustic signal is generated and detected. The PA signal can be further enhanced by using an acoustic resonator to form a resonant PA cell [57, 58]. By modulating the intensity/wavelength of the laser at a frequency matched to the resonant frequency of the acoustic resonator, an amplified PA signal is generated due to resonant buildup and acoustic energy accumulation within the gas cell. A variety of PA resonators operating on longitudinal, azimuthal and radial resonances have been developed for trace gas detection [48, 59-70].

The generation of acoustic wave can also be enhanced by using optical multi-pass [71-74] and cavity enhanced PA cells [75, 76]. In a multi-pass system, light beam is reflected multiple times over a certain detection area, resulting in increased light absorption and hence the larger acoustic energy over the area. By tuning the laser wavelength to a cavity mode of a high-finesse optical cavity, optical power could be coupled into the cavity efficiently, leading to high optical power buildup and yielding a stronger PA signal within the cavity.

For acoustic detection, various techniques have been used, including capacitive microphones [68-70], resonant quartz tuning forks [50, 77-82], and micro-cantilever beams in combination with optical interferometry [83-87]. With these acoustic detectors, gas detection down to sub-parts-per-million (sub-ppm) or ppb level has been achieved. Table 1.3 summarizes the lower detection limits of some of the reported PAS systems operating at the near infrared wavelength region. It lists the system performance in terms

of NEC and normalized NEA (NNEA). The NNEA is independent of the gas species and provides a common basis for comparison of the various PAS systems.

Table 1.3 Detection limit of PAS gas sensors [88]

Gas type	Wavelength (μm)	Detection technique	Pressure (Torr)	Power (mW)	NNEA ($\text{cm}^{-1}\text{WHz}^{-1/2}$)	NEC (ppm)	Integration time(s)	Resonant tube
NH_3 [68]	1.532	Microphone	100	500	1.5×10^{-9}	0.006	10	Yes
C_2H_2 [69]	1.511	Microphone	760	3.5	4×10^{-8}	10	0.003	Yes
NH_3 [70]	1.532	Microphone	760	500	Not stated	0.003	0.1	Yes
CH_4 [77]	1.667	QEPAS	375	2	1.2×10^{-7}	Not stated	1	Yes
NH_3 [78]	1.532	QEPAS	60	38	7.2×10^{-9}	0.65	1	Yes
H_2O [80]	1.396	QEPAS	760	8	5.9×10^{-9}	Not stated	1	Yes
C_2H_2 [82]	1.532	QEPAS	770	37	3.3×10^{-9}	0.085	1	Yes
CO_2 [84, 86]	1.572	Cantilever-based	190	50	4.9×10^{-9}	7.2	Not stated	No
CO_2 [85]	1.572	Cantilever-based	760	30	1.7×10^{-10}	1.9	2.6	No

QEPAS, Quartz-enhanced photoacoustic spectroscopy; NNEA, Normalized noise equivalent absorption coefficient; NEC, noise equivalent concentration.

However, most of the acoustic detectors used electrical cables for signal transmission which limits their applications in remote detection and in environments with high electromagnetic interference. These limitations may be overcome by the employment of optical fibers and fiber-based technologies.

For PA signal excitation with optical fibers, fiber pigtailed graded index collimator was applicable since the laser beam can be transmitted through optical fiber for PA signal excitation and complex alignment of bulky lenses is no longer essential in the system. Moreover, in order to avoid using complex collimating lenses, Cao et al. demonstrated that the PA wave can be generated by the evanescent field of a tapered optical microfiber as shown in Figure 1.8 [89], where a microfiber is placed in between

two prongs of a resonant quartz tuning fork (QTF). With diameter of $1.1\ \mu\text{m}$, normalized NEA of $1.96 \times 10^{-6}\ \text{cm}^{-1}\text{W}/\sqrt{\text{Hz}}$ was achieved. The excited PA signal can be further enhanced by using microfibers with smaller diameters.

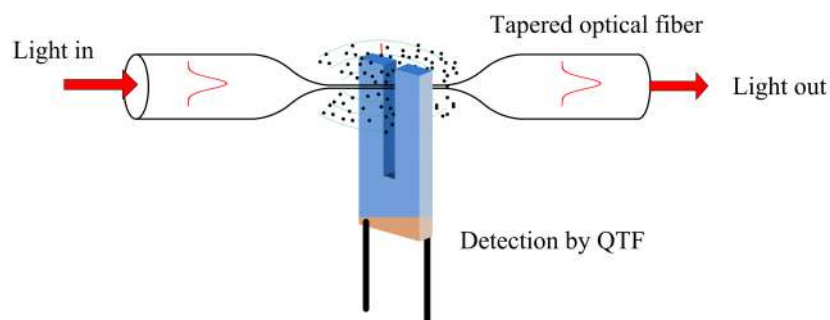


Fig. 1.8 Schematic of PA wave generation by a tapered microfiber and PA detection with a quartz tuning fork [89].

For PA signal detection with optical fibers, Leslie et al. reported the first optical fiber spectrophone for the detection of PA wave in 1981 [90]. Later, Breguet et al. demonstrated an optical-fiber microphone formed by winding a fiber coil on a thin plate as one arm of a Michelson interferometer to detect the acoustic signal and achieved a lower detection limit of 14 ppb of ethanol and ozone vapor [91]. Over the past decade, significant work has been done in developing miniature fiber-tip Fabry-Perot interferometer (FPI) type microphones [92-98]. Fiber-tip FPI pressure/acoustic sensors with thin photonic crystal [95], metal [96, 97], polymer [92, 93] and graphene diaphragms [98] were reported. These optical fiber probes would be ideally suited for space-limited applications such as acoustic detection within a PA cell. Wang et al. reported the use of a diaphragm-based fiber FPI acoustic sensor in combination with an acoustic resonator for acetylene detection [92]. They used a polymer diaphragm with diameter of 4 mm and thickness of $6\ \mu\text{m}$ and achieved a minimum detectable gas concentration of 1.56 ppb with 500 mW of pump laser power. Without using an acoustic resonator, Cao et al. demonstrated a simple miniature all-fiber PAS gas sensor with a

fiber-tip FPI with a 2- μm -thick, 2.75-mm-diameter polymer diaphragm as the acoustic detector as shown in Figure 1.9 [93]. A lower detection limit of 4.3 parts-per-million (ppm) was achieved with an optical power level of only ~ 8 mW. The acoustic sensitivity of the fiber FPI acoustic detector is largely determined by the dimensions and the mechanical properties of the diaphragm and would be enhanced by using a thinner and larger diaphragm.

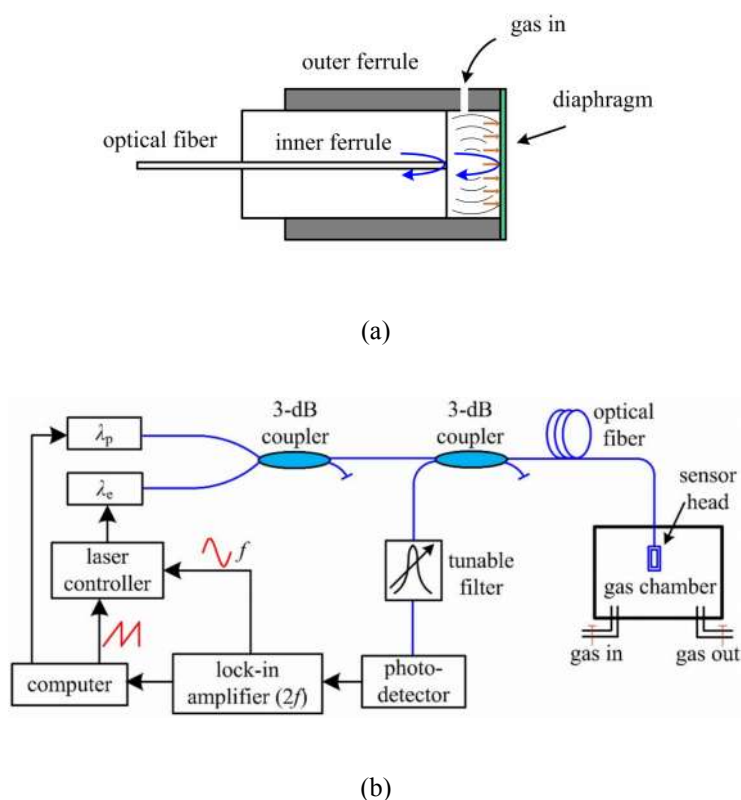


Fig. 1.9 (a) Schematic of acoustic detector formed between the fiber end of the diaphragm. (b) Experimental setup of the fiber-tip PAS gas detection system. [93]

1.1.2.2 Fiber based photothermal interferometry

Photothermal interferometry (PTI) detects the phase modulation induced by gas absorption, leading to refractive index change of the gas sample by via photothermal (PT) effect. Different types of gas have been reported, such as methanol [99], ammonia [100], sulfur hexafluoride [101], and nitrogen dioxide [102] with very high sensitivity.

However, previously reported PTI gas detection systems used free-space optics and mid-infrared pump laser sources, making the system clumsy and bulky. Wei Jin et al. firstly studied PT effect in gas-filled hollow-core photonic bandgap fibres (HC-PBFs) and demonstrated a detection limit of ~ 2 ppb for acetylene with a 10-meter-long HC-PBF [103]. As shown in Figure 1.10, when a wavelength modulated pump beam is propagating with a probe beam in a gas-filled HC-PBF, the phase of the probe is modulated due to periodic pump gas absorption. Using HC-PBF would enable large phase modulation at the wavelength of 1530 to 1535 nm covering weak absorption of the target gas by using a low pump power level. Therefore, near-infrared laser sources and optical fiber components can be applied in these fiber optic systems, enabling good compatibility with the standard telecommunication fiber optic systems.

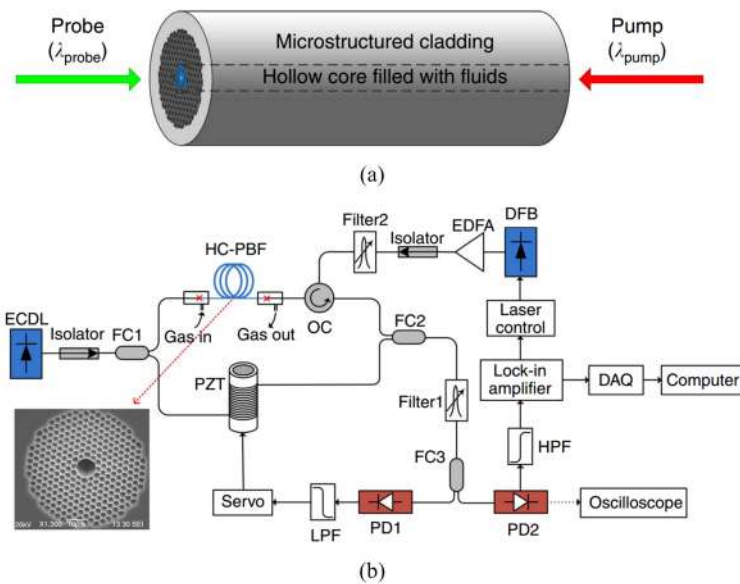


Fig. 1.10 (a) PT phase modulation in a HC-PBF where pump and probe light beams propagate through the same gas-filled HC-PBF. (b) Experimental set-up for PT gas detection with 10-m-long HC-PBF [103].

HC-PBF gas sensor based on different optical interferometer configurations have been proposed and studied in our research group, such as Mach-Zehnder interferometer (MZI) [103], in-fiber MZI [47], Sagnac interferometer [47], Fabry-Perot interferometer

(FPI) [104]. Table 1.4 summarizes the lower detection limits of some of the reported PTI HC-PBF gas sensing systems. It lists the system performance in terms of NEC and NEA.

Table 1.4 Detection limit of PTI HC-PBF gas sensors

Gas type	Wavelength(μm)	Length of HC-PBF	Interferometer configuration	Integration time(s)	NEC(ppm)	NEA(cm^{-1})
C_2H_2 [103]	1.53037	10 m	MZI	1	0.002	2.3×10^{-9}
C_2H_2 [47]	1.53037	0.3 m	In-fiber MZI	1	1	1.2×10^{-6}
C_2H_2 [47]	1.53037	0.62 m	Sagnac	1	0.775	9.3×10^{-7}
C_2H_2 [104]	1.53037	0.02 m	FPI	77	0.117	1.4×10^{-7}

1.2 Motivation and significance of this work

The detection sensitivity of LAS sensors can be improved by using longer absorption cell. Using of a longer length of HC-PBF as absorption cell could improve the detection sensitivity. However, it is very difficult to achieve ppb level detection because it would require a very long length of HC-PBF (e.g., 100 meters). This will also make the sensor response extremely slow because of the very long time needed to fill gas sample into the hollow-core. So the current direct absorption gas sensors are difficult to achieve high sensitivity and fast response simultaneously.

In this thesis, we aim to investigate the all optical fiber gas sensors based on photothermal spectroscopy which can achieve high sensitivity and fast response simultaneously. Photothermal spectroscopy is an alternative indirect method which can provide high sensitivity for gas detection. Trace gas detection based on photothermal effect has been investigated by many instrumental methods such as PAS and PTI. These methods have demonstrated sub-ppb level detection sensitivity.

The first motivation of this thesis is to propose an all-optical fiber photoacoustic gas sensor with a graphene nano-mechanical resonator as the acoustic detector. The acoustic detector is a low finesse Fabry-Perot interferometer formed by attaching multilayer graphene diaphragm to a hollow cavity at the end of a single mode optical fiber. By operating at one of the mechanical resonances of the diaphragm, the sensitivity for acoustic detection is enhanced. Detection of acetylene gas is demonstrated with a distributed feedback semiconductor laser tuned to the P(9) absorption line of acetylene and a lower detection limit of 119.8 ppb is achieved. Theoretical analysis shows that by increasing the Q -factor of the resonator, which may be achieved by operating at low gas pressures, ppb level gas detection is possible.

In the second parts, we also propose and fabricate a high finesse resonating HC-PBF photonic microcell. This cell is formed by aligning two single mode fibers with coated high reflectivity mirrors to both sides of one piece of HC-PBF. A resonating HC-PBF photonic microcell with length of 6.75 cm can be made to achieve a cavity finesse of 128, corresponding to an effective optical path length of ~ 5.5 m. By using a resonating HC-PBF photonic microcell with length of 9.4 cm and cavity finesse of 68, a lower detection limit of 7 ppm acetylene is demonstrated based on direct absorption.

The sensitivity of resonating HC-PBF photonic microcell based on direct absorption spectroscopy is found limited. In order to further improve the detection sensitivity, we also investigate a cavity-enhanced PT spectroscopic gas sensor with a resonating HC-PBF microcell. Experiments with a 6.2-cm-long resonating microcell with a finesse of 45 for pump beam and 41 for probe beam demonstrated a detection limit of 126 ppb acetylene. The cavity enhancement of such a resonating HC-PBF microcell can simultaneously amplify the intracavity build-up intensity for the pump beam inside the HC-PBF and improve the slope of the operating point for the probe beam by a factor proportional to the cavity finesse. The double-cavity-enhanced PT

spectroscopic gas sensor enables higher intracavity build-up intensity and allows us to use shorter length of HC-PBF, which can be used to develop all-fiber gas sensors with high sensitivity and fast response.

1.3 Thesis outline

The thesis structure is arranged as follows:

Chapter 1 reviews the development and background of optical fiber gas sensors. Optical fiber gas sensors combined with different detection methods such as direct absorption spectroscopy, photothermal spectroscopy (including PAS and PTI) are introduced, and their performances have been compared. Then the motivation of this work is proposed, followed by the thesis outline.

Chapter 2 introduces the principle of DAS and WMS. The absorption lineshapes, detected signal, and the detection limit are also introduced.

Chapter 3 and **Chapter 4** demonstrate an all optical fiber photoacoustic gas sensor with a graphene nano-mechanical resonator as the acoustic detector.

Chapter 3 presents the acoustic sensor based on an optical fiber Fabry-Perot interferometer with graphene diaphragm. For this acoustic detector, the basics, construction, its response to acoustic pressure wave, and signal demodulation are introduced and analyzed first. Then the fabrication of the acoustic detector is illustrated and its frequency response to acoustic pressure is presented. Finally, a feedback control system for operating point stabilization is designed and applied to the acoustic experiments.

Chapter 4 demonstrates an all optical fiber photoacoustic gas sensor. The acoustic detector introduced in Chapter 3 will be used for gas detection via the photoacoustic effect. The basics of photoacoustic spectroscopy for gas detection and interference signal

demodulation are introduced. The limit of gas detection under different modulation frequency are tested experimentally. A lower detection limit of ~ 120 ppb is achieved by operating at one of the mechanical resonances of the diaphragm. The improvement of the detection sensitivity are also discussed.

Chapter 5 introduces a novel resonating HC-PBF photonic microcell which can be used to enhance the performance of DAS and PT gas sensor in Chapter 6 and Chapter 7. Firstly the construction and fabrication of the resonating microcell is introduced, then the characterization of the microcell is presented. The cavity transmission and finesse are measured and calculated experimentally.

Chapter 6 and **Chapter 7** demonstrate a resonating HC-PBF photonic microcell for high performance gas detection based on DAS and PT effect.

Chapter 6 demonstrates a resonating HC-PBF photonic microcell for high performance gas detection based on DAS. By using this resonating HC-PBF photonic microcell, the effective absorption path length can be enhanced by a factor proportional to the cavity finesse. With a cavity length of 9.4 cm and finesse of 68, we demonstrated acetylene detection with a detection limit of ~ 7 p.p.m, 1-2 orders of magnitude better than a single-path HC-PBF sensor with a similar length.

Chapter 7 demonstrates the cavity-enhanced PT gas experiments with a resonating HC-PBF photonic microcell. The basic of cavity enhancement for photothermal spectroscopy is firstly introduced, then the cavity-enhanced PT gas experiments are demonstrated. With a cavity length of 6.2 cm and finesse of 45 for pump beam and 41 for probe beam, we demonstrated acetylene detection with a detection limit of ~ 126 ppb, 1-2 orders of magnitude better than a high finesse HC-PBF sensor with a similar length of 9.4 cm based on direct absorption.

Chapter 8 summarizes the conclusions of the whole work and gives several suggestions

for future research.

References of Chapter 1

- [1] U. Willer, M. Saraji, A. Khorsandi, P. Geiser, and W. Schade, "Near-and mid-infrared laser monitoring of industrial processes, environment and security applications," *Optics and lasers in engineering* 44, 699-710 (2006).
- [2] D. Matthews and J. Hayes, "Isotope-ratio-monitoring gas chromatography-mass spectrometry," *Anal. Chem.* 50, 1465-1473 (1978).
- [3] V. Katti, A. Debnath, S. Gadkari, S. Gupta, and V. Sahni, "Passivated thick film catalytic type H₂ sensor operating at low temperature," *Sensor. Actuat. B-Chem* 84, 219-225 (2002).
- [4] D. Williams, *Conduction and gas response of semiconductor gas sensors*, ed P. T. Moseley and B. C. Tofield (Bristol: Adam Hilger) chapter 4 (1987).
- [5] P. Moseley, "Solid state gas sensors," *Meas. Sci. Technol.* 8, 223 (1997).
- [6] E. Bakker and M. Telting-Diaz, "Electrochemical sensors," *Anal. Chem.* 74, 2781-2800 (2002).
- [7] B. Culshaw, G. Stewart, F. Dong, C. Tandy, and D. Moodie, "Fibre optic techniques for remote spectroscopic methane detection—from concept to system realisation," *Sensor. Actuat. B-Chem* 51, 25-37 (1998).
- [8] B. Lee, "Review of the present status of optical fiber sensors," *Opt. Fiber Technol.* 9, 57-79 (2003).
- [9] J. Shemshad, S. M. Aminossadati, and M. S. Kizil, "A review of developments in near infrared methane detection based on tunable diode laser," *Sensor. Actuat. B-Chem* 171, 77-92 (2012).
- [10] J. Hodgkinson and R. P. Tatam, "Optical gas sensing: a review," *Meas. Sci. Technol.* 24, 012004 (2013).
- [11] W. Jin, H. Ho, Y. Cao, J. Ju, and L. Qi, "Gas detection with micro-and nano-engineered optical fibers," *Opt. Fiber Technol.* 19, 741-759 (2013).
- [12] K. Chan, H. Ito, H. Inaba, and T. Furuya, "10 km-long fibre-optic remote sensing of CH₄

-
- gas by near infrared absorption,” *Appl. Phys. B* 38, 11-15 (1985).
- [13] J. Dakin, C. Wade, D. Pinchbeck, and J. Wykes, “A novel optical fibre methane sensor,” *Fibre Optics '87* 254-260 (1987).
- [14] J. U. White, “Very long optical paths in air,” *J. Opt. Soc. Am.* 66, 411-416 (1976).
- [15] D. R. Herriott and H. J. Schulte, “Folded optical delay lines,” *Appl. Opt.* 4, 883-889 (1965).
- [16] T. McGarvey, A. Conjusteau, and H. Mabuchi, “Finesse and sensitivity gain in cavity-enhanced absorption spectroscopy of biomolecules in solution,” *Opt. Express* 14, 10441-10451 (2006).
- [17] A. O’ Keefe and D. A. Deacon, “Cavity ring-down optical spectrometer for absorption measurements using pulsed laser sources,” *Rev. Sci. Instrum.* 59, 2544-2551 (1988).
- [18] P. Kluczynski and O. Axner, “Theoretical description based on Fourier analysis of wavelength-modulation spectrometry in terms of analytical and background signals,” *Appl. Opt.* 38, 5803-5815 (1999).
- [19] P. Kluczynski, J. Gustafsson, Å. M. Lindberg, and O. Axner, “Wavelength modulation absorption spectrometry—an extensive scrutiny of the generation of signals,” *Spectrochimica Acta Part B: Atomic Spectroscopy* 56, 1277-1354 (2001).
- [20] S. Schilt, L. Thevenaz, and P. Robert, “Wavelength modulation spectroscopy: combined frequency and intensity laser modulation,” *Appl. Opt.* 42, 6728-6738 (2003).
- [21] C. Haisch, “Photoacoustic spectroscopy for analytical measurements,” *Meas. Sci. Technol.* 23, 012001 (2012).
- [22] S. Bialkowski, *Photothermal spectroscopy methods for chemical analysis*, John Wiley & Sons (1996).
- [23] H. L. Ho, W. Jin, and M. S. Demokan, “Quantitative measurement of acetylene by using external-cavity tunable diode laser,” *Photonics East'99* 124-133 (1999).
- [24] J. Sa, Y. Chen, G. Zhang, Z. Zhou, and L. Cui, “Gas cell based on cascaded GRIN lens for optical fiber gas sensor,” in *Proc. of SPIE* 67234I-1 (2007).
- [25] H. Ho, J. Ju, and W. Jin, “Fiber optic gas detection system for health monitoring of oil-filled transformer,” in *Proc. of SPIE* 75030T-1 (2009).
- [26] C. Hussey and J. Minelly, “Optical fibre polishing with a motor-driven polishing wheel,”

-
- Electron. Lett. 24, 805-807 (1988).
- [27] G. Brambilla, V. Finazzi, and D. J. Richardson, "Ultra-low-loss optical fiber nanotapers," *Opt. Express* 12, 2258-2263 (2004).
- [28] G. Brambilla, "Optical fibre nanotaper sensors," *Opt. Fiber Technol.* 16, 331-342 (2010).
- [29] F. Muhammad, G. Stewart, and W. Jin, "Sensitivity enhancement of D-fibre methane gas sensor using high-index overlay," *IEE Proceedings J (Optoelectronics)* 140, 115-118 (1993).
- [30] Y. L. Hoo, W. Jin, C. Shi, H. L. Ho, D. N. Wang, and S. C. Ruan, "Design and modeling of a photonic crystal fiber gas sensor," *Appl. Opt.* 42, 3509-3515 (2003).
- [31] T. M. Monro, S. Warren-Smith, E. P. Schartner, A. François, S. Heng, H. Ebendorff-Heidepriem, and S. Afshar V, "Sensing with suspended-core optical fibers," *Opt. Fiber Technol.* 16, 343-356 (2010).
- [32] Y. Hoo, W. Jin, H. L. Ho, D. Wang, and R. S. Windeler, "Evanescent-wave gas sensing using microstructure fiber," *Opt. Eng.* 41, 8-9 (2002).
- [33] C. Hensley, D. H. Broaddus, C. B. Schaffer, and A. L. Gaeta, "Photonic band-gap fiber gas cell fabricated using femtosecond micromachining," *Opt. Express* 15, 6690-6695 (2007).
- [34] A. van Brakel, C. Grivas, M. N. Petrovich, and D. J. Richardson, "Micro-channels machined in microstructured optical fibers by femtosecond laser," *Opt. Express* 15, 8731-8736 (2007).
- [35] P. Russell, "Photonic crystal fibers," *science*, 299, 358-362 (2003).
- [36] J. M. Fini, J. W. Nicholson, R. S. Windeler, E. M. Monberg, L. Meng, B. Mangan, A. DeSantolo, and F. V. DiMarcello, "Low-loss hollow-core fibers with improved single-modedness," *Opt. Express* 21, 6233-6242 (2013).
- [37] R. Cregan, B. Mangan, J. Knight, T. Birks, P. S. J. Russell, P. Roberts, and D. Allan, "Single-mode photonic band gap guidance of light in air," *science* 285, 1537-1539 (1999).
- [38] Y. Hoo, W. Jin, H. Ho, J. Ju, and D. Wang, "Gas diffusion measurement using hollow-core photonic bandgap fiber," *Sensor. Actuat. B-Chem* 105, 183-186 (2005).
- [39] T. Ritari, J. Tuominen, H. Ludvigsen, J. Petersen, T. Sørensen, T. Hansen, and H. Simonsen, "Gas sensing using air-guiding photonic bandgap fibers," *Opt. Express* 12, 4080-4087, (2004).
- [40] A. Cubillas, M. Silva-Lopez, J. Lazaro, O. Conde, M. N. Petrovich, and J. M.

-
- Lopez-Higuera, "Methane detection at 1670-nm band using a hollow-core photonic bandgap fiber and a multiline algorithm," *Opt. Express* 15, 17570-17576 (2007).
- [41] Y. Hoo, S. Liu, H. L. Ho, and W. Jin, "Fast response microstructured optical fiber methane sensor with multiple side-openings," *IEEE Photonics Technol. Lett.* 22, 296-298 (2010).
- [42] M. Petrovich, A. Heidt, N. Wheeler, N. Baddela, and D. Richardson, "High sensitivity methane and ethane detection using low-loss mid-IR hollow-core photonic bandgap fibers," in *23rd International Conference on Optical Fiber Sensors (OFS2014)*, 91573P-91573P-4 (2014).
- [43] J. Nwaboh, J. Hald, J. Lyngsø, J. Petersen, and O. Werhahn, "Measurements of CO₂ in a multipass cell and in a hollow-core photonic bandgap fiber at 2 μ m," *Appl. Phys. B* 110, 187-194 (2013).
- [44] R. M. Wynne, B. Barabadi, K. J. Creedon, and A. Ortega, "Sub-minute response time of a hollow-core photonic bandgap fiber gas sensor," *J. Lightwave Technol.* 27, 1590-1596 (2009).
- [45] J. Parry, B. Griffiths, N. Gayraud, E. McNaghten, A. Parkes, W. MacPherson, and D. Hand, "Towards practical gas sensing with micro-structured fibres," *Meas. Sci. Technol.* 20, 075301 (2009).
- [46] J. Carvalho, H. Lehmann, H. Bartelt, F. Magalhaes, R. Amezcua-Correa, J. Santos, J. Van Roosbroeck, F. Araújo, L. Ferreira, and J. Knight, "Remote system for detection of low-levels of methane based on photonic crystal fibres and wavelength modulation spectroscopy," *J. Sens.* 2009, 398403 (2009).
- [47] F. Yang, W. Jin, Y. Lin, C. Wang, H. L. Ho, and Y. Tan, "Hollow-core Microstructured Optical Fiber Gas Sensors," *J. Lightwave Technol.* 35, 3413-3424 (2017).
- [48] A. Miklós, P. Hess, and Z. Bozóki, "Application of acoustic resonators in photoacoustic trace gas analysis and metrology," *Rev. Sci. Instrum.* 72, 1937-1955 (2001).
- [49] T. Schmid, "Photoacoustic spectroscopy for process analysis," *Anal. Bioanal. Chem.* 384, 1071-1086 (2006).
- [50] A. Elia, P. M. Lugarà, C. Di Franco, and V. Spagnolo, "Photoacoustic techniques for trace gas sensing based on semiconductor laser sources," *Sensors* 9, 9616-9628 (2009).

-
- [51] M. Viegerov, "Eine Methode der gasanalyse, beruhend auf der optisch-akustischen tyndall-röntgenerscheinung," in Dokl. Akad. Nauk SSSR 687-688 (1938).
- [52] E. L. Kerr and J. G. Atwood, "The laser illuminated absorptivity spectrophone: a method for measurement of weak absorptivity in gases at laser wavelengths," Appl. Opt. 7, 915-921 (1968).
- [53] L. Kreuzer, "Ultralow gas concentration infrared absorption spectroscopy," J. Appl. Phys. 42, 2934-2943 (1971).
- [54] L. Kreuzer, N. Kenyon, and C. Patel, "Air pollution: sensitive detection of ten pollutant gases by carbon monoxide and carbon dioxide lasers," Science 177, 347-349 (1972).
- [55] M. B. Pushkarsky, I. G. Dunayevskiy, M. Prasanna, A. G. Tsekoun, R. Go, and C. K. N. Patel, "High-sensitivity detection of TNT," Proceedings of the National Academy of Sciences 103, 19630-19634 (2006).
- [56] P. A. Martin, "Near-infrared diode laser spectroscopy in chemical process and environmental air monitoring," Chem. Soc. Rev. 31, 201-210 (2002).
- [57] C. Dewey Jr, R. Kamm, and C. Hackett, "Acoustic amplifier for detection of atmospheric pollutants," Appl. Phys. Lett. 23, 633-635 (1973).
- [58] R. D. Kamm, "Detection of weakly absorbing gases using a resonant optoacoustic method," J. Appl. Phys. 47, 3550-3558 (1976).
- [59] L.-G. Rosengren, "Optimal optoacoustic detector design," Appl. Opt. 14, 1960-1976 (1975).
- [60] C. Patel and R. Kerl, "A new optoacoustic cell with improved performance," Appl. Phys. Lett. 30, 578-579 (1977).
- [61] R. Gerlach and N. Amer, "Brewster window and windowless resonant spectrophones for intracavity operation," Appl. Phys. 23, 319-326 (1980).
- [62] S. Bernegger and M. Sigrist, "Longitudinal resonant spectrophone for CO-laser photoacoustic spectroscopy," Appl. Phys. B 44, 125-132 (1987).
- [63] F. Harren, J. Reuss, E. Woltering, and D. Bicanic, "Photoacoustic measurements of agriculturally interesting gases and detection of C₂H₄ below the ppb level," Appl. Spectrosc. 44, 1360-1368 (1990).
- [64] F. Harren, F. Bijnen, J. Reuss, L. Voeselek, and C. Blom, "Sensitive intracavity

- photoacoustic measurements with a CO₂ waveguide laser,” *Appl. Phys. B* 50, 137-144 (1990).
- [65] P. Meyer and M. Sigrist, “Atmospheric pollution monitoring using CO₂-laser photoacoustic spectroscopy and other techniques,” *Rev. Sci. Instrum.* 61, 1779-1807 (1990).
- [66] Z. Bozóki, J. Sneider, G. Szabó, A. Miklós, M. Serényi, G. Nagy, and M. Fehér, “Intracavity photoacoustic gas detection with an external cavity diode laser,” *Appl. Phys. B* 63, 399-401 (1996).
- [67] A. Boschetti, D. Bassi, E. Iacob, S. Iannotta, L. Ricci, and M. Scotoni, “Resonant photoacoustic simultaneous detection of methane and ethylene by means of a 1.63- μ m diode laser,” *Appl. Phys. B* 74, 273-278 (2002).
- [68] M. E. Webber, M. Pushkarsky, and C. K. N. Patel, “Fiber-amplifier-enhanced photoacoustic spectroscopy with near-infrared tunable diode lasers,” *Appl. Opt.* 42, 2119-2126 (2003).
- [69] J. Li, X. Gao, L. Fang, W. Zhang, and H. Cha, “Resonant photoacoustic detection of trace gas with DFB diode laser,” *Opt. Laser Technol.* 39, 1144-1149 (2007).
- [70] Y. Peng, W. Zhang, L. Li, and Q. Yu, “Tunable fiber laser and fiber amplifier based photoacoustic spectrometer for trace gas detection,” *Spectrochim. Acta Part A* 74, 924-927 (2009).
- [71] L.-y. Hao, S. Qiang, G.-r. Wu, L. Qi, D. Feng, and Q.-s. Zhu, “Cylindrical mirror multipass Lissajous system for laser photoacoustic spectroscopy,” *Rev. Sci. Instrum.* 73, 2079-2085 (2002).
- [72] J. Rey, D. Marinov, D. Vogler, and M. Sigrist, “Investigation and optimisation of a multipass resonant photoacoustic cell at high absorption levels,” *Appl. Phys. B* 80, 261-266 (2005).
- [73] J. Saarela, J. Sand, T. Sorvajärvi, A. Manninen, and J. Toivonen, “Transversely excited multipass photoacoustic cell using electromechanical film as microphone,” *Sensors* 10, 5294-5307 (2010).
- [74] Y. Cao, N. P. Sanchez, W. Jiang, W. Ren, R. Lewicki, D. Jiang, R. J. Griffin, and F. K. Tittel, “Multi-pass absorption spectroscopy for H₂O₂ detection using a CW DFB-QCL,” *Adv. Opt. Techn.* 3, 549-558 (2014).
- [75] A. Rossi, R. Buffa, M. Scotoni, D. Bassi, S. Iannotta, and A. Boschetti, “Optical

-
- enhancement of diode laser-photoacoustic trace gas detection by means of external Fabry-Perot cavity,” *Appl. Phys. Lett.* 87, 041110 (2005).
- [76] M. Hippler, C. Mohr, K. A. Keen, and E. D. McNaghten, “Cavity-enhanced resonant photoacoustic spectroscopy with optical feedback cw diode lasers: A novel technique for ultratrace gas analysis and high-resolution spectroscopy,” *J. Chem. Phys.* 133, 044308 (2010).
- [77] A. Kosterev, Y. A. Bakhirkin, R. Curl, and F. Tittel, “Quartz-enhanced photoacoustic spectroscopy,” *Opt. Lett.* 27, 1902-1904 (2002).
- [78] A. A. Kosterev and F. K. Tittel, “Ammonia detection by use of quartz-enhanced photoacoustic spectroscopy with a near-IR telecommunication diode laser,” *Appl. Opt.* 43, 6213-6217 (2004).
- [79] A. A. Kosterev, F. K. Tittel, D. V. Serebryakov, A. L. Malinovsky, and I. V. Morozov, “Applications of quartz tuning forks in spectroscopic gas sensing,” *Rev. Sci. Instrum.* 76, 043105 (2005).
- [80] K. Liu, X. Guo, H. Yi, W. Chen, W. Zhang, and X. Gao, “Off-beam quartz-enhanced photoacoustic spectroscopy,” *Opt. Lett.* 34, 1594-1596 (2009).
- [81] K. Liu, H. Yi, A. A. Kosterev, W. Chen, L. Dong, L. Wang, T. Tan, W. Zhang, F.K. Tittel, and X. Gao, “Trace gas detection based on off-beam quartz enhanced photoacoustic spectroscopy: Optimization and performance evaluation,” *Rev. Sci. Instrum.* 81, 103103 (2010).
- [82] L. Dong, A. A. Kosterev, D. Thomazy, and F. K. Tittel, “QEPAS spectrophones: design, optimization, and performance,” *Appl. Phys. B* 100, 627-635 (2010).
- [83] J. Kauppinen, K. Wilcken, I. Kauppinen, and V. Koskinen, “High sensitivity in gas analysis with photoacoustic detection,” *Microchem. J.* 76, 151-159 (2004).
- [84] T. Laurila, H. Cattaneo, V. Koskinen, J. Kauppinen, and R. Hernberg, “Diode laser-based photoacoustic spectroscopy with interferometrically-enhanced cantilever detection,” *Opt. Express* 13, 2453-2458 (2005).
- [85] V. Koskinen, J. Fonsen, K. Roth, and J. Kauppinen, “Cantilever enhanced photoacoustic detection of carbon dioxide using a tunable diode laser source,” *Appl. Phys. B* 86, 451-454

- (2007).
- [86] T. Laurila, H. Cattaneo, V. Koskinen, J. Kauppinen, and R. Hernberg, "Diode laser-based photoacoustic spectroscopy with interferometrically-enhanced cantilever detection: erratum," *Opt. Express* 14, 4195 (2006).
- [87] V. Koskinen, J. Fonsen, K. Roth, and J. Kauppinen, "Progress in cantilever enhanced photoacoustic spectroscopy," *Vib. Spectrosc.* 48, 16-21 (2008).
- [88] Y. Tan, C. Zhang, W. Jin, F. Yang, H. L. Ho, and J. Ma, "Optical fiber photoacoustic gas sensor with graphene nano-mechanical resonator as the acoustic detector," *IEEE J.Sel. Top. Quant. Electronics* 23, 5600211 (2017).
- [89] Y. Cao, W. Jin, L. H. Ho, and Z. Liu, "Evanescent-wave photoacoustic spectroscopy with optical micro/nano fibers," *Opt. Lett.* 37, 214-216 (2012).
- [90] D. Leslie, G. Trusty, A. Dandridge, and T. Giallorenzi, "Fibre-optic spectrophone," *Electron. Lett.* 17, 581-582 (1981).
- [91] J. Breguet, J.-P. Pellaux, and N. Gisin, "Photoacoustical detection of trace gases with an optical microphone," in *10th Optical Fibre Sensors Conference* 457-460 (1994).
- [92] Q. Wang, J. Wang, L. Li, and Q. Yu, "An all-optical photoacoustic spectrometer for trace gas detection," *Sensor. Actuat. B-Chem* 153, 214-218 (2011).
- [93] Y. Cao, W. Jin, H. L. Ho, and J. Ma, "Miniature fiber-tip photoacoustic spectrometer for trace gas detection," *Opt. Lett.* 38, 434-436 (2013).
- [94] P. Beard, F. Perennes, E. Draguioti, and T. Mills, "Optical fiber photoacoustic–photothermal probe," *Opt. Lett.* 23, 1235-1237 (1998).
- [95] O. C. Akkaya, O. Kilic, M. J. Dignonnet, G. S. Kino, and O. Solgaard, "High-sensitivity thermally stable acoustic fiber sensor," in *IEEE Sensors* 1148-1151 (2010).
- [96] F. Xu, D. Ren, X. Shi, C. Li, W. Lu, L. Lu, et al., "High-sensitivity Fabry–Perot interferometric pressure sensor based on a nanothick silver diaphragm," *Opt. Lett.* 37, 133-135 (2012).
- [97] F. Guo, T. Fink, M. Han, L. Koester, J. Turner, and J. Huang, "High-sensitivity, high-frequency extrinsic Fabry–Perot interferometric fiber-tip sensor based on a thin silver diaphragm," *Opt. Lett.* 37, 1505-1507 (2012).

- [98] J. Ma, H. Xuan, H. L. Ho, W. Jin, Y. Yang, and S. Fan, "Fiber-optic Fabry–Perot acoustic sensor with multilayer graphene diaphragm," *IEEE Photonics Technol. Lett.* 10, 932-935 (2013).
- [99] C. C. Davis and S. J. Petuchowski, "Phase fluctuation optical heterodyne spectroscopy of gases," *Appl. Opt.* 20, 2539-2554 (1981).
- [100] M. A. Owens, C. C. Davis, and R. R. Dickerson, "A photothermal interferometer for gas-phase ammonia detection," *Anal. Chem.* 71, 1391-1399 (1999).
- [101] N. D. Weston, P. Sakthivel, and P. Mukherjee, "Ultrasensitive spectral trace detection of individual molecular components in an atmospheric binary mixture," *Appl. Opt.* 32, 828-835 (1993).
- [102] A. Sedlacek and J. Lee, "Photothermal interferometric aerosol absorption spectrometry," *Aerosol Sci. Technol.* 41, 1089-1101 (2007).
- [103] W. Jin, Y. Cao, F. Yang, and H. L. Ho, "Ultra-sensitive all-fibre photothermal spectroscopy with large dynamic range," *Nature communications* 6,6767 (2015).
- [104] F. Yang, Y. Tan, W. Jin, Y. Lin, Y. Qi, and H. L. Ho, "Hollow-core fiber Fabry–Perot photothermal gas sensor," *Opt. Lett.* 41, 3025-3028 (2016).

Chapter 2

Basics of gas absorption spectroscopy

2.1 Introduction

In this chapter, we will introduce the basic principles of direct absorption spectroscopy (DAS) and wavelength modulation spectroscopy (WMS).

2.2 Principle of direct absorption spectroscopy

2.2.1 Beer-Lambert law

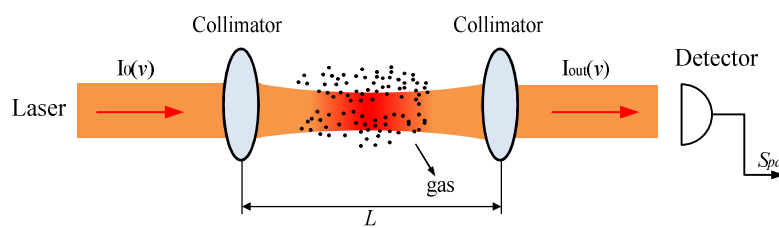


Fig. 2.1 Schematic of an optical absorption sensor.

Figure 2.1 shows the schematic of a gas sensor based on direct absorption. The basic process is as follows: When a laser beam with specific wavelength located near the absorption line of the target gas propagates through the gas sample, part of the optical power will be absorbed by the gas sample and the transmitted power can be detected. The amount of absorption depending on the gas concentration and absorption path length can be determined by comparing the incident power to the transmitted power through the target gas. According to the Beer-Lambert Law, the transmitted light intensity $I_{out}(\nu)$ passing through the gas sample with an absorption path length of L , can be expressed as [1, 2]

$$I_{out}(\nu) = I_0(\nu) \exp(-\alpha(\nu)L) \quad (2.1)$$

where $I_0(\nu)$ is the input light intensity at wavenumber ν (cm^{-1}), and $\alpha(\nu)$ is the gas absorption, which is expressed as [1]

$$\alpha(\nu) = NS\chi(\nu)L = CN_{tot}S\chi(\nu)L \quad (2.2)$$

The gas absorption is determined by the gas concentration C , line strength S , lineshape function $\chi(\nu)$ and an absorption path length L . N_{tot} is the total gas molecular density expressed as $N_{tot} = N_L \frac{296}{T} p$ at temperature T and pressure p with the Loschmidt number of $N_L = 2.479 \times 10^{19} \text{ mol} \cdot \text{cm}^{-3} \cdot \text{atm}^{-1}$.

The lineshape functions $\chi(\nu)$ are referred to three typical types function, i.e. Gaussian type, Lorentzian type and Voigt type [3]. The line strength S of an absorption transition can be related to the population in the lower quantum state N_n , and the probability of the transition between lower state n and higher state m as [4, 5]

$$S = \frac{N_n}{N} \frac{h\nu_{nm}}{c} B_{nm} \left[1 - \exp\left(-\frac{h\nu_{nm}}{kT}\right) \right] \quad (2.3)$$

where B_{nm} is the Einstein coefficient, c is light velocity in vacuum and k is Boltzmann constant. Figure 2.2 lists the absorption spectrums of several gas in the near-infrared (NIR) region.

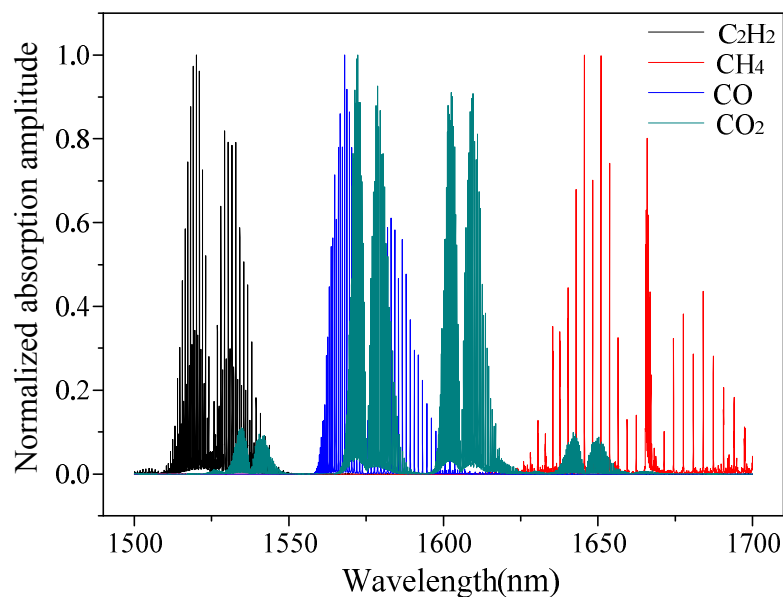


Fig. 2.2 Absorption spectrums of several gas in the near-infrared region [4].

2.2.2 Absorption lineshape

The gas absorption will not appear at a single frequency profile but has a distribution around the absorption line center due to molecule collisional broadening. The lineshape of absorption profile mainly depends on the dominant broadening mechanism.

If the lineshape results from a homogeneous broadening mechanism (natural/lifetime or collision), the absorption lineshape will be represented by a Lorentzian lineshape, which can be expressed by [1, 6]

$$\bar{\chi}_L(\nu) = \frac{\gamma_L^2}{(\nu - \nu_0)^2 + \gamma_L^2} \quad (2.4)$$

where γ_L is the half width at half maximum (HWHM) of the Lorentzian lineshape in cm^{-1} , ν_0 is the line center wavenumber in cm^{-1} .

If the lineshape results from an inhomogeneous broadening mechanism (Doppler broadening) induced by the random thermal motion of gas molecules, the absorption lineshape will be represented by a Gaussian lineshape, which can be expressed by [1]

$$\bar{\chi}_G(\nu) = \exp[-4 \ln 2 (\nu - \nu_0)^2 / (2\gamma_D)^2] \quad (2.5)$$

where γ_D is the Doppler HWHM of absorption line in cm^{-1} , and it can be written as

$$\gamma_D = \nu_0 / c \sqrt{2kT \ln 2 / m} \quad (2.6)$$

where T (in Kelvin) is temperature in K , and m is the molecular weight of the target gas.

Figure 2.3 shows the Peak normalized Lorentzian (solid curve) and Gaussian (dashed curve) absorption lineshapes with the same linewidth. We can see that the Gaussian profile decreases rapidly when the wavenumber is far from the center compared with the Lorentzian profile.

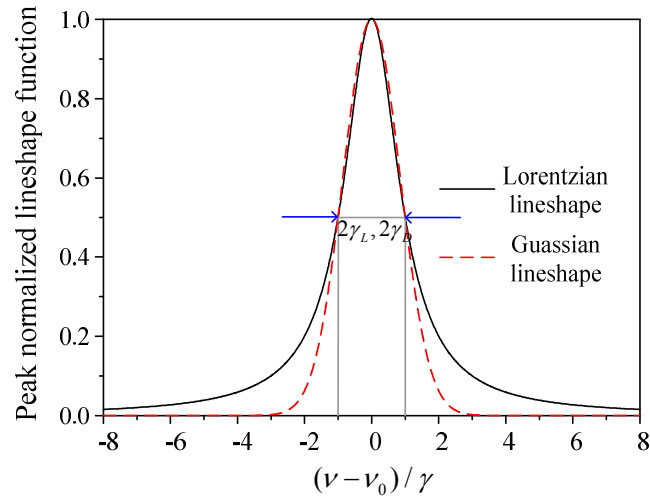


Fig. 2.3 Peak normalized Lorentzian and Gaussian lineshapes.

If the actual broadening is a combination of Doppler, natural and collisional broadening, the absorption lineshape will be represented by a Voigt lineshape, which can be expressed by [3]

$$\bar{\chi}_V(\nu) = \bar{\chi}_G(\nu_0) \frac{\sqrt{\ln 2} \gamma_L / \gamma_D}{\pi} \int_{-\infty}^{+\infty} \frac{\exp(-(\sqrt{\ln 2} \nu / \gamma_D)^2)}{(\sqrt{\ln 2} \gamma_L / \gamma_D)^2 + (\sqrt{\ln 2} (\nu - \nu_0) / \gamma_D - \sqrt{\ln 2} \nu / \gamma_D)^2} d(\sqrt{\ln 2} \nu / \gamma_D) \quad (2.7)$$

The line width (HWHM) of Voigt lineshape can be estimated by [7]

$$\gamma_V = 0.534\gamma_L + \sqrt{0.2166\gamma_L^2 + \gamma_D^2} \quad (2.8)$$

For small Voigt parameter of $\sqrt{\ln 2}\gamma_L/\gamma_D$, Doppler broadening will be the prevailing broadening mechanism, Voigt profile approaches Gaussian profile. When the Voigt parameter becomes larger, the collisional broadening dominates, Voigt profile approaches Lorentzian profile.

2.2.3 The detector signal

As shown in Figure 2.1, when a laser beam transmits through an empty gas cell and is received by a photodetector, it will produce a current proportional to the power of the laser beam P which is defined as the area integrated intensity

$$P = \int I dA \quad (2.9)$$

where A is the laser beam area. The detector current is given by [8, 9]

$$i_{pd} = \eta_c P \quad (2.10)$$

where η_c (A/W) is the current responsivity of the detector, then the detector signal, S_{pd} (V), is given by [9]

$$S_{pd} = \eta P = \eta_c g_{pd} Z_{pd} P = g_{pd} Z_{pd} i_{pd} \quad (2.11)$$

Where η (V/W) is an instrumentation factor with $\eta = \eta_c g_{pd} Z_{pd}$, g_{pd} is the voltage gain of the detector amplifier and Z_{pd} is the input impedance of the current to voltage converter (Ω).

When the gas cell is filled with weakly absorbing gas sample, the detector signal is given by [9]

$$S_{pd} = \eta P_0 [1 - \alpha(\nu)] = S_1 - S_2 \quad (2.12)$$

with the background signal $S_1 = \eta P_0$ and absorption signal $S_2 = \eta P_0 \alpha(\nu)$ where P_0 is the light power incident on the detector in the absence of the gas sample.

2.2.4 Noise and detection limit

2.2.4.1 Noise

The detection limit of a technique is typically limited by the system noise. The noise that may affect the gas absorption signal are mainly from the laser source, technical noise, residual amplitude modulation (RAM), background signal and the shot noise [1]. Table 2.1 summarizes the different types of noise sources and the corresponding method to reduce the noise.

Table 2.1 Noise that may affect the gas detected signal

Noise source		Effective way to reduce the noise	
Laser source	Amplitude noise, or 1/f noise	Modulation technique	
Technical noise	Electrical noise, mechanical noise	Modulation technique	
RAM	Induces background signals	Modulation technique	
Background signal			
Shot noise	Random fluctuation in the electrical current		

2.2.4.2 Detection limit

The sensitivity of a technique is determined by the signal-to-noise ratio (SNR) of the system, which is calculated by comparing the peak absorption signal to the root-mean-square (rms) of the background signal such as the noise level. A

well-developed gas absorption system has a detection limit close to the shot noise level. Shot noise is the fundamental limit of the noise which determines the detection limit. The shot noise is induced by the random fluctuations in the electrical current, which depends on the power incident on the detector and the detection bandwidth.

The shot noise current can be written as [9, 10]

$$i_{shot} = \sqrt{2e\Delta f i_{pd}} \quad (2.13)$$

where Δf is the detection bandwidth and elementary charge $e = 1.6 \times 10^{-19}$ C. Then the signal corresponding to the shot noise current is given by Eq.(2.10) as

$$S_{shot} = g_{pd} Z_{pd} i_{shot} = g_{pd} Z_{pd} \sqrt{2e\Delta f \eta_c P_0} \quad (2.14)$$

The minimum detectable gas absorption limited by shot noise can be calculated by

setting S_2 in $S_2 = \eta P_0 \alpha(\nu)$ by $S_2 = S_{shot}$ for DAS, then we have

$$(\alpha_0)_{\min}^{DAS} = \sqrt{\frac{2e\Delta f}{\eta_c P_0}} \quad (2.15)$$

For $\Delta f = 1$ Hz, $\eta_c = 1$ A/W and $P_0 = 1$ mW, the shot noise limited absorption $(\alpha_0)_{\min}^{DAS}$ is calculated to be 2×10^{-8} . However, for DAS, the shot noise limit will not be achieved since the detected signal is limit by other noises such as technical noise, 1/frequency noise and thermal noise. So many other techniques for high detected signal and low noise have been developed, for example, WMS, which will be introduced in the next part.

2.3 Wavelength modulation spectroscopy (WMS)

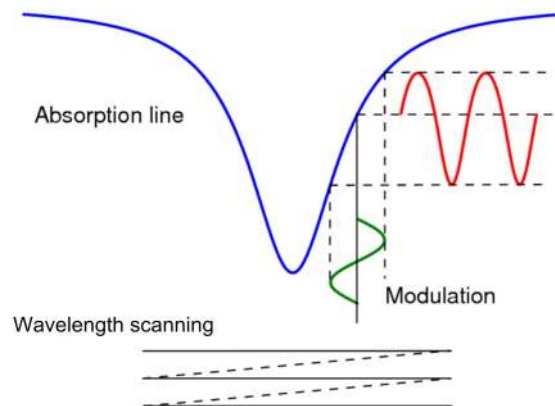
WMS with harmonic detection is a suitable and important technique for LAS since it can reduce the background noise and achieve high detection sensitivity [11-14]. The basic

process of WMS is shown in Figure 2.4 (a) and the experimental setup is shown in Figure 2.4 (b), which is followed by the three steps:

(1) The wavelength of the distributed feedback semiconductor (DFB) laser is firstly tuned to the absorption line and scanned across it periodically by a temperature laser controller, at the same time the wavelength is modulated sinusoidally at a higher frequency of f (often in several or tens of kHz ~MHz range) by a current laser controller,, as shown in Figure 2.4 (a).

(2) The light is propagating through a gas cell where the light power is absorbed, and the transmitted light is detected by a photodiode as shown in Figure 2.4 (b).

(3) The detector signal consists of a series harmonic signals of the gas characteristics, which is induced by the interaction between the modulated wavelength and the gas absorption line function. This signal is then demodulated by a lock-in amplifier.



(a)

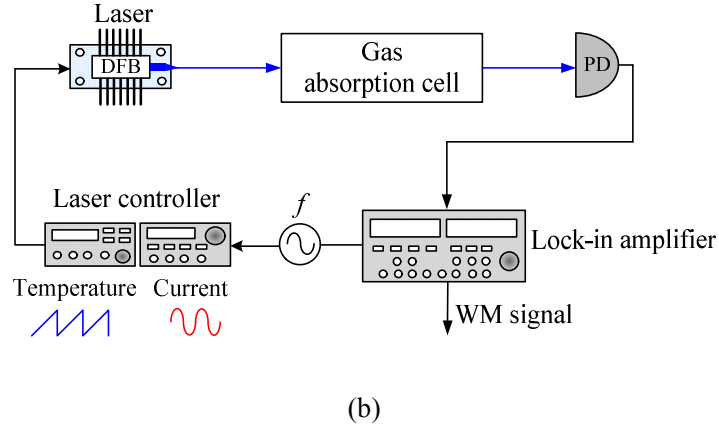


Fig.2.4. (a) The basic process of WMS [3]. (b) Schematic of the general setup of WMS.

In Eq. (2.1), $\alpha(\nu) = \alpha_0 \bar{\chi}(\nu)$ is the gas absorption, α_0 is the peak absorption and $\bar{\chi}(\nu)$ is the peak-normalized lineshape function. For a Lorentzian profile, $\bar{\chi}(\nu)$ can be expressed by Eq. (2.4) as [3]

$$\bar{\chi}(\nu) = \frac{1}{1 + [(\nu - \nu_0) / \gamma]^2} \quad (2.16)$$

where ν_0 is the wavenumber of the absorption line center and γ is the linewidth (HWHM) of the absorption line (cm^{-1}). Let $x = (\nu - \nu_0) / \gamma$, then Eq. (2.16) becomes

$$\bar{\chi}(\nu) = \frac{1}{1 + x^2}.$$

When the wavelength is modulated at a frequency of ω , wavenumber ν can be written as

$$\nu = \bar{\nu} - \delta\nu \cos(\omega t - \psi) \quad (2.17)$$

Where $\bar{\nu}$ is the central wavenumber of the input laser, $\delta\nu$ is the wavenumber modulation, ψ is the phase delay. Then x becomes

$$\begin{aligned}
x &= (\nu - \nu_0) / \gamma = [\bar{\nu} - \delta\nu \cos(\omega t - \psi) - \nu_0] / \gamma \\
&= \frac{\bar{\nu} - \nu_0}{\gamma} - \frac{\delta\nu}{\gamma} \cos(\omega t - \psi) = \bar{x} - m \cos(\omega t - \psi)
\end{aligned} \tag{2.18}$$

with $\bar{x} = (\bar{\nu} - \nu_0) / \gamma$ and $m = \delta\nu / \gamma$ is the modulation depth, so the peak-normalized lineshape function $\bar{\chi}(\nu)$ becomes

$$\bar{\chi}(\nu) = \frac{1}{1 + [\bar{x} - m \cos(\omega t - \psi)]^2} \tag{2.19}$$

And it can be expanded into Fourier series by [15]

$$\bar{\chi}(\nu) = a_0 + \sum_{n=1}^{\infty} a_n \cos(n\theta) = a_0 + \sum_{n=1}^{\infty} a_n \cos(n\omega t - n\psi) \tag{2.20}$$

with

$$a_0 = \frac{1}{\pi} \int_0^{\pi} \bar{\chi}(\theta) d\theta = \frac{1}{\pi} \int_0^{\pi} \frac{1}{1 + [\bar{x} - m \cos(\theta)]^2} d\theta \tag{2.21}$$

$$a_n = \frac{2}{\pi} \int_0^{\pi} \bar{\chi}(\theta) \cos(n\theta) d\theta = \frac{2}{\pi} \int_0^{\pi} \frac{\cos(n\theta)}{1 + [\bar{x} - m \cos(\theta)]^2} d\theta \tag{2.22}$$

where $\theta = \omega t - \psi$, a_0 and a_n are the harmonic coefficients. The first four harmonics of absorption coefficient with different modulation depth is plotted in Figure 2.5. We can see that only the second harmonic a_2 achieve a maximum value at the absorption line center and its maximum values depends on the modulation depth m . When $m=2.2$ (i.e. wavenumber modulation $\delta\nu$ is 2.2 times of the absorption linewidth), then the second harmonic signal achieves its maximum [3].

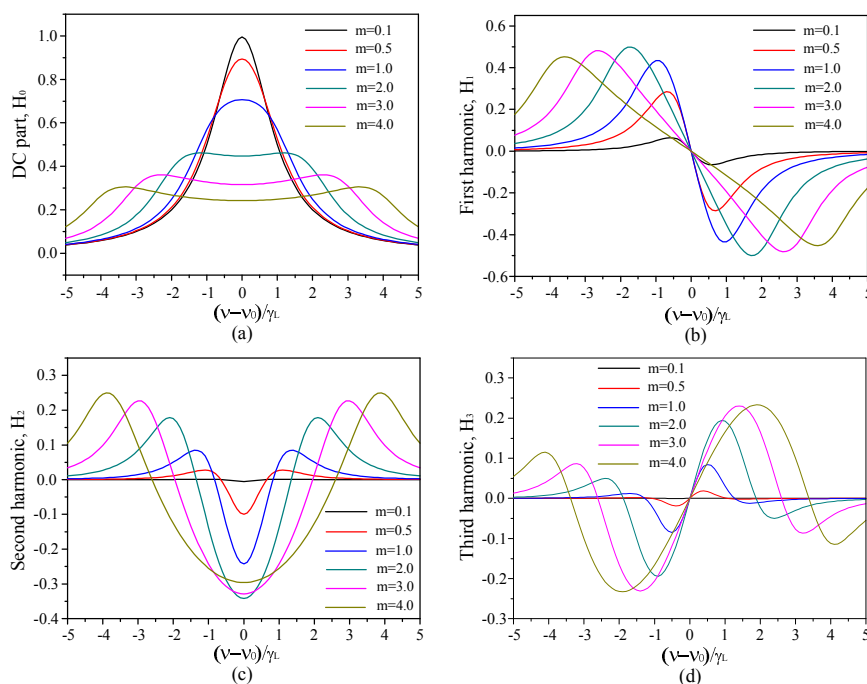


Fig. 2.5 The first four harmonic coefficients for different modulation depth.

In the wavelength modulation scheme, the laser wavelength is tuned to the absorption line and scanned across it periodically. Meanwhile, a sinusoidal current is injected into the laser controller to result in a modulation on the laser wavelength. However, for a semiconductor laser, a modulation on the injected current can simultaneously result in modulation of the laser wavelength and optical intensity (IM). The intensity modulation is the undesired residual signal and it is called residual intensity modulation (RIM). The RIM mainly affects the relative amplitude of the two branches for the signals, giving an asymmetric signal profile. In the absorption line center, the second harmonic signal maintains its profile even for a large residual intensity modulation compared with the first harmonic signal which shows a zero value at the absorption center. The advantages of wavelength modulation with second harmonic detection are high sensitivity with larger signal, independent signal profile on RIM at the absorption center, lower background noise.

2.4 Summary

In this chapter, basic of DAS is introduced first, which includes the Beer-Lamber Law, absorption lineshapes, detector signal and detection limit. Then WMS with second harmonic detection is presented and analyzed. This chapter shows the basic knowledge for the absorption based gas detection in this thesis. In the following several chapters, we will introduce the detection techniques based on this chapter.

References of Chapter 2

- [1] F. Schmidt, "Laser-based absorption spectrometry: development of NICE-OHMS towards ultra-sensitive trace species detection," PhD Thesis, Umeå University (2007).
- [2] G. Stewart, J. Norris, D. Clark, and B. Culshaw, "Evanescent-wave chemical sensors--a theoretical evaluation," *International J. of Optoelectron.* 6, 227-238 (1991).
- [3] Y. Cao, "Quartz-enhanced photoacoustic spectroscopy and its association with fiber-optic devices," PhD Thesis, The Hong Kong Polytechnic University (2012).
- [4] L. S. Rothman, D. Jacquemart, A. Barbe, D. C. Benner, M. Birk, L. Brown, M. Carleer, C. Chackerian, Jr, K. Chance, L. Coudert, V. Dana, V. Devi, J. Flaud, R. Gamache, A. Goldman, J. Hartmann, K. Jucks, A. Maki, J. Mandin, S. Massie, J. Orphal, A. Perrin, C. Rinsland, M. Simth, J. Tennyson, R. Tolchenov, R. Toth, J. Auwera, P. Varanasi, and G. Wagner, "The HITRAN 2004 molecular spectroscopic database," *J. Quant. Spectrosc. Radiat. Transfer* 96, 139-204 (2005).
- [5] J. P. Besson, "Photoacoustic spectroscopy for multi-gas sensing using near infrared lasers," PhD Thesis, École Polytechnic Federale De Lausanne (2006).
- [6] W. Demtröder, *Laser spectroscopy*, Springer (2008).
- [7] J. J. Olivero and R. Longbothum, "Empirical fits to the Voigt line width: A brief review," *J. Quant. Spectrosc. Radiat. Transfer.* 17, 233-236 (1977).
- [8] F. Yang, "Novel hollow-core optical fiber gas and acoustic sensors," PhD Thesis, The Hong Kong Polytechnic University (2015).

-
- [9] A. Foltynowicz, “Fiber-laser-based noise-immune cavity-enhanced optical heterodyne molecular spectrometry,” PhD Thesis, Umeå University (2009).
- [10] J. Ye, L.-S. Ma, and J. L. Hall, “Ultrasensitive detections in atomic and molecular physics: demonstration in molecular overtone spectroscopy,” *J. Opt. Soc. Am. B* 15,6-15 (1998).
- [11] P. Kluczynski and O. Axner, “Theoretical description based on Fourier analysis of wavelength-modulation spectrometry in terms of analytical and background signals,” *Appl. Opt.* 38, 5803-5815 (1999).
- [12] P. Kluczynski, J. Gustafsson, Å. M. Lindberg, and O. Axner, “Wavelength modulation absorption spectrometry—an extensive scrutiny of the generation of signals,” *Spectrochimica Acta Part B: Atom. Spectro.* 56, 1277-1354 (2001).
- [13] S. Schilt, L. Thevenaz, and P. Robert, “Wavelength modulation spectroscopy: combined frequency and intensity laser modulation,” *Appl. Opt.* 42, 6728-6738 (2003).
- [14] R. Spearrin, C. Goldenstein, J. Jeffries, and R. Hanson, “Quantum cascade laser absorption sensor for carbon monoxide in high-pressure gases using wavelength modulation spectroscopy,” *Appl. Opt.* 53, 1938-1946 (2014).
- [15] G. Stewart, W. Johnstone, J. R. Bain, K. Ruxton, and K. Duffin, “Recovery of absolute gas absorption line shapes using tunable diode laser spectroscopy with wavelength modulation—Part I: Theoretical analysis,” *J. Lightwave Technol.* 29, 811-821 (2011).

Chapter 3

Acoustic detector based on optical fiber Fabry-Perot interferometer

3.1 Introduction

This chapter will present the acoustic sensors based on optical fiber Fabry-Perot (F-P) interferometer, which is formed between two parallel endfaces of the SMF and a multilayer graphene diaphragm. This acoustic detector is prepared for the photoacoustic gas sensors in Chapter 4. In this chapter, we first introduce construction of a low finesse F-P cavity. Secondly, the acoustic sensor based on multilayer graphene diaphragm is introduced, including the responses of graphene diaphragm under the static and dynamic pressure, and the signal demodulation scheme. Then the fabrication of the acoustic detector is presented. The sensitivity and frequency responses of the acoustic detector are measured and analyzed. Finally, a feedback control system for the operating point stabilization is designed and applied to the acoustic experiments.

3.2 The construction of a low finesse Fabry-Perot cavity

In terms of the cavity finesse, the F-P cavity can be divided into low finesse F-P cavity and high finesse F-P cavity. For the cavity with lower reflectivity ($r \ll 1$), it is regarded as the low finesse F-P cavity. For the cavity with higher reflectivity ($r \sim 1$), it can be regarded as the high finesse F-P cavity. In the following part, we mainly introduce acoustic detector which is a low finesse F-P cavity.

The construction a low finesse F-P cavity is shown in Figure 3.1. The space between the cleaved single mode fiber end and the diaphragm forms a F-P cavity and the

reflectivities of the fiber interface and the diaphragm are 4% approximately. The first reflected light intensity is 4% of the input light intensity, and the second reflected light intensity is 3.69% of the input light intensity. However, the third reflected light intensity is only 0.0059% of the input light intensity, which is 3 orders of magnitude smaller than the second reflected light. So the third and the other higher order reflection from the diaphragm can be neglected in a low finesse F-P cavity, which can be simplified as two-beam interference.

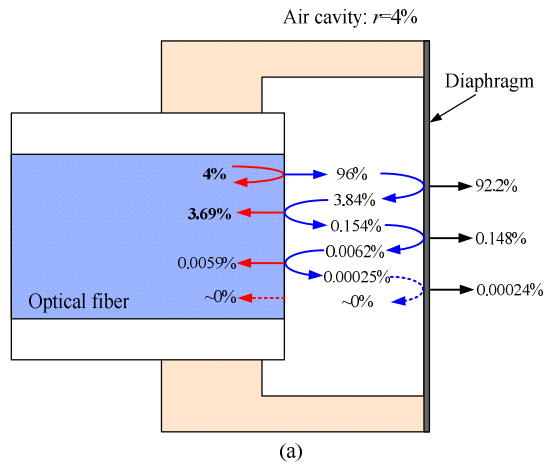


Fig. 3.1 Schematic of the acoustic detector based on multilayer graphene diaphragm.

The F-P cavity length L can be calculated from the cavity spectrum as [1]:

$$L = \frac{\lambda_1 \lambda_2}{2FSR} \quad (3.1)$$

where λ_1 , λ_2 are the wavelengths of the two adjacent resonant peaks of the cavity, and FSR is the free spectrum range of the cavity which is the separation of two adjacent wavelengths of the cavity transmission. When an external static/dynamic pressure is applied to the diaphragm of the F-P cavity, the diaphragm will be deformed, which will modulate the cavity length and induce an intensity variation of the reflected light from the F-P cavity. So diaphragm based low finesse F-P cavity can be used for acoustic/pressure detection as a pressure sensor. The size of this type of acoustic sensor is only in \sim mm

scale. The pressure response of the diaphragm plays an important role in the performance of the pressure/acoustic sensor. In the following part, the responses of graphene diaphragm to static and dynamic pressures will be discussed and analyzed based on the diaphragm vibration analysis.

3.3 Mechanical properties of graphene diaphragm

Since the F-P cavity is formed between the endface of the optical fiber and a thin graphene diaphragm, a simple model of a circular plate with its circular edges clamped can be used to approximate this cavity shown in Figure 3.2 [2]. The diaphragm will vibrate under the external pressure wave, and the pressure sensitivity of the diaphragm mainly depends on the properties of the diaphragm materials, such as radius a , thickness h , Young's modulus E and Poisson ratio μ of the diaphragm. So in this section, the pressure response of the diaphragm will be discussed and analyzed from two aspects, including the responses of static and dynamic pressure.

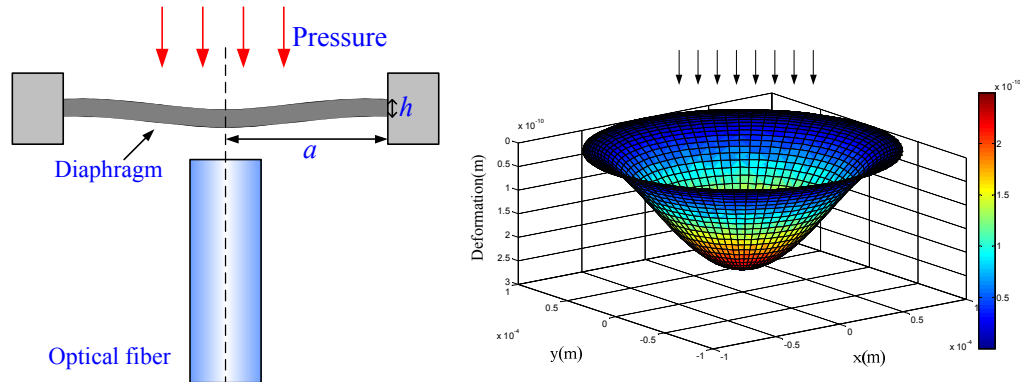


Fig. 3.2 Schematic of a diaphragm based F-P cavity under an external pressure.

Two different models can be adopted to analyze the mechanical behavior of the circular thin diaphragm [3]:

- (1) Linear plate theory: thick membrane with small deformations which is smaller than 20%~30% of the diaphragm thickness, such as silica and polymer diaphragm with

thickness at the level of micrometer scale;

- (2) Nonlinear membrane theory: thin membrane with deformations which is higher than 20%~30% of the diaphragm thickness, such as graphene diaphragm with thickness at the level of nanometer scale.

Here the nonlinear membrane theory will be used to analyse the deflection of the graphene diaphragm.

3.3.1. Deflections under static pressure

When the center deformation of the graphene diaphragm is large compared with its thickness of the diaphragm, the relationship between the applied static pressure p and the center deformation Y_{deform} can be expressed by [3-5]

$$p = \frac{E}{1-\mu} \frac{2hY_{deform}^3}{r^4} + \sigma_0 \frac{4hY_{deform}}{r^2} \quad (3.2)$$

where h and r are the thickness and radius of the diaphragm, E and μ are the Young's modulus and Poisson ratio of the diaphragm, σ_0 is the initial stress or pre-stress on the diaphragm before the pressure is applied. From Eq. (3.2), we can see that the applied static pressure p is formed by two terms of nonlinear term $\frac{2hE}{(1-\mu)r^4} Y_{deform}^3$ and linear term $\frac{4h\sigma_0}{r^2} Y_{deform}$. When the applied static pressure p is large, the nonlinear term of the large deformation will dominate, while the linear term of the small deformation will dominate when the applied pressure p is small.

Figure 3.3 shows the calculated deformation of the diaphragm in terms of the applied pressure with different parameters of thickness h , radius r and pre-stress σ_0 . The values of E and μ used in the calculation are 1 TPa and 0.17. Figure 3.3 (a) shows

diaphragm deformation with different values of thickness h , indicating that the diaphragm with higher thickness has lower pressure sensitivity. Figure 3.3 (b) shows diaphragm deformation with different values of radius r , indicating that the diaphragm with larger radius has higher pressure sensitivity. Figure 3.3 (c) shows diaphragm deformation with different values of pre-stress σ_0 , indicating that the diaphragm with larger pre-stress has lower pressure sensitivity. So thinner diaphragm with larger radius is required for the design of pressure sensors with higher sensitivity.

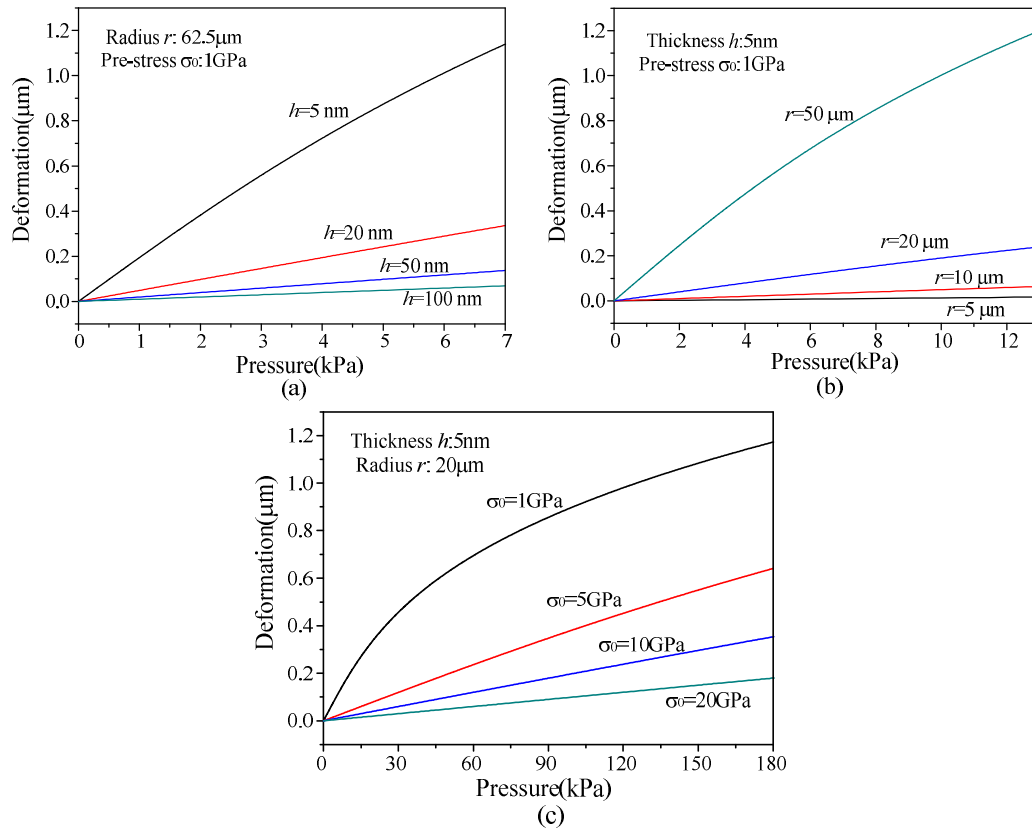


Fig. 3.3 The calculated deformation of the diaphragm with different parameters of (a) thickness h , (b) radius r and (c) pre-stress σ_0 .

3.3.2. Deflections under dynamic pressure

Under the condition of dynamic pressure, the resonant frequency f_{mn} for a circular diaphragm with radius of r and thickness of h can be expressed as [6]

$$f_{mn} \approx p^{1/3} \frac{a_{mn}}{2\pi r} \left(\frac{Er^2}{32(1-\mu)h^2\rho^3} \right)^{1/6} \quad (3.3)$$

where E , ρ and μ are the Young's modulus, mass density and Poisson ratio of the diaphragm. a_{mn} is a constant for different order (m, n) of the vibration modes, and its values are listed in Table 3.1 [3]. The subscript m and n denote the number of the nodal diameter and nodal circle, respectively.

Table 3.1 Values of a_{mn}

	$n=1$	$n=2$	$n=3$	$n=4$
$m=0$	2.404	5.520	8.654	11.792
$m=1$	3.832	7.016	10.173	13.323
$m=2$	5.135	8.417	11.620	14.796
$m=3$	6.379	9.760	13.017	16.224

Figure 3.4 shows the calculated resonant frequency of the diaphragm as functions of the pressure with different radius r . The values of E , ρ and μ used in the calculation are 1 Tpa, 2200kg/m³ and 0.17 [7]. Table 3.2 shows the calculated resonant frequencies of the diaphragm for different order (m, n) of the vibration modes.

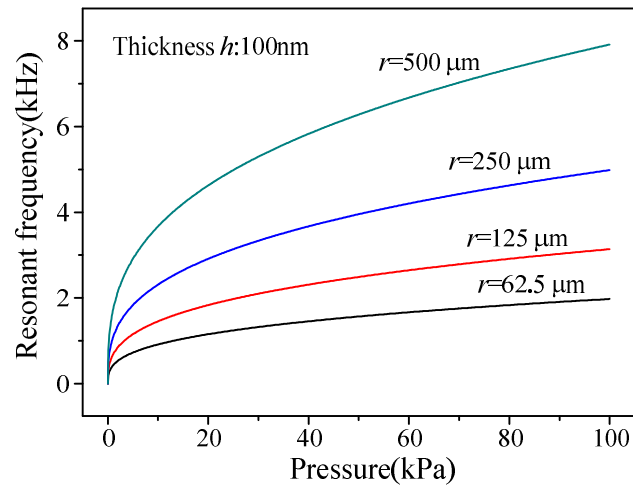


Fig. 3.4 Resonant frequency as functions of the pressure for membranes with different radius r .

Table 3.2 Resonant frequency (kHz) for different vibration modes

	$n=1$	$n=2$	$n=3$	$n=4$
$m=0$	7.901	18.165	28.479	38.805
$m=1$	12.610	23.088	33.477	43.843
$m=2$	16.898	27.699	38.239	48.691
$m=3$	20.992	32.118	42.836	53.390

3.4 Signal demodulation

For the acoustic sensor, the acoustic wave is applied to the diaphragm and the periodic deformation of the diaphragm modulates the cavity length, then the interference spectrum will shift, changing the reflected light intensity in the output of the F-P cavity, as shown in Figure 3.5.

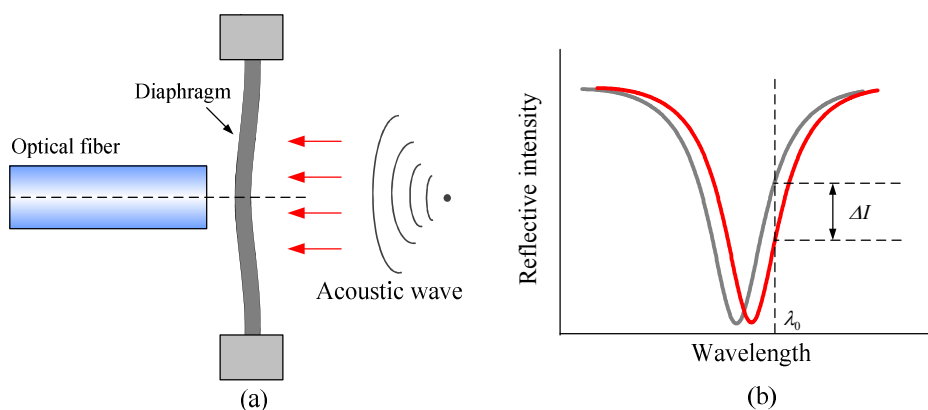


Fig. 3.5 (a) Schematic of diaphragm based F-P cavity under acoustic wave. (b) Modulated reflected power spectrum.

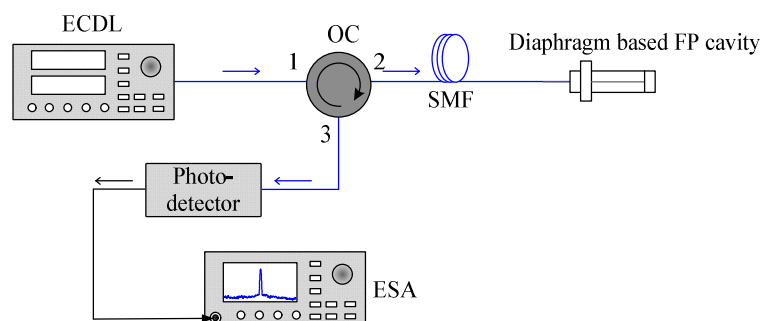


Fig. 3.6 Schematic of the demodulation system for diaphragm based F-P cavity.

In order to analyze the deformation of the diaphragm quantitatively and achieve a linear response to maximize the sensitivity of the F-P cavity (S_{FP}), a linear/quadrature demodulation technique can be used to demodulate the signal from the cavity [8]. Figure 3.6 shows the demodulation system for diaphragm based F-P cavity. An external cavity diode laser (ECDL) is used as the light source and is injected to the F-P cavity via port 1 and 2 of an optical circulator (OC). The reflected light is directed to a photo-detector (PD) via port 3 of the OC, and the output of PD is received and analyzed by a real-time electrical spectrum analyzer (ESA).

The maximum sensitivity of an F-P cavity (S_{FP}) in terms of the cavity length change can be obtained by operating the laser wavelength at the quadrature point (Q -point)

where the slope of the interference fringes is steepest [9, 10]. As shown in Figure 3.7, taking a low-finesse F-P cavity with a sinusoidal interference as an example, when the laser wavelength is chosen at the Q -point, the cavity shows a linear response and the output sensitivity becomes maximum (red line). However, if the laser wavelength works at the peak or dip of the interference fringe, the output signal would become distorted and the sensitivity would deteriorate (purple line).

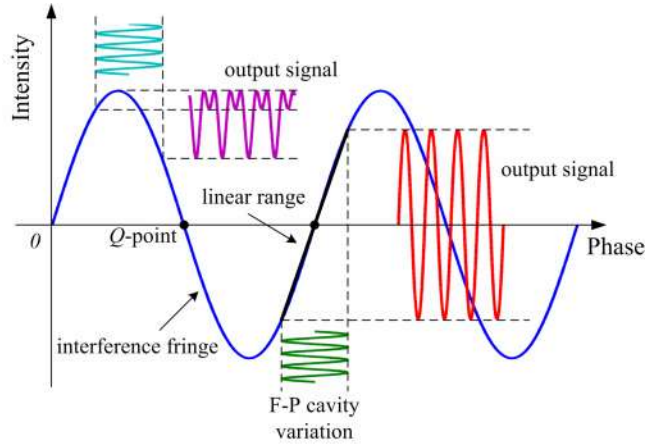


Fig. 3.7 Illustration of a linear operating range of the signal demodulation [9, 10].

To be more specific, the sensitivity of an F-P cavity (S_{FP}) in terms of the cavity length change can be expressed as

$$S_{FP} = abs\left(\frac{dI_r}{dL}\right) \quad (3.4)$$

I_r is the reflected light intensity from the F-P cavity and it can be expressed as [11]

$$I_r = I_0 \frac{r_1 + r_2 - 2\sqrt{r_1 r_2} \cos(4\pi nL / \lambda + \varphi_0)}{1 + r_1 r_2 - 2\sqrt{r_1 r_2} \cos(4\pi nL / \lambda + \varphi_0)} \quad (3.5)$$

where I_0 is the input light intensity of the cavity, r_1 , r_2 are the reflectivities of the two endfaces of the cavity, n is the refractive index within the cavity, L is the cavity length, λ is the wavelength of the input light, and φ_0 is the constant phase shift. Then Eq. (3.4) can be calculated as

$$S_{FP} = abs\left(\frac{dI_r}{dL}\right) = abs\left(\frac{d\left(I_0 \frac{r_1 + r_2 - 2\sqrt{r_1 r_2} \cos(4\pi nL / \lambda + \varphi_0)}{1 + r_1 r_2 - 2\sqrt{r_1 r_2} \cos(4\pi nL / \lambda + \varphi_0)}\right)}{dL}\right) \quad (3.6)$$

Assuming that $r_1=r_2=r$, $n=1$ for air, $\varphi_0=0$, Eq. (3.6) can be calculated as

$$S_{FP} = abs\left(I_0 \frac{2r(1-r)^2 \frac{4\pi}{\lambda} \sin\left(\frac{4\pi L}{\lambda}\right)}{\left[1 + r^2 - 2r \cos\left(\frac{4\pi L}{\lambda}\right)\right]^2}\right) \quad (3.7)$$

The interference spectrums of the F-P cavity under different reflectivities of 4%, 10%, 30% and 50% are shown in Figure 3.8 (a). The correspondingly sensitivity S_{FP} for different reflectivities are also shown in Figure 3.8 (b). From Figure 3.8 (b), the sensitivity S_{FP} increases with the reflectivity and drifts to the peak or dip of the interference fringes. Therefore, the laser wavelength should operate at Q -point to obtain both the high sensitivity and linear response.

Moreover, the sensitivity of the F-P cavity to the external pressure wave is also related to the pressure sensitivity of the diaphragm ($S_d=\Delta L/\Delta P$), responsibility of PD (R) and the gain of the amplifier (G). So the output current i_{ac} of a low-finesse F-P cavity for an laser source with the light intensity of I_0 can be expressed as [3]

$$i_{ac} = R \cdot G \cdot I_0 \cdot S_{FP} \cdot \Delta L = R \cdot G \cdot I_0 \cdot S_{FP} \cdot S_d \cdot \Delta P \quad (3.8)$$

where $S_d=\Delta L/\Delta P$ is the pressure sensitivity of the diaphragm, and ΔL is the diaphragm deflection induced by the dynamic pressure ΔP . From Eq. (3.8), the sensitivity to the external pressure ($i_{ac}/\Delta P$) of the cavity is determined by S_{FP} , S_d , R of the PD and G of the amplifier.

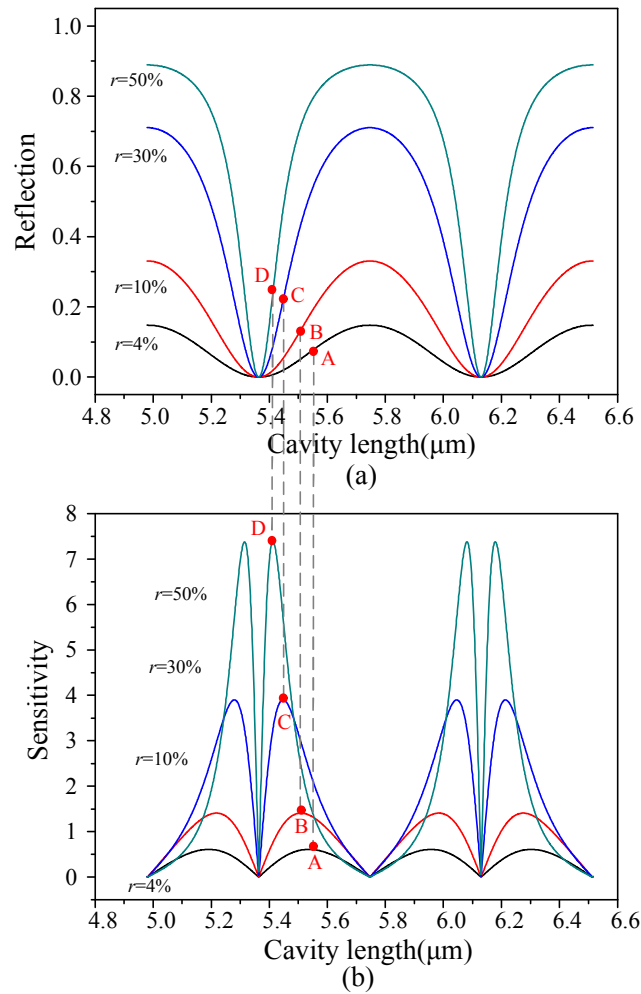


Fig. 3.8 (a) Interference fringes for different reflectance, and (b) corresponding sensitivity curves for each fringe.

3.5 Acoustic detector with multilayer graphene diaphragm

Graphene can be regarded as one of the most sensitive materials for pressure/acoustic sensors due to its excellent characteristics of ultra-thin thickness, extraordinary stiffness and large elastic deformation range [12]. In the near few years, our research group has investigated a lot in the aspect of compact optical fiber acoustic/pressure sensors with few and multilayer graphene as the sensitive diaphragms [7, 13, 14]. Table 3.3 summarizes the characteristic parameters of the graphene diaphragms used in our fiber F-P cavity.

Table 3.3 Characteristic parameters of the graphene diaphragms

<i>Graphene</i>	Few-layer	Multilayer		
<i>Type</i>	fiber-tip	ferrule-top	ferrule-top	sleeve-top
<i>Thickness</i>	<1 nm	10~15 nm	100 nm	100 nm
<i>Diameter</i>	25 μm	125 μm	125 μm	2.5 mm

The acoustic detectors are based on the multilayer graphene diaphragm located at the ends of optical fibers, as shown in Figure 3.9. An optical F-P interferometer (FPI) is formed between the cleaved end of the SMF and the surface of the graphene diaphragm. Acoustic wave applied to the graphene diaphragm drives it back and forth periodically, the periodic deformation modulates the cavity length of the FPI. When a probe light beam is propagating into the FPI, the reflected light intensity will vary periodically, which is detected to recover the acoustic pressure information. In this section, two types of acoustic detectors made with 100 nm-thick multilayer graphene diaphragm with different diameter of 2.5 mm and 125 μm are introduced, as shown in Figure 3.9.

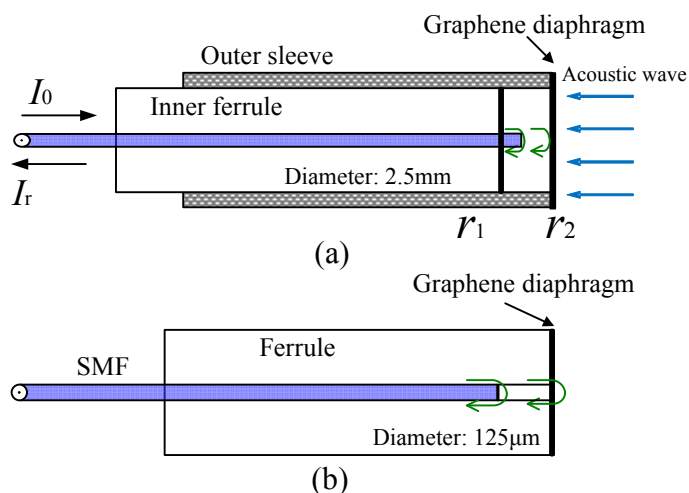


Fig. 3.9 Schematic diagram of the fiber FPI acoustic detector. (a) a graphene diaphragm with diameter of 2.5 mm covering the endface of a sleeve; (b) a graphene diaphragm with diameter of 125 μm covering the endface of a zirconia ferrule.

3.5.1 Fabrication of the acoustic detector

3.5.1.1 The acoustic detector with 125 μm -diameter graphene diaphragm

From Figure 3.9 (b), the 125 μm -diaphragm acoustic detector consists of a cleaved single mode fiber (SMF), a ceramic ferrule with inner/outer diameter of 125 μm /1 mm, and a \sim 100-nm-thick multilayer graphene diaphragm. The graphene diaphragm is obtained from a multilayer graphene/Nickel(Ni)/ multilayer graphene (MLG/Ni/MLG film) sample in which the graphene diaphragm is grown on both sides of the Ni foil with thickness of 25 μm by chemical vapor deposition (CVD) (Graphene-supermarket.com). As shown in Figure 3.10, the fabrication of the sensor head is followed by four main steps [13]:

- (1) To separate the MLG/Ni/MLG film from the Ni foil substrate, the MLG/Ni/MLG film was cut into 2.5 mm \times 2.5mm square piece and immersed into a Ferric chloride (FeCl_3) solution with a concentration of 0.05 g/mL to separate from the Ni foil [Fig. 3.10 (a)].
- (2) After staying in the FeCl_3 solution for \sim 8 hours, both sides of the MLG/Ni/MLG film was detached from the Ni foil, then the multilayer graphene diaphragm sample was transferred to de-ionized (DI) water by a glass slide [Fig. 3.10 (b)]. The MLG is thick enough to avoid being damaged during the transferring process compared with the single larger and few layer graphene diaphragm.
- (3) To transfer the MLG film onto the surface of the ceramic ferrule, the MLG film was transferred into the clean DI water and float on the water surface for \sim 4 hours to remove the residual Fe ions. The ferrule was then moved down slowly toward the

floating MLG film until the graphene sample is attached to the endface of the ferrule together with a thin layer of water. The ferrule with the MLG film was then dried at room temperature for ~0.5 hour to remove the residual water [Fig. 3.10 (c).] After water evaporation, the MLG film is firmly stuck to the surface of the ferrule by the van der Waals interaction [15].

- (4) Finally, a cleaved SMF is inserted into the ferrule covered with the MLG film and moved slowly to the MLG film by a precision translation stage, as shown in Fig. 3.10 (d). The reflective surfaces between the cleaved fiber end and the graphene diaphragm form a low-finesse F-P cavity, and the reflection spectrum is monitored and used to determine the cavity length of the F-P cavity. Once the expected cavity length is achieved, the SMF is fixed to the ferrule with epoxy. A photograph of the assembled acoustic detector is shown in Fig. 3.10 (d).

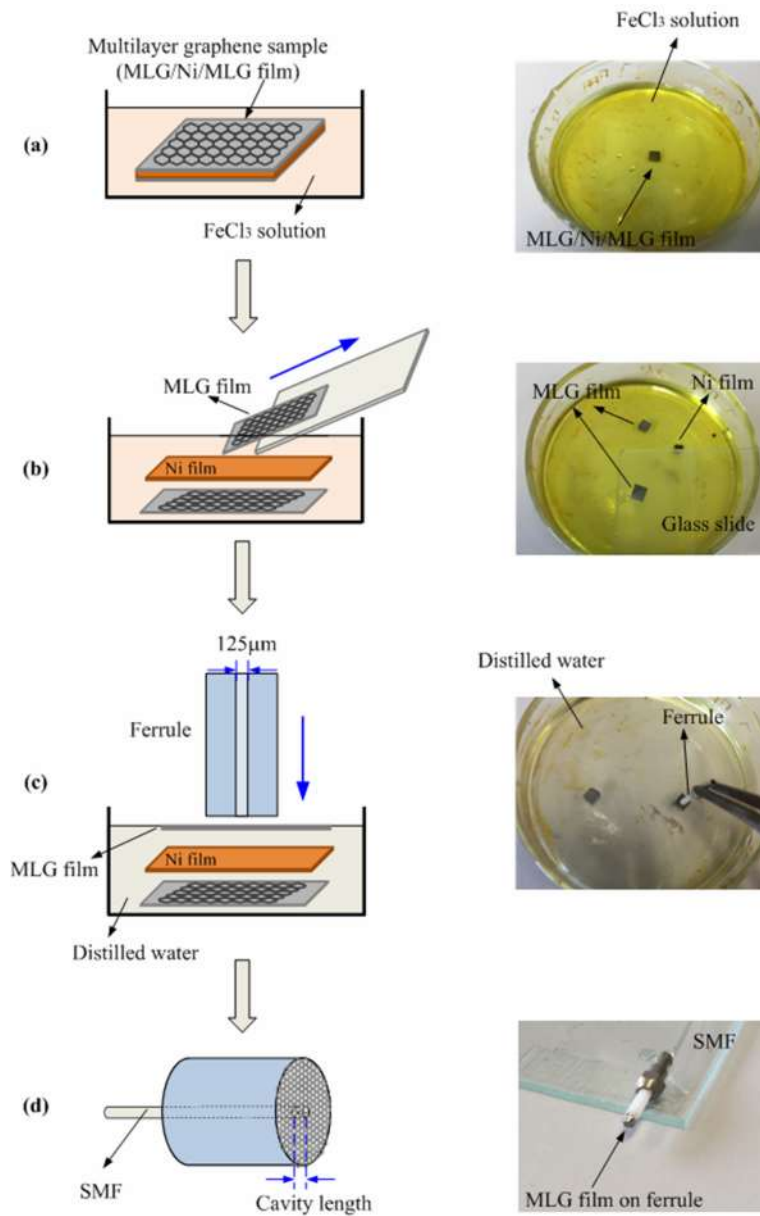


Fig. 3.10 Fabrication process of the 100 nm-thick, 125- μm -diameter MLG diaphragm-based FPI acoustic detector.

3.5.1.2 The acoustic detector with 2.5 mm-diameter graphene diaphragm

From Figure 3.9 (a), the 2.5 mm-diameter acoustic detector consists of a cleaved single mode fiber, a ceramic ferrule with inner/outer diameter of 125 μm /2.5 mm, a hollow

ceramic sleeve with inner diameter of 2.5 mm, and a ~100-nm-thick multilayer graphene diaphragm. As shown in Figure 3.11, the fabrication of the sensor head is followed by four main steps:

- (1) The MLG/Ni/MLG film was firstly cut into 2.5 mm×2.5mm square piece and was flattened between two glass slides. One end of the hollow ceramic sleeve is coated with a thin layer of ultraviolet (UV) curable liquid gel. The top glass slide is then removed and the gel-coated sleeve end is compressed onto the flat surface of the flattened sample film [Figures 3.11 (a), (b)].
- (2) After that, the liquid gel between the sleeve and sample film is cured under the UV light illumination for ~6 hours and the MLG/Ni/MLG film is then firmly stuck to the sleeve end. By immersing the film-stuck sleeve into a FeCl₃ solution to separate MLG film from the Ni foil [Figures 3.11 (c), (d), (f)].
- (3) The sleeve end is flushed in the DI water to separate the lower MLG film from the sleeve-attached MLG film. The sleeve with MLG film was then dried at room temperature for ~0.5 hour to remove the residual water.
- (4) Finally, a cleaved SMF is inserted and fixed into the ferrule by epoxy, and then this assembly is inserted into the prepared sleeve in Step (3) and moved slowly toward the MLG film by use of a precision translation stage. The reflective surfaces between the cleaved fiber end and the graphene diaphragm form a low-finesse FPI, and the reflection spectrum is monitored and used to determine the cavity length of the FPI. Once the expected cavity length is achieved, the sleeve is fixed to the ferrule with epoxy. A photograph of the assembled acoustic detector is shown in Figure 3.11 (g).

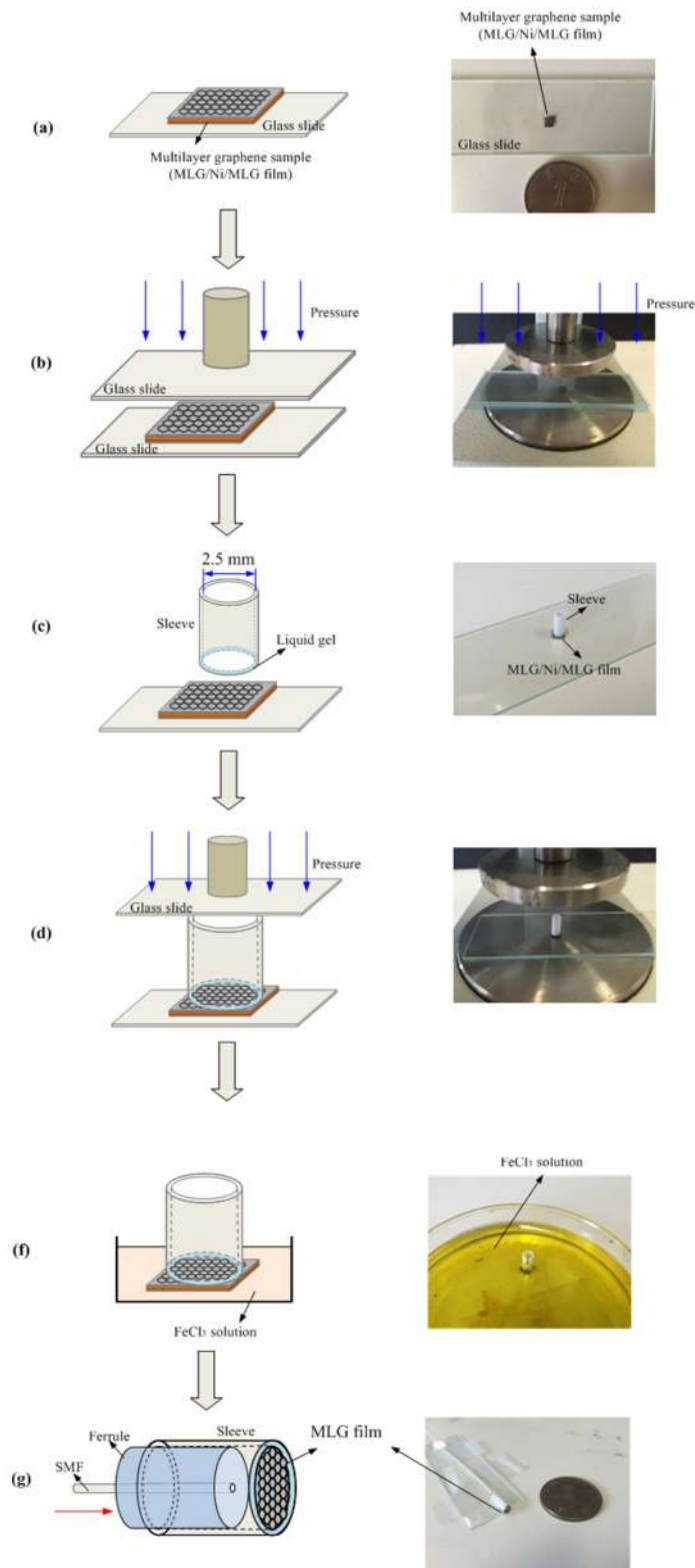


Fig. 3.11 Fabrication process of the 100 nm-thick, 2.5-mm-diameter MLG diaphragm-based FPI acoustic detector.

Figure 3.12 shows the experimental setup for the measurement of reflection spectrum of the fabricated acoustic detector. A broadband light source (BBS) is propagating into the fabricated F-P acoustic detector, via the port 1 and 2 of a optical circulator (OC) and the reflected light from the acoustic detector is received by an optical spectrum analyzer (OSA) via port 3 of the OC. Figure 3.13 shows the measured reflection spectrum (red solid line) and the calculated spectrum (black dash line) of the 2.5 mm-diameter acoustic detector. The visibility of the measured interference fringe is ~ 20 dB with a free spectrum range of ~ 17.6 nm around 1540 nm. The corresponding cavity length referred to the separation between the fiber end and graphene diaphragm is then calculated to be $68.3 \mu\text{m}$ by Eq. (3.1) [16].

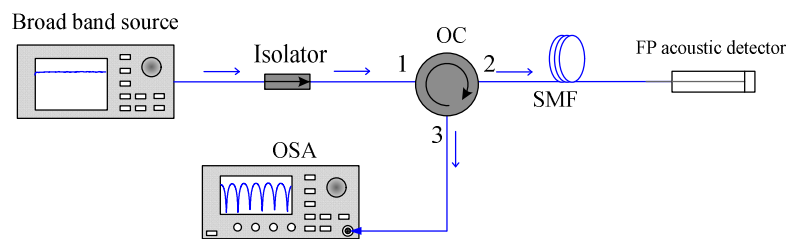


Fig. 3.12 Experimental setup for reflection spectrum measurement of the fabricated acoustic detector.

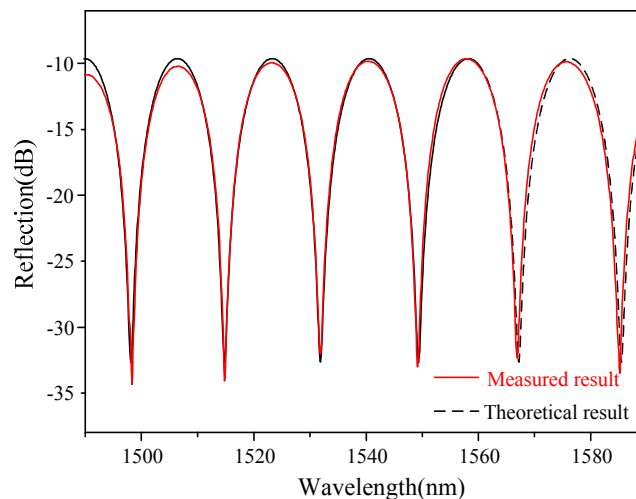


Fig. 3.13 Measured reflection spectrum of the graphene diaphragm-based F-P cavity.

3.5.2 Sensitivity and frequency response to acoustic pressure

The performances of graphene diaphragm-based FPI as acoustic detectors can be characterized by several parameters including the linearity (Q -point), signal to noise ratio (SNR), minimum detectable pressure (MDP), and Q -point stability. The definition of these parameters are shown in the following part as:

(1) **Linearity (Q -point)**: The maximum sensitivity of a F-P cavity (S_{FP}) in terms of the cavity length change can be obtained by operating the laser wavelength at the quadrature point (Q -point) where the slope of the interference fringes is steepest [10], as shown in Figure 3.14 and introduced in Section 3.4. Figure 3.14 is the linear scale of the measured reflection spectrum of the FPI in Figure 3.13.

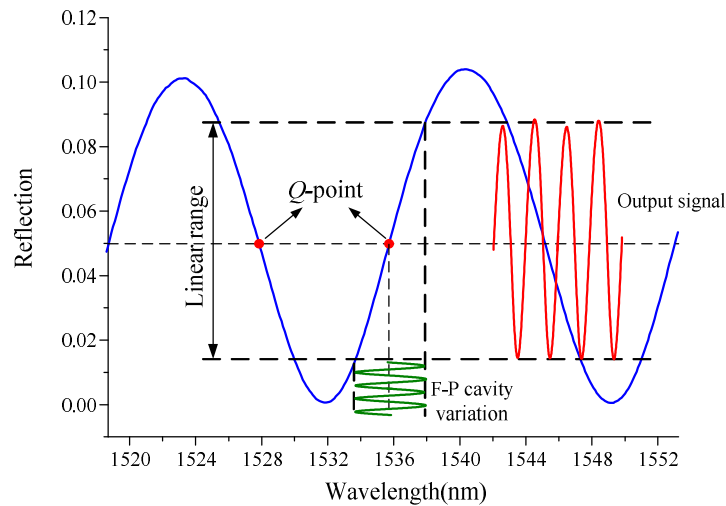


Fig. 3.14 Schematic of a linear operating range of the sensor response curve. linear scale of the measured reflection spectrum of the FPI in Fig. 3.13.

(2) **Q -point stability**: As mentioned in Section 3.4, to achieve a linear response and maximize the sensitivity, the wavelength of the probe laser for acoustic detection should be tuned to the Q -point of the interference spectrum. However, it was found that the operating point often drift due to environmental perturbation such as background pressure change, which leads to long term instability of the demodulation system.

Therefore, an active feedback control system will be introduced to maintain the wavelength operating at the Q -point in this section [16].

(3) **Signal to noise ratio (SNR)**: SNR is the ratio of signal to noise level, which can be expressed in linear scale of V_{signal}/V_{noise} by

$$SNR = V_{signal} / V_{noise} = 10^{dB_{scale}/20} \quad (3.9)$$

where V_{signal} and V_{noise} are the signal and noise voltage respectively, and dB scale is usually displayed on the detector, such as a real-time electrical spectrum analyzer (ESA). If the measured SNR of the system is higher, the sensitivity of the acoustic detector would be improved, indicating better performance of the detector.

(4) **Minimum detectable pressure (MDP)**: MDP is used to describe the incident acoustic pressure that induces an output signal equal to the noise, i.e. the noise-limited minimum detectable pressure level of the acoustic detector. It can be expressed by

$$MDP = \frac{P}{SNR \cdot \sqrt{BW}} \quad \text{in } \mu\text{Pa}/\text{Hz}^{1/2} \quad (3.10)$$

where p is the actual pressure and BW is the detection bandwidth of the detector.

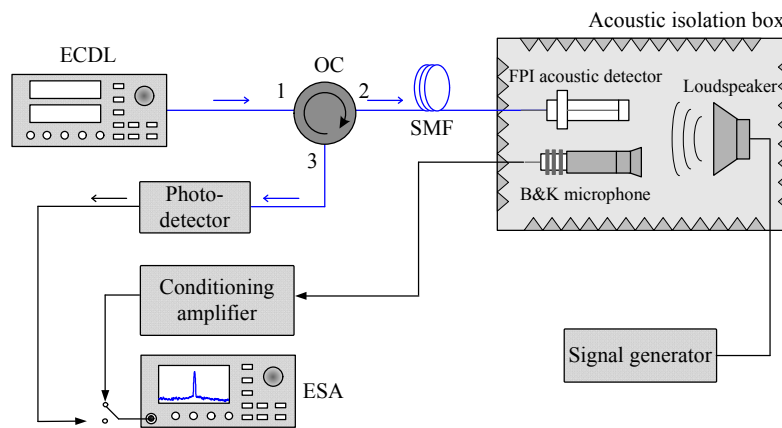


Fig.3.15 Experimental setup for testing the performance of the optical fiber acoustic detector.

The performances of graphene diaphragm-based FPI as acoustic detector are tested

with the experimental setup shown in Figure 3.15. The measurement can be conducted by the following steps:

(1) Devices preparation for acoustic measurement

External cavity diode laser (ECDL): tunable laser source (Agilent, 81600B);

Photo-detector: convert the optical signal into electrical signal;

Loudspeaker combined with the signal generator: generate the acoustic pressure under different frequencies;

B&K electrical microphone (B&K 4189) combined with its conditioning amplifier: determine the actual acoustic pressure applied to the FPI as a reference microphone;

Real-time electrical spectrum analyzer (ESA): display the detected acoustic signal from photo-detector or conditioning amplifier. (Tektronix, 3303A)

(2) The optical fiber acoustic detector under test was placed ~15 cm from a loudspeaker which is used as the acoustic source. A calibrated reference microphone was positioned at the symmetry point of the fiber acoustic detector to the central axis of the speaker, and the measured acoustic pressure with the reference microphone is regarded as the same as that incident on the fiber acoustic detector. The optical acoustic detector, the reference microphone and the speaker are all put inside an acoustically isolated chamber.

(3) Actual pressure measurement (pressure calibration):

The amplitude and frequency of the loudspeaker are set at specific value, say 5V and 2kHz, and the sensitivity of the B&K electrical microphone is set as 10 mv/Pa. Then the ESA (Tektronix, 3303A) is connected to the conditioning amplifier to measure the actual pressure generated by the loudspeaker speaker.

(4) Pressure response measurement of the optical fiber acoustic detector:

After calibrating the actual acoustic pressure, the ESA (Tektronix, 3303A) is connected to the photo-detector (PD). Then the light from an ECDL (Agilent, 81600B) (the probe) is injected to the FPI acoustic detector via port 1 and 2 of an optical circulator (OC). The working wavelength of the probe laser is tuned to the Q -point of the interference spectrum to achieve a linear response and to maximize the sensitivity to acoustic pressure. The reflected probe light is directed to a PD via port 3 of the OC. Then the pressure sensitivity can be calculated from ESA according to the reference pressure measured by B&K electrical microphone.

(5) The frequency of the signal generator is tuned from 1 kHz to 20 kHz with step of 1 kHz, and Step 3 and 4 are repeated. Then the frequency response of the optical fiber acoustic detector can be obtained.

3.5.2.1 The acoustic detector with 125 μm -diameter graphene diaphragm

The frequency response of the 125 μm -diameter optical fiber acoustic detector is measured by tuning the frequency from 1 kHz to 20 kHz of the loudspeaker and the output signal is measured by the ESA. The sensitivity of the B&K electrical microphone is set as 10 mV/Pa. According to the voltage signal $V_{B\&K}$, then the actual acoustic pressure p at different frequencies can be determined by

$$p = \frac{V_{B\&K}}{\text{Sensitivity}_{B\&K}} \quad (3.11)$$

Figure 3.16 shows the frequency response of the 125- μm -diamater FPI from 3 to 17 kHz. The acoustic pressure sensitivity reaches a maximum value of 2 mV/Pa at ~ 4 kHz, corresponding to one of the resonances of the graphene diaphragm. To be more specific,

the power spectrums of PD output measured by ESA when acoustic pressure levels of 35.0 mPa at 3.8 kHz and 49.5 mPa at 7.4 kHz are applied are shown in Figure 3.17. Table 3.4 shows the measured MDP value of the fiber FPI with 125- μm -diameter graphene diaphragm. The noise floor is about ~ 90 dBm for a 50 Hz resolution bandwidth. The signal to noise ratios (SNRs) are respectively 37.5 dB and 32 dB for the two cases, corresponding to a noise-limited minimum detectable pressure (MDP) level of $66.0 \mu\text{Pa}/\text{Hz}^{1/2}$ at 3.8 kHz and $175.8 \mu\text{Pa}/\text{Hz}^{1/2}$ at 7.4 kHz.

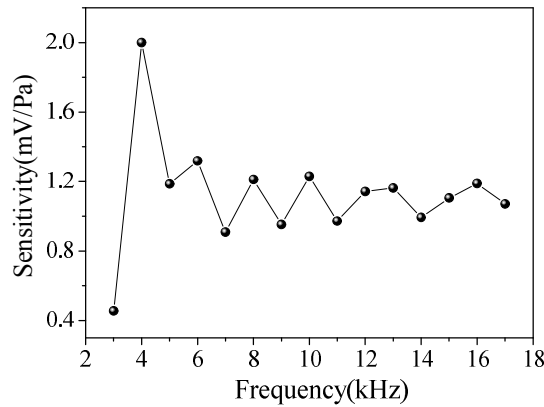


Fig. 3.16 Frequency response of the fiber FPI with 125- μm -diameter graphene diaphragm.

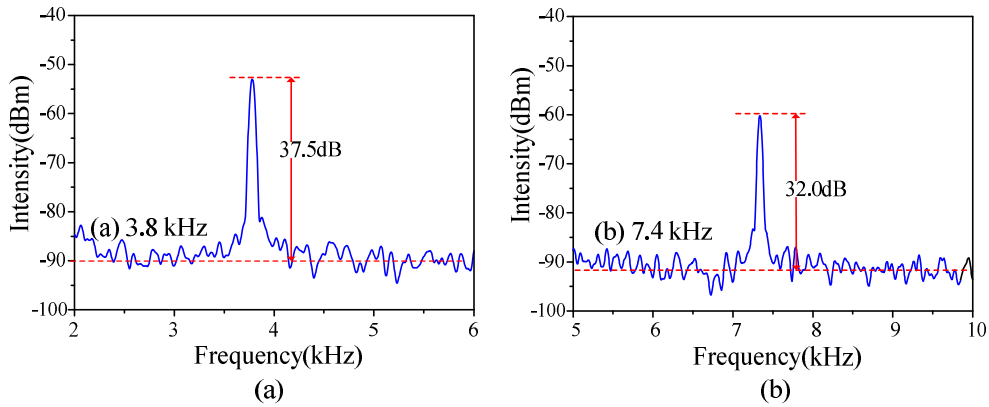


Fig. 3.17 Power spectrum of the photo-detector output when an acoustic pressure level of (a) 35 mPa at 3.8 kHz and (b) 49.5 mPa at 7.4 kHz is applied.

Table 3.4 MDP value of the 125 μm -diameter optical fiber acoustic detector at Q -point

Acoustic Frequency (kHz)	Acoustic pressure (mPa)	SNR (dB)	MDP($\mu\text{Pa}/\text{Hz}^{1/2}$)
3.8 kHz	35.0	37.5	66.0
7.4 kHz	49.5	32.0	175.8

3.5.2.2 The acoustic detector with 2.5mm-diameter graphene diaphragm

Similar with the measurement of the 125 μm -diameter optical fiber acoustic detector, the frequency response of the 2.5mm-diameter optical fiber acoustic detector also is measured by tuning the frequency from 1kHz to 20kHz of the loudspeaker and the output signal is measured by the ESA. The sensitivity of the B&K electrical microphone is set as 100 mV/Pa.

Figure 3.18 shows the frequency response of the 2.5-mm-diameter FPI from 2 to 17 kHz. The acoustic pressure sensitivity reaches the maximum value of 80 mV/Pa when operating the graphene diaphragm at resonance (~ 10.1 kHz). The power spectrum of the photo-detector output for the applied acoustic pressure of 10.55 mPa at 10.1 kHz and 12.05 mPa at 16.0 kHz are shown in Figure 3.19 (a) and Figure 3.19 (b), respectively. Table 3.5 shows the measured MDP value of the fiber FPI with 2.5-mm-diameter graphene diaphragm. The noise floor is about ~ 90 dBm for a 50 Hz resolution bandwidth. The SNRs for the two cases are 57.0 dB and 45.5 dB, corresponding respectively to a noise-limited MDP level of $2.11 \mu\text{Pa}/\text{Hz}^{1/2}$ at 10.1 kHz and $9.05 \mu\text{Pa}/\text{Hz}^{1/2}$ at 16.0 kHz. The value at 10.1 kHz is better than the commercial B&K4189 microphone ($\sim 8 \mu\text{Pa}/\text{Hz}^{1/2}$), and the MDP at resonance is ~ 4 times better than

off resonance. Moreover, the MDP level of the 2.5-mm-diaphragm acoustic detector is 31 times better than that of the 125- μm -diameter one, showing straightforward sensitivity improvement for graphene diaphragm with a larger diameter, which is in agreement with the model in Ref. [7].

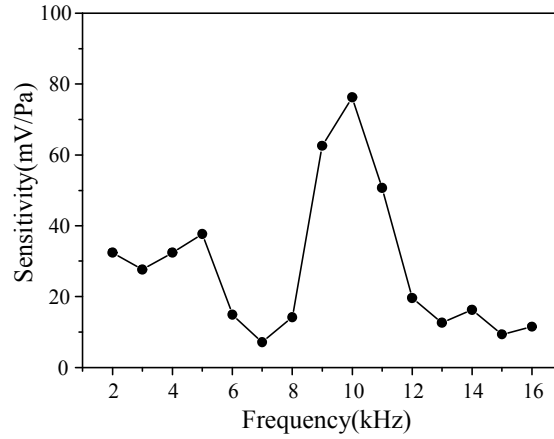


Fig. 3.18 Frequency response of the FPI with 2.5-mm-diameter graphene diaphragm.

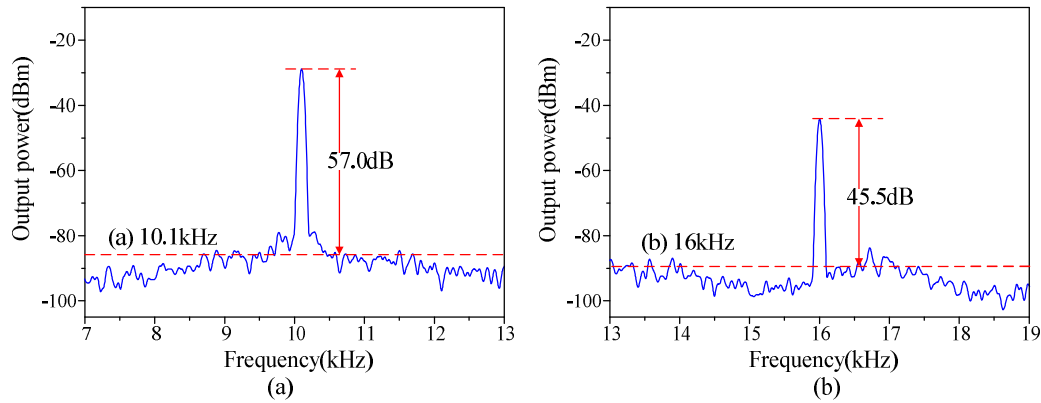


Fig. 3.19 Power spectrum of the photo-detector output when an acoustic pressure level of (a) 10.55 mPa at 10.1 kHz and (b) 12.05 mPa at 16.0 kHz is applied.

Table 3.5 MDP value of the 2.5 mm-diameter optical fiber acoustic detector at Q -point

Acoustic Frequency (kHz)	Acoustic pressure (mPa)	SNR (dB)	MDP($\mu\text{Pa}/\text{Hz}^{1/2}$)
10.1 kHz	10.55	57.0	2.11
16.0 kHz	12.05	45.5	9.05

3.5.3 Mechanical thermal noise limited equivalent pressure level

We will analyze and calculate the noise equivalent pressure level of the uniform diaphragm in the acoustic detectors regarding the mechanical thermal noise, which is associated with the random motion of the diaphragm due to dissipation mechanisms in the sensor. This mechanical thermal noise sets a detection limit of any acoustic detector for measuring the acoustic wave.

The mechanical thermal noise of the acoustic sensor is the root-mean square of the fluctuating pressure and it can be expressed by [17]

$$P_N = \sqrt{4k_B T R_{acs}} \quad \text{in } \mu\text{Pa/Hz}^{1/2} \quad (3.12)$$

where k_B is the Boltzmann constant $k_B = 1.38 \times 10^{-23} \text{ J/K}$ and T is the environmental temperature. And $R_{acs} = R/S^2$ is the total acoustic resistance with total mechanical resistance R and area of the diaphragm S . Total mechanical resistance R consists of viscous resistance (R_{vsc}) and radiation resistance (R_{rad}) with $R = R_{vsc} + R_{rad}$.

The viscous resistance R_{vsc} originates from the Brownian motion. When the diaphragm vibrates within a fluid, its motion will be damped and it will suffer from a power dissipation. This damping effect shows that the intensity of any diaphragm vibration will attenuate gradually since the diaphragm has random collisions with the surrounding molecules no matter it is vibrational or stationary, which is described as squeeze-film damping. The viscous resistance R_{vsc} regarding to the squeeze-film damping is [17]

$$R_{vsc} = \frac{3\mu S^2}{2\pi L^3} \quad (3.13)$$

where μ is the dynamic viscosity of air $\mu = 1.82 \times 10^{-5} \text{ Pa} \cdot \text{s}$ at $T = 20^\circ\text{C} = 293\text{K}$, L is length gap between diaphragm and fiber end (cavity length).

The energy of a vibrating diaphragm will attenuate gradually with the production of the pressure waves, and this corresponds to the radiation resistance R_{rad} which is [17]

$$R_{rad} = \frac{\rho_{air} \omega^2 S^2}{4\pi c} \quad (3.14)$$

where ρ_{air} is the density of dry air, 1.21 kg/m^3 , r is radius of the diaphragm, $\omega = 2\pi f$ is the operation frequency and c is speed of sound in air, 343 m/s . Then the total acoustic resistance R_{acs} becomes

$$R_{acs} = \frac{R}{S^2} = \frac{R_{vsc} + R_{rad}}{S^2} = \frac{3\mu}{2\pi L^3} + \frac{\rho_{air} \omega^2}{4\pi c} \quad (3.15)$$

Figure 3.20 shows the calculated mechanical thermal noise P_N for different operation frequency of the diaphragm by the Eqs. (3.12-3.15) we can see that the mechanical thermal noise P_N increases with the operation frequency. Table 3.6 shows the comparison of measured MDP and calculated mechanical thermal noise of the graphene diaphragm based acoustic detector. The measured MDP is still higher than the calculated mechanical thermal noise and we are still trying to achieve this minimum limit by increasing the sensitivity of the acoustic detector.

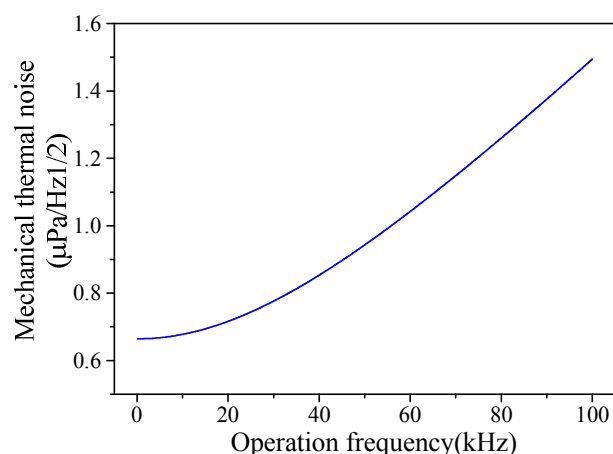


Fig. 3.20 Calculated mechanical thermal noise P_N for different operation frequency of the diaphragm.

Table 3.6 Measured MDP and calculated mechanical thermal noise of the graphene diaphragm based acoustic detector

Operation frequency	Cavity length L	Experimental result of MDP	Mechanical thermal noise P_N
10.1 kHz	68.3 μm	2.11 $\mu\text{Pa}/\text{Hz}^{1/2}$	0.678 $\mu\text{Pa}/\text{Hz}^{1/2}$
16.0 kHz	68.3 μm	9.05 $\mu\text{Pa}/\text{Hz}^{1/2}$	0.698 $\mu\text{Pa}/\text{Hz}^{1/2}$

3.5.4 Long term stability and design of feedback control

In Section 3.5.2, the performances of optical fiber acoustic detector are tested by tuning the a narrow band laser into the Q -point of the interference fringe to achieve a linear response and maximize the sensitivity. However, it was found that operating Q -point often drift due to environmental perturbation such as temperature fluctuation, which leads to long term instability of the demodulation system. Temperature change is one of the key factors that may limit the detection sensitivity, because F-P cavity is sensitive to temperature change. Alternatively, other environmental perturbation such as background pressure change may also lead to instability of the operating Q -point, especially for the F-P cavity based on the ultra-thin graphene diaphragm, the cavity length of which is

easily affected by the background pressure change. Actually these changes are involved in a slow variation process, so the use of the active feedback control may improve the long term stability of the system.

3.5.4.1 Design and the system of feedback control

When the background pressure or the temperature changes, the corresponding deformation of graphene diaphragm within the acoustic detector would change the cavity length, causing the movement of interference spectrum, as shown in Figure 3.21 (a). If the wavelength of the tunable laser remains at the same value, then the wavelength may direct to the peak/valley of the interference spectrum, inducing distortion in the demodulated signal and decreasing the pressure sensitivity of the detector. For example, if the interference spectrum moves toward to the right/left side as the red line, the Q -point would shift from the blue dot to red/pink dot, then the output DC voltage would become higher/lower and non-linear.

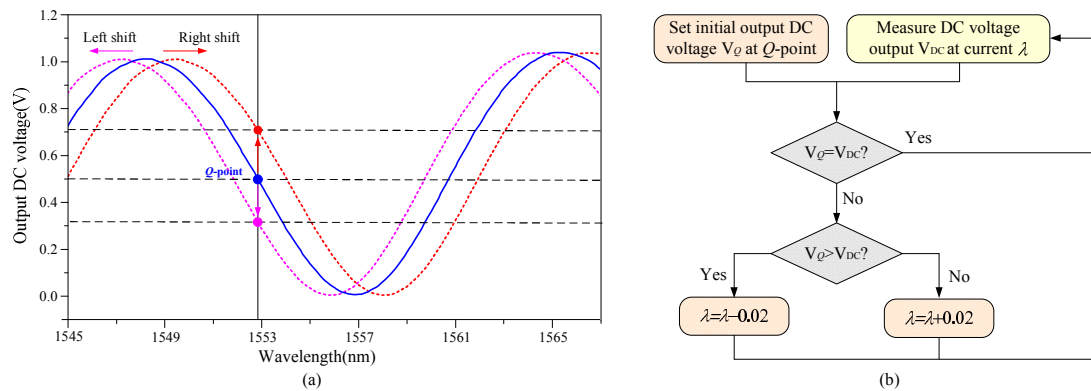


Fig. 3.21 (a) Q -point drifts due to environmental perturbation.(b) The basic process of the Q -point tracking.

Here an electrical feedback control system is introduced to maintain the operating Q -point for long term stability of the optical fiber acoustic detector. The basic concept in this feedback control system is that the wavelength of the input laser is tracking the variation of the Q -point. When the Q -point shifts, the DC output voltage will vary

accordingly, then the Labview program will tune wavelength of the filter so that the wavelength of the input laser can point to the Q -point and the operating point is maintained. As shown in Figure 3.21 (b), the logic of the feedback process is as follow:

(1) The output electrical signal from the PD contains both AC and DC components, so the DC voltage indicating the position of the laser wavelength in the interference spectrum can be used to track the Q -point position.

(2) For example, the peak voltage V_{peak} and bottom voltage V_{bottom} of interference spectrum are 1.04 V and 0.0 V, respectively, as shown in Figure 3.21 (a). So the initial output DC voltage at Q -point $V_Q = V_{bottom} + (V_{peak} - V_{bottom})/2 = 0.52$ V at wavelength of 1552.8 nm.

(3) If the spectrum moves to the right side, the output DC voltage V_{DC} at 1552.8 nm would increase, then the laser wavelength will be tuned and increases by a step of 0.02 nm so that V_{DC} decreases accordingly until $V_{DC} = V_Q$ when the wavelength is tracking at the Q -point, as shown in the Figures 3.21 (a) and (b).

(4) Similarly, if the spectrum moves to the left side, the output DC voltage V_{DC} at 1552.8 nm would decrease, then the laser wavelength will be tuned and decreases by a step of 0.02 nm so that V_{DC} increases accordingly until $V_{DC} = V_Q$ when the wavelength is tracking at the Q -point, as shown in the Figures 3.21 (a) and (b). In the feedback control system, a band pass source (BBS) combined with a programmable optical tunable filter is used as the laser source with the experimental setup shown in Figure 3.22, instead of using the narrow band tunable laser.

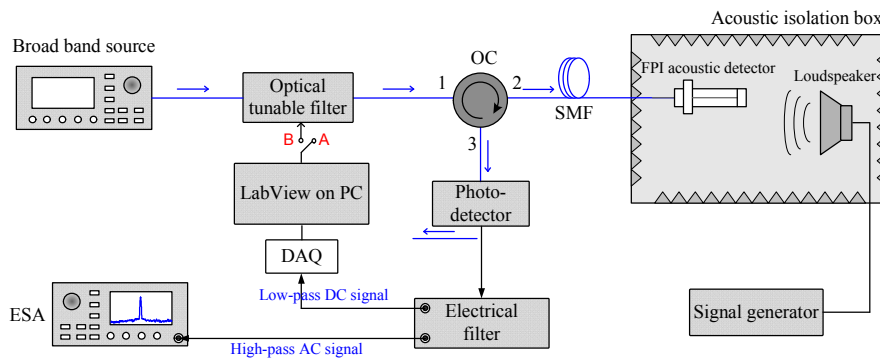


Fig. 3.22 Experimental setup for testing the long term stability of the acoustic detector.

Function illustration of the devices:

(1) Devices preparation

Board band source (BBS);

Programmable optical tunable filter: The bandwidth of this filter is 0.3 nm and it can be tuned under the control of the LabView programme, so that any narrow wavelength could be obtained by using this filter with a board band source (BBS);

Electrical filter: The output electrical signal from the PD contains both DC and AC components, electrical filter can be used to separate these two components into a low-pass DC signal and high-pass AC signal (Model SR650, Stanford research systems, Inc.);

As shown in Figure. 3.22, a BBS with a programmable optical tunable filter, optical circulator (OC), photo-detector (PD), Electrical filter, data acquisition card (DAQ, No. NI USB-6009) and LabView programme in computer are combined together to form feedback control loop to control the output of the optical tunable filter.

(2) The wavelength of tunable filter can be tuned under voltage control from the feedback loop. The feedback loop begins at PD, where the electrical signal is delivered to the electrical filter. Then the electrical signal can be separated into a low-pass DC

signal and high-pass AC signal by the electrical filter. The low-pass DC signal is injected into the DAQ and the LabView programme while the high-pass AC signal is sent to real-time ESA for measurement of acoustic pressure.

(3) The function of the LabView programme is to compare the value of the current DC voltage V_{DC} with the pre-set Q -point voltage V_Q , and then send a control command to the tunable filter regarding this voltage discrepancy, so that the wavelength of tunable filter can be tuned to the corresponding position.

The feedback control can be achieved by the following steps:

(1) The optical tunable filter under the control of the Labview firstly scans several FSR of the interference fringe to obtain the maximum and minimum DC values of the reflected spectrum, from which we can determine the output DC voltage corresponding to the Q point. And the corresponding output will be shown in the real-time waveform columns. Then the peak voltage V_{peak} and bottom voltage V_{bottom} of interference spectrum can be obtained, so the initial Q -point DC voltage V_Q can be calculated by $V_Q = V_{bottom} + (V_{peak} - V_{bottom})/2$;

(2) The calculated an initial V_Q at Q -point is pre-set and the feedback control is started. With a fast response of the Labview command, the wavelength of the filter shows an efficient Q -point tracking and the DC output voltage can remains in a stable level.

3.5.4.2 Stability Test of the sensor before using the feedback control system

Before applying the feedback loop control system, we first test the long-term stability of the optical fiber acoustic detector. The experimental setup is shown in Figure 3.22 with the Labview programme disconnected with the optical tunable filter. The tunable filter is

firstly tuned to the Q -point of the interference spectrum and the acoustic detector is exposed to a continued pressure wave generated by the loudspeaker for 12 hours. The parameters in the test are as follows:

- (1) Q -point wavelength is set at 1552.8 nm;
- (2) Acoustic signal is at 5V and 10 kHz;
- (3) Acoustic pressure level is 10 mPa.

The high-pass AC signal is transferred to ESA for acoustic detection while the low-pass DC signal is delivered to the DAQ and recorded in real-time by a Labview programme. The AC data is recorded every 2 hour while the DC signal is recorded continuously.

Figure 3.23 (a) and Figure 3.23 (b) show respectively the recorded DC and AC output voltage for 12 hours. The DC output varies between 0.5 V and 1.2 V over 12 hours, indicating the operating point is not stable and changes with the temperature fluctuation and background pressure change. For constant applied acoustic pressure, the AC output changed by over 10 dB from above -60 dBm to below -70 dBm, showing the demodulation is instable.

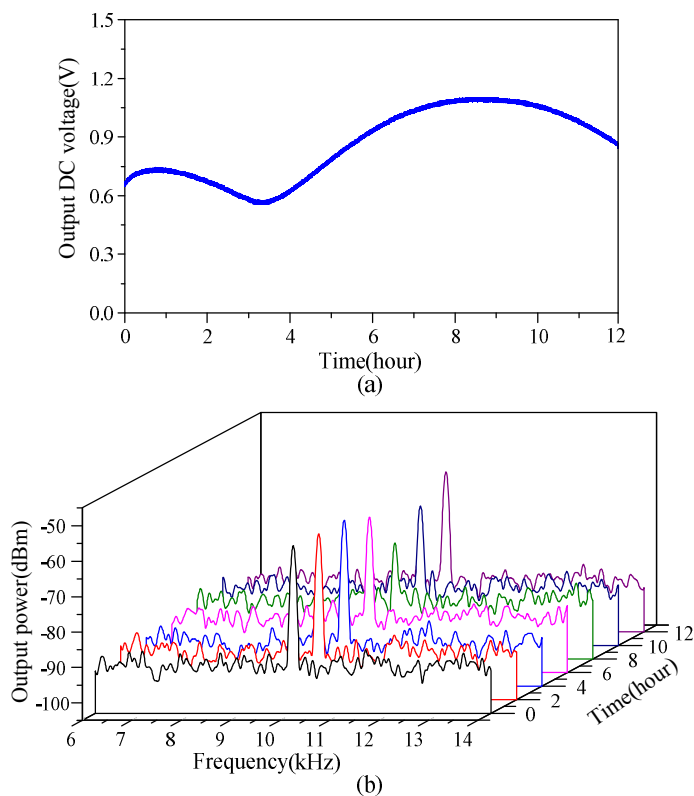


Fig. 3.23 Without feedback control system: (a) DC output voltage of the F-P acoustic detector over 12 hours. (b) Power spectrum of the AC component for an applied acoustic pressure of 10 mPa at 10 kHz over 12 hours.

3.5.4.3 Stability Test of the sensor after using the feedback control system

We then measured the output signals over a similar period by using feedback to stabilize the operating point with the Labview programme disconnected with the optical tunable filter.

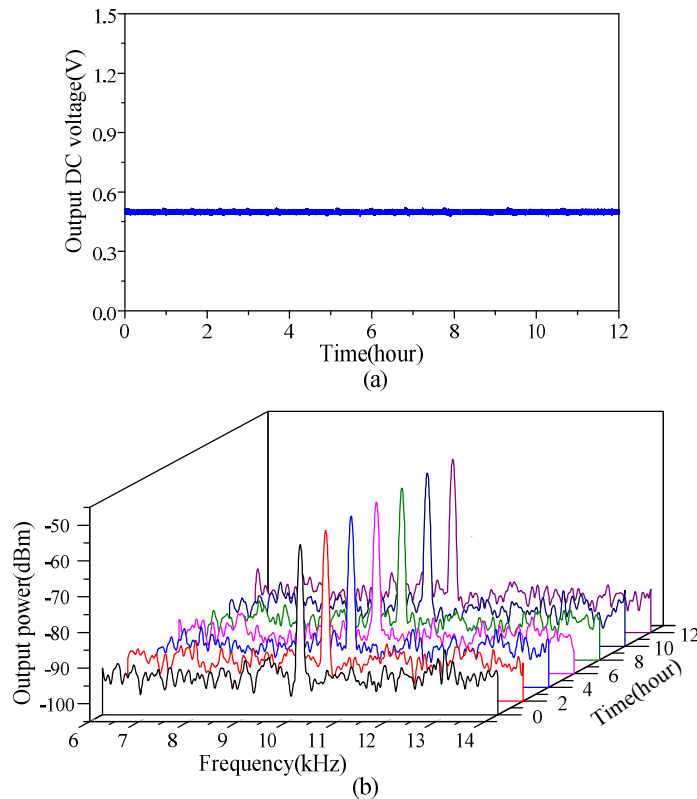


Fig. 3.24 With feedback control system: (a) DC output voltage of the F-P acoustic detector over 12 hours. (b) Power spectrum of the AC component for an applied acoustic pressure of 10 mPa at 10 kHz over 12 hours.

Figure 3.24 (a) and Figure 3.24 (b) show the DC and AC output voltages over a 12-hour period with feedback loop on. The DC output is operating stably at the level of 0.52 V which is the pre-set Voltage in Q -point. The use of active feedback significantly improves the long term stability of the demodulation system and for a constant acoustic pressure of 10 mPa, the AC output remained in a stable level of -58 dBm compared with the results without the feedback loop control in Figure 3.23.

3.6 Summary

In this chapter, the configuration of a F-P cavity is introduced first. For the graphene diaphragm based F-P cavity, the responses of graphene diaphragm under static and dynamic pressure are analyzed, and the demodulation system for diaphragm based F-P cavity is demonstrated. Then the acoustic detector based on multilayer graphene

diaphragm is introduced, including its fabrication, the sensitivity and frequency responses. By operating at one of the mechanical resonances of the 2.5 mm-diameter diaphragm, the sensitivity for acoustic detection is enhanced and a noise equivalent minimum detectable pressure of $2.11 \mu\text{Pa}/\text{Hz}^{1/2}$ at 10.1 kHz is achieved. Finally, a feedback control system for operating point stabilization is designed and applied to the acoustic experiments.

References of Chapter 3

- [1] Y. Cao, "Quartz-enhanced photoacoustic spectroscopy and its association with fiber-optic devices," PhD Thesis, The Hong Kong Polytechnic University (2012).
- [2] U. Komaragiri, M. Begley, and J. Simmonds, "The mechanical response of freestanding circular elastic films under point and pressure loads," *J. Appl. Mech-t ASME* 72, 203-212 (2005).
- [3] J. Ma, "Miniature fiber-tip Fabry-Perot interferometric sensors for pressure and acoustic detection," PhD Thesis, The Hong Kong Polytechnic University (2014).
- [4] J. S. Bunch, "Mechanical and electrical properties of graphene sheets," PhD Thesis, Cornell University, 2008.
- [5] D. Xu and K. Liechti, "Bulge testing transparent thin films with moiré deflectometry," *Exp. Mech.* 50, 217-225 (2010).
- [6] W. Weaver Jr, S. P. Timoshenko, and D. H. Young, *Vibration problems in engineering*, John Wiley & Sons (1990).
- [7] J. Ma, H. Xuan, H. L. Ho, W. Jin, Y. Yang, and S. Fan, "Fiber-optic Fabry-Perot acoustic sensor with multilayer graphene diaphragm," *IEEE Photon. Technol. Lett.* 10, 932-935 (2013).
- [8] B. Yu, D. W. Kim, J. Deng, H. Xiao, and A. Wang, "Fiber Fabry-Perot sensors for detection of partial discharges in power transformers," *Appl. Opt.* 42, 3241-3250 (2003).
- [9] D. Jackson, R. Priest, A. Dandridge, and A. B. Tveten, "Elimination of drift in a single-mode optical fiber interferometer using a piezoelectrically stretched coiled fiber,"

- Appl. Opt. 19, 2926-2929 (1980).
- [10] F. Yang, W. Jin, Y. Lin, C. Wang, H. L. Ho, and Y. Tan, "Hollow-core Microstructured Optical Fiber Gas Sensors," *J. Lightwave Technol.* 35, 3413-3424 (2017).
- [11] A. Yariv and P. Yeh, *Photonics: optical electronics in modern communications*, Oxford University Press New York (2007).
- [12] C. Lee, X. Wei, J. W. Kysar, and J. Hone, "Measurement of the elastic properties and intrinsic strength of monolayer graphene," *science* 321, 385-388 (2008).
- [13] J. Ma, W. Jin, H. L. Ho, and J. Y. Dai, "High-sensitivity fiber-tip pressure sensor with graphene diaphragm," *Opt. Lett.* 37, 2493-2495 (2012).
- [14] J. Ma, W. Jin, H. Xuan, C. Wang, and H. L. Ho, "Fiber-optic ferrule-top nanomechanical resonator with multilayer graphene film," *Opt. Lett.* 39, 4769-4772 (2014).
- [15] S. P. Koenig, N. G. Boddeti, M. L. Dunn, and J. S. Bunch, "Ultrastrong adhesion of graphene membranes," *Nat. Nanotech.* 6, 543-546 (2011).
- [16] Y. Tan, C. Zhang, W. Jin, F. Yang, H. L. Ho, and J. Ma, "Optical fiber photoacoustic gas sensor with graphene nano-mechanical resonator as the acoustic detector," *IEEE J. Sel. Topics in Quantum Electronics* 23, 5600211 (2017).
- [17] T. B. Gabrielson, "Mechanical-thermal noise in micromachined acoustic and vibration sensors," *IEEE Trans. Electron. Devices* 40, 903-909 (1993).

Chapter 4

Optical fiber photoacoustic gas sensor with graphene nano-mechanical resonator as the acoustic detector

4.1 Introduction

Photoacoustic spectroscopy (PAS) is one of the important indirect methods for trace gas detection. It is based on the photoacoustic (PA) effect involving the conversion of light absorption of the target gas into the acoustic pressure wave [1-3]. The generated acoustic pressure wave can be detected by the acoustic detector. In this chapter, we mainly introduce the acoustic detector based on the low finesse diaphragm based Fabry-Perot (F-P) cavity described in Chapter 3. Acetylene detection based on the PA effect by using this acoustic detector is demonstrated in details. Since the acoustic detector is in ~mm scale and graphene is used as the sensing diaphragm, this all-optical fiber gas sensor shows many advantages including compact size, high sensitivity, immune to electromagnetic interference, and it would be ideally suited for remote and distributed sensing applications.

4.2 Basics of PAS gas detection

Figure 4.1 (a) and Figure 4.1 (b) show the basic process for laser-based PAS gas detection. The principle of low finesse diaphragm based F-P cavity for gas detection is PAS [4]. The gas detection process can be divided into the following procedures:

- 1) The wavelength modulated pump beam propagates along the SMF and is incident into the space between two fiber-pigtailed collimated lenses, then the laser energy interacts and is absorbed by the target gas sample, generating a localized periodical heat by the PA effect, resulting in an acoustic wave production. This acoustic

wave has the same frequency of the light modulation.

2) The magnitude of the generated acoustic wave is proportional to gas concentration and can be detected by the graphene diaphragm based F-P acoustic detector described in Chapter 3. This acoustic wave applies on the graphene diaphragm and drives it back and forth periodically;

3) The F-P cavity length is modulated by the periodic diaphragm deflection, then the reflected light intensity from the cavity is also modulated, from which the target gas concentration can be measured by a demodulation system and the lock-in technique.

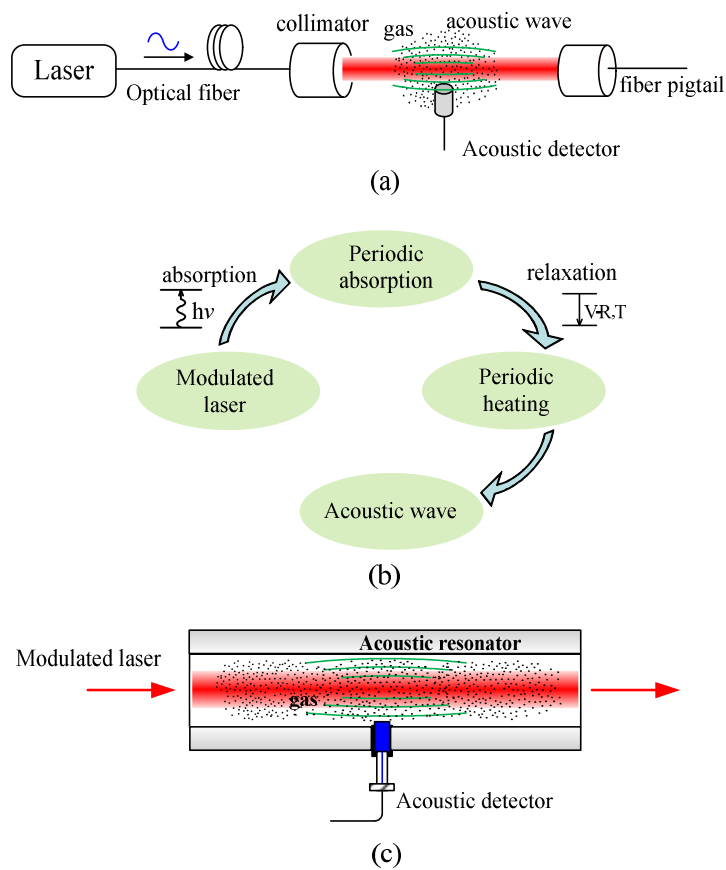


Fig. 4.1 (a) The basic principle of PAS for gas detection. (b) Processes of PA wave generation. (c) a resonating PA cell for signal enhancement [4].

Moreover, using an additional acoustic resonator, the magnitude of the acoustic wave could be further enhanced when the modulation frequency of the pump is tuned to

one of its acoustic resonances shown in Figure 4.1 (c), so higher detection sensitivity can be achieved.

The performances of graphene diaphragm-based FPI as acoustic detectors for gas detection can be characterized by several parameters involving the PA signal, the detection limit of a PAS system in terms of noise equivalent concentration of gas (NEC or $c_{m, \min}$), noise equivalent absorption-coefficient (NEA or α_{\min} , in cm^{-1}), and a normalized NEA (NNEA) measured in $\text{cm}^{-1}\text{W}/\text{Hz}^{1/2}$, and the quality factor Q of the acoustic resonance. The definition of these parameters are shown as:

(1) PA signal S : The PA signal S can be calculated as [5, 6]

$$S = S_m P C_{cell} \alpha \quad \text{in volt (V)} \quad (4.1)$$

where S_m is the sensitivity of the acoustic detector in mV/Pa , P is the power of the pump laser in W , the PA cell response constant C_{cell} is a scaling factor depending on the PA cell geometry, modulation frequency and measurement conditions, in $\text{Pa}/\text{cm}^{-1}\text{W}$. α is the absorption coefficient with $\alpha = N_{tot} c_m \sigma$, where N_{tot} is the total number density of molecules in $\text{molecule}/\text{cm}^3$, c_m is the concentration of the target gas and σ is absorption cross-section. The PA signal is proportional to the gas absorption coefficient α and laser power P , and the use of a well-designed acoustic resonator through optimizing response constant C_{cell} . The sensitivity of acoustic detection (S_m) may also be enhanced by use of a resonant acoustic detector and operating at its resonant frequency.

(2) Detection limit:

The detection limit of a PAS system can be determined by NEC ($c_{m, \min}$) or NEA (α_{\min}), through a relationship of

$$c_{m, \min} = \frac{\alpha_{\min}}{N_{tot} \cdot \sigma} \quad (4.2)$$

The value of NEA (α_{\min}) is calculated by equaling the PA signal to that of the noise level (i.e., SNR=1). Since the PA signal is proportional to the laser power with the noise proportional to the detection bandwidth, NEA is then proportional to the square root of the bandwidth and inversely proportional to the laser power. A normalized NEA (NNEA) can be defined as the value of NEA normalized to 1 Hz measurement bandwidth and 1 W laser power, and measured in $\text{cm}^{-1}\text{W}/\text{Hz}^{1/2}$ [6].

(3) **Quality factor Q :** Q -factor of the resonance is defined as $Q=f_0/\Delta f_{\text{FWHM}}$, where f_0 and Δf_{FWHM} are the resonant frequency and the full width at half maximum (FWHM) of the resonance profile, respectively.

4.3 Gas detection experiments

4.3.1 Resonant and non-resonant detection

The performances of PAS gas (acetylene) detection system with the optical fiber acoustic detectors operating at resonant and non-resonant modes were conducted using the setup shown in Figure 4.2. The acoustic detector is prepared and fabricated in Chapter 3.

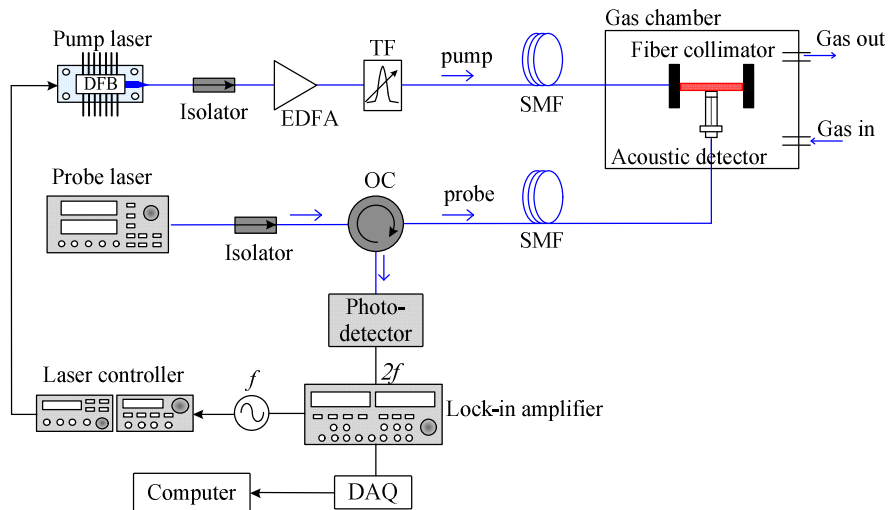


Fig. 4.2 Experimental setup of the PAS system for acetylene detection.

With the experimental setup shown in Figure 4.2, the measurement can be

conducted by the following steps:

(1) A distributed feedback (DFB) laser is used as the pump source (λ_{pump}) with wavelength tuned to one of the absorption line of the target gas, for example, the P(13) absorption line of acetylene at 1532.830 nm. The pump beam wavelength modulated sinusoidally at a frequency of $f=22.8$ kHz, corresponding to one of the resonances of the acoustic detector, and collimated with a fiber collimator with a beam diameter of ~ 300 μm . Then a PA wave with the same frequency of the light modulation is generated. The amplitude of wavelength modulation was set to ~ 2.2 times of the absorption linewidth in order to maximize the second-harmonic signal [7].

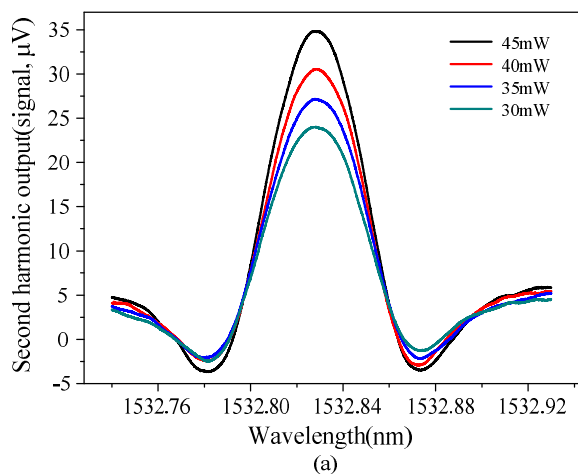
(2) The PA signal is detected by use of the fabricated F-P acoustic detector and the end of the F-P with graphene diaphragm is placed adjacent to collimated pump beam.

(3) The acoustic wave induced periodic diaphragm deflection, which was probed by an external cavity diode laser (ECDL) with output power of ~ 1 mW. The wavelength of the probe laser (λ_{probe}) is tuned to 1551.9 nm, corresponding to steepest slope of the interference, which produces the largest change in output power for a given acoustically induced vibration.

(4) The reflected probe light from the detector travels back along the same fiber and was detected by a photo-detector (PD). The output from the PD is demodulated by a lock-in amplifier (Stanford research systems, SR830) at its second harmonic frequency (i.e., 45.6 kHz). The space within the collimator was filled with 100 p.p.m. acetylene balanced by nitrogen (N_2). The time constant of the lock-in amplifier is set to 10 s with a filter slope of 18 dB Oct⁻¹. All the experiments were carried out at atmospheric pressure and room temperature.

Figure 4.3 (a) shows the second harmonic lock-in outputs for different pump power levels delivered to the fiber collimator when the pump wavelength was scanned across

the P(13) line of acetylene. We can see that the output signal increases with the pump power level. For the pump power of 45.1 mW, the peak-to-peak amplitude of the second harmonic signal is $\sim 38.2 \mu\text{V}$. The second harmonic lock-in output when the pump is tuned away from the absorption peak to 1,532.93 nm is shown in Figure 4.3 (b). The standard deviation (s.d.) of the noise over 8-min duration is $0.16 \mu\text{V}$, not much larger than the noise level ($0.11 \mu\text{V}$) when the pump is off, giving a signal to noise ratio (SNR=peak-to-peak amplitude of the second harmonic signal/std. of the noise) of 238. So the lower detection limit for a signal to noise ratio of unity is estimated to be 418 ppb in NEC (NEC=gas concentration/SNR) for a detection bandwidth of 0.0094 Hz. Moreover, the second harmonic signal and the standard deviation (s.d.) of the noise as functions of pump power level are shown in Figure 4.3 (c). The second harmonic output signals for different pump power levels are shown in black squares. Curve fitting shows that it has a linear relationship ($r^2=0.9960$) with the pump power in the range of 17 to 45 mW. The s.d. of the noise as functions of pump power levels are shown in blue squares, showing that the noise level remained in a relatively plane level.



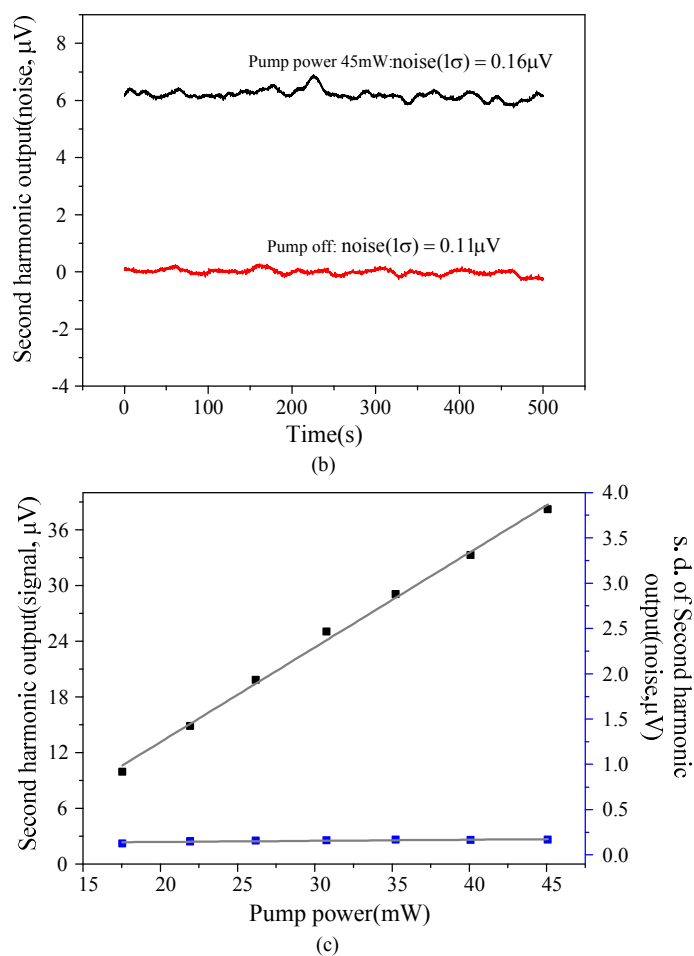


Fig. 4.3 Experimental results for the acetylene detection. (a) Second harmonic lock-in output (signal) when pump laser is tuned across the P(13) line of acetylene at 1,532.83 nm under different pump power levels. (b) Second harmonic lock-in output (noise) when the pump wavelength is tuned away from absorption and to 1,532.93nm. (c) Second harmonic signal and the s.d. of the noise as functions of pump power level.

The effect of varying modulation frequency on the amplitude of the second harmonic output signal is also investigated. The modulation frequency of DFB pump laser is tuned from 21 kHz to 25 kHz and the corresponding second harmonic lock-in signal is shown in Figure 4.4. The power of the pump laser is fixed to 45 mW. From the figure, we can see that the output signal is maximized at ~ 22.8 kHz with output signal of ~ 50 μV , corresponding to the resonant frequency of the graphene nano-mechanical resonator [8]. And the output signal is minimized at ~ 21.05 kHz with output signal of ~ 5 μV , corresponding to a non-resonant frequency of the graphene nano-mechanical

resonator. The Q factor of this graphene resonator is calculated to be 13.

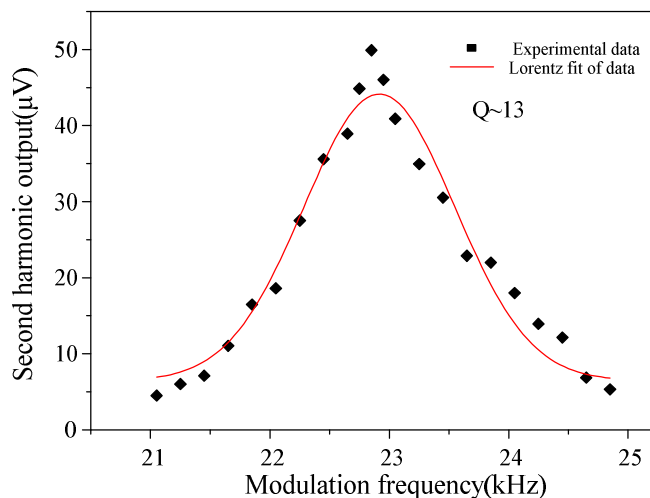


Fig. 4.4 Second harmonic lock-in output under different modulation frequencies when the pump laser is tuned to the P(13) absorption line and fixed to 1532.83 nm.

Table 4.1 Performance of gas sensor for two different modulation frequencies

Modulation Frequency (kHz)	2nd harmonic output at absorption peak (1532.83 nm)	2nd harmonic output away from absorption peak (1532.93 nm)	s.d. of noise over 500s	SNR	NEC
22.84 kHz (at resonance)	49.92 μV	5.62 μV	0.169 μV	262	0.38ppm
21.05 kHz (at resonance)	4.49 μV	1.17 μV	0.128 μV	25	4ppm

To compare the performance of the PAS gas sensor operating at the resonant and non-resonant frequencies, we evaluated signals and the noises at 22.84 kHz (at resonance) and 21.05 kHz (off resonance), which are shown in Table 4.1. The SNR of the PA gas sensor at resonance is 262, which is ~ 10 times better than that in the

non-resonance with SNR of 25, showing the system performance can be significantly improved by operating the graphene diaphragm at resonance. The lower detection limit at the resonance (22.84 kHz) for SNR=1 is estimated to be 381 ppb in NEC, which is ~10 times better than that in the non-resonance of 4 ppm and in accordance with the calculated Q factor of 13.

4.3.2 Operating at different acoustic resonances

The performances of the PAS gas sensor operating at two acoustic resonances around 5 and 22 kHz were also investigated. The experimental setup is similar to that shown in Figure 4.2, but a DFB laser with different wavelength range of 1530.371 nm located in the P(9) absorption line is used. The pump power used is 123.9 mW and acetylene concentration of 100 ppm. The time constant of the lock-in amplifier is set to 3 s with a filter slope of 18 dB/oct.

Figure 4.5 shows the second harmonic lock-in output when the pump wavelength is scanned across the P(9) line and the pump laser is modulated around 5 and 22 kHz. The peak to peak value of the second harmonic outputs are similar at 5 and 22 kHz which are around 160 μ V. However, the noise level at 5 kHz is ~4 times larger than that at 22 kHz. The NEC and NNEA values at 5 kHz are calculated to be 450 ppb and $3.7 \times 10^{-7} \text{ cm}^{-1} \text{ WHz}^{-1/2}$. The NEC and NNEA values at 22 kHz are calculated to be 119.8 ppb and $9.782 \times 10^{-8} \text{ cm}^{-1} \text{ WHz}^{-1/2}$. Table 4.2 shows the signals and the noises at different modulation frequencies at and away from the absorption line center. The detection sensitivity can be improved by operating the graphene diaphragm at a resonance with a higher resonance frequency since the SNR is better at higher frequencies due to smaller environmental noise.

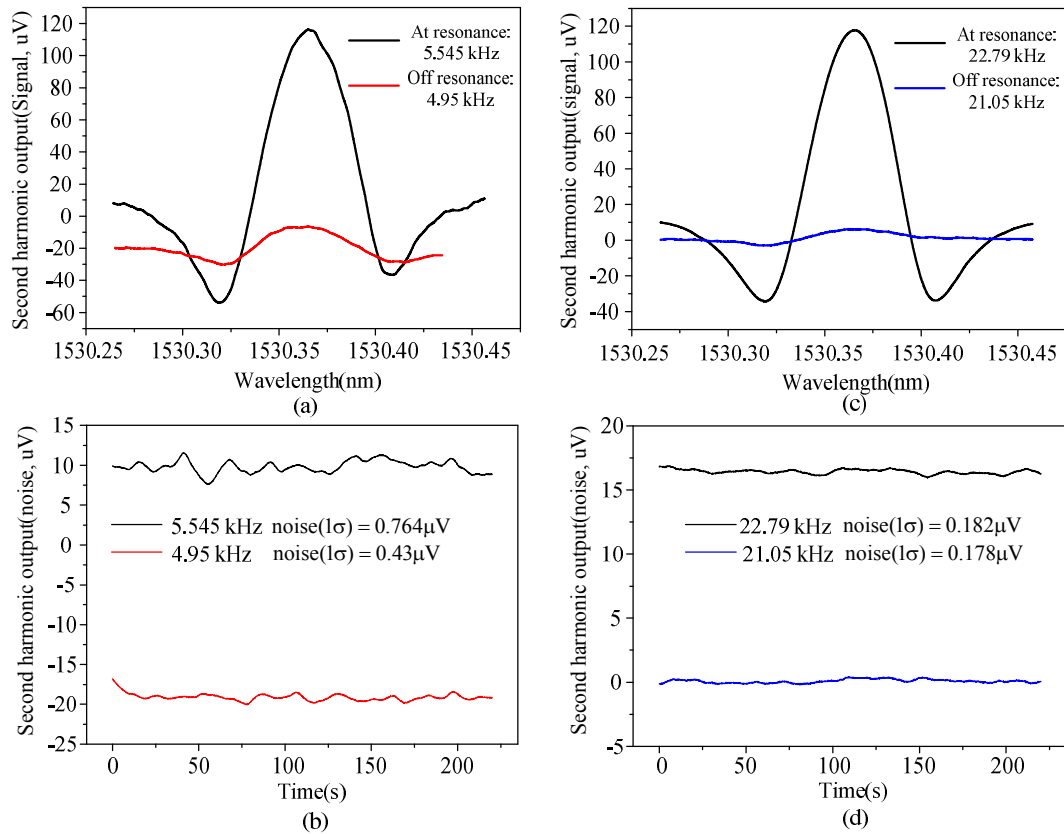


Fig. 4.5 Experimental results for the acetylene detection at two specific resonances around (a, b) 5 kHz and (c, d) 22 kHz. (a) Second harmonic lock-in output (signal) at resonance of 5.545 kHz (black curve) and off resonance of 4.95 kHz (red curve). (b) Second harmonic lock-in output (noise) when the pump wavelength is tuned away from the absorption peak to 1,530.26 nm at acoustic resonance of 5.545 kHz (black curve) and off acoustic resonance of 4.95 kHz (red curve). (c) Second harmonic lock-in output (signal) at resonance of 22.79 kHz (black curve) and off resonance of 21.05 kHz (blue curve). (d) Second harmonic lock-in output (noise) when the pump wavelength is tuned away from the absorption peak to 1,530.26 nm at resonance of 22.79 kHz (black curve) and off resonance of 21.05 kHz (blue curve).

Table 4.2 Detection limits of graphene diaphragm based pas gas sensors

Modulation frequency	2 nd harmonic output at absorption peak (1530.371 nm)	2 nd harmonic output away from absorption peak (1530.26 nm)	2 nd harmonic output signal	s.d. of noise over 200s	SNR	NEC (ppm)	NNEA (cm ⁻¹ W/Hz ^{1/2})
5.545 kHz (at resonance)	115.66 μV	-52.57 μV	158.2 μV	0.764 μV	220	0.45	3.707 × 10 ⁻⁷
4.95 kHz (off resonance)	-6.50 μV	-30.04 μV	23.54 μV	0.430 μV	55	1.83	1.492 × 10 ⁻⁶
22.79 kHz (at resonance)	117.70 μV	-34.21 μV	151.9 μV	0.182 μV	835	0.12	9.782 × 10 ⁻⁸
21.05 kHz (off resonance)	6.27 μV	-2.88 μV	9.15 μV	0.178 μV	51	1.94	1.587 × 10 ⁻⁶

NNEA, Normalized noise equivalent absorption coefficient; NEC, noise equivalent concentration

4.4 Improvement of detection sensitivity

Using a nano-mechanical resonator with higher Q -factor, the detection sensitivity of the PAS gas sensor can be improved. The graphene diaphragm can be considered as a thin circular plate with its edges clamped. The radius and thickness of the graphene diaphragm are denoted as r and t . Assuming that the graphene diaphragm is in contact with a Newtonian fluid (air), the Q -factor (Q_{tot}) contains two terms about the effect of acoustic radiation and viscous damping, so Q_{tot} of the resonator may be expressed as [9-11]

$$Q_{tot} = \frac{1}{1/Q_{ar} + 1/Q_{vis}} \quad (4.3)$$

where Q_{ar} and Q_{vis} are the acoustic radiation and viscosity term of the Q -factor

$$\text{with } Q_{ar} = 1.20 \frac{\rho_p c_f}{\rho_f c_p} (1 + \beta)^{3/2}; Q_{vis} = \frac{0.95}{\xi} \left(\frac{1}{\beta} + 1 \right) \quad (4.4)$$

where $\xi = \sqrt{\frac{\nu}{\omega_1 r^2}}$ is a non-dimensional parameter, and ν is the kinetic viscosity of the fluid. Taking the fundamental mode of vibration as an example, ω_1 can be expressed as

$$\omega_1 = \frac{10.21}{\sqrt{12(1+\beta)}} \frac{tc_p}{r^2} \quad (4.5)$$

where c_p is the velocity of propagation of waves in the plate, and β is the added virtual mass factor

$$\text{with } c_p = \sqrt{\frac{E}{(1-\nu^2)\rho_p}}; \beta = 0.6689 \frac{\rho_f r}{\rho_p t} \quad (4.6)$$

where E , ν , and ρ_p are the Young's modulus, Poisson's ratio and mass density of graphene diaphragm, ρ_f is the density of the surrounding fluid.

The Q -factor of the graphene in air is calculated by Eq. (4.3) at atmospheric pressure and room temperature, where the physical parameters of the graphene diaphragm and air used for the calculation are listed in Table 4.3 [9, 10]. For a graphene diaphragm with radius of 1.25 mm and thickness of 100 nm, Q_{ar} and Q_{vis} are calculated to be 455 and 15, respectively, so the Q_{tot} value is 14 of the diaphragm, showing that the viscous damping term dominates in the Q_{tot} value of the diaphragm when it vibrates at atmospheric pressure. When the pressure decreases below 1 Pa, the air damping term can be negligible compared to the intrinsic damping of the vibrating diaphragm and the Q -factor may increase significantly [12]. We can infer that the Q -factor in vacuum would become 455 or larger, so that the lower detection limit for gas detection would be $< \sim 4.2$ ppb.

Table 4.3 Physical parameters of graphene diaphragm and air

Graphene diaphragm	Diameter $2r$ (mm): 2.5	Density ρ_p (kg/m ³): 2200
	Thickness t (nm): 100	Poisson ratio ν : 0.17
	Young's modulus E : ~1TPa	
Air(at 1atm, room temperature)	Dynamic viscosity μ (Pa·s): 1.8×10^{-5}	Density ρ_f (kg/m ³): 1.18
	Kinetic viscosity ν (m ² /s): 1.53×10^{-5}	Speed of sound c_f (m/s): 343

4.5 Summary

In this chapter, acetylene detection based on the PA effect is demonstrated by using a graphene diaphragm acoustic detector. A DFB laser is used as a pump laser with its wavelength tuned to the P(9) absorption line of acetylene, while an ECDL is used as the probe beam with its wavelength tuned to a linear response region of the F-P interference. A lower detection limit of 119.8 ppb can be achieved when the modulation frequency is operating at one of the mechanical resonances of the diaphragm with 123.9 mW pump power. Theoretical analysis shows that the detection sensitivity can be further improved to sub-ppb level by increasing the Q -factor of the resonator at low gas pressures. The all-fiber photoacoustic gas sensor shows many advantages including compact size, high sensitivity, immune to electromagnetic interference, and it would be ideally suited for remote and distributed sensing applications.

References of Chapter 4

- [1] A. Miklós, P. Hess, and Z. Bozóki, "Application of acoustic resonators in photoacoustic trace gas analysis and metrology," *Rev. Sci. Instrum.* 72, 1937-1955 (2001).
- [2] T. Schmid, "Photoacoustic spectroscopy for process analysis," *Anal. Bioanal. Chem.* 384, 1071-1086 (2006).
- [3] A. Elia, P. M. Lugarà, C. Di Franco, and V. Spagnolo, "Photoacoustic techniques for trace

-
- gas sensing based on semiconductor laser sources,” *Sensors* 9, 9616-9628 (2009).
- [4] Y. Tan, C. Zhang, W. Jin, F. Yang, H. L. Ho, and J. Ma, “Optical fiber photoacoustic gas sensor with graphene nano-mechanical resonator as the acoustic detector,” *IEEE J. Sel. Topics in Quantum Electronics* 23, 5600211 (2017).
- [5] J. Li, X. Gao, L. Fang, W. Zhang, and H. Cha, “Resonant photoacoustic detection of trace gas with DFB diode laser,” *Opt. Laser Technol.* 39, 1144-1149 (2007).
- [6] P. Patimisco, G. Scamarcio, F. K. Tittel, and V. Spagnolo, “Quartz-enhanced photoacoustic spectroscopy: a review,” *Sensors* 14, 6165-6206 (2014).
- [7] S. Schilt, L. Thevenaz, and P. Robert, “Wavelength modulation spectroscopy: combined frequency and intensity laser modulation,” *Appl. Opt.* 42, 6728-6738 (2003).
- [8] J. Ma, W. Jin, H. Xuan, C. Wang, and H. L. Ho, “Fiber-optic ferrule-top nanomechanical resonator with multilayer graphene film,” *Opt. Lett.* 39, 4769-4772 (2014).
- [9] J. Ma, H. Xuan, H. L. Ho, W. Jin, Y. Yang, and S. Fan, “Fiber-optic Fabry–Perot acoustic sensor with multilayer graphene diaphragm,” *IEEE Photonics Technol. Lett.* 10, 932-935 (2013).
- [10] M. Olfatnia, Z. Shen, J. Miao, L. Ong, T. Xu, and M. Ebrahimi, “Medium damping influences on the resonant frequency and quality factor of piezoelectric circular microdiaphragm sensors,” *J. Micromech. Microeng.* 21, 045002 (2011).
- [11] H. Lamb and R. Southwell, “The vibrations of a spinning disk,” *Proc. Royl. Soc. London.* 99, 272-280 (1921).
- [12] F. Blom, S. Bouwstra, M. Elwenspoek, and J. Fluitman, “Dependence of the quality factor of micromachined silicon beam resonators on pressure and geometry,” *J. Vac. Sci. Technol. B* 10, 19-26 (1992).

Chapter 5

Resonating hollow-core fiber photonic microcell

5.1 Introduction

The conventional configurations such as free-space absorption cells have been used for conventional direct absorption spectroscopy. Their sensitivity can be improved by increasing the absorption path length. However, the absorption path lengths in free space are limited because they may suffer from unavoidable diffraction, causing the light to disperse and intensity to drop as it propagates. Compared with the free-space absorption cells, HC-PBF would be an ideal waveguide since it has most of optical power propagating in the central hollow-cores (e.g., 95%) and allows a perfect overlap between propagating light and gas-phase materials. Moreover, the HC-PBF is compact size and low loss, which make it as a good platform for strong light-gas interaction over long distance.

This chapter will present a novel resonating hollow-core photonic bandgap fiber (HC-PBF) photonic microcell which can be used to enhance the performance of DAS and PT gas sensor in Chapter 6 and Chapter 7. The resonating microcell introduced in this chapter is made by jointing a piece of HC-PBF with two single mode fibers (SMFs) with mirrored ends. We first introduce the construction and fabrication of the resonating microcell, then the characterization of the microcell will be presented in details.

5.2 Resonating hollow-core fiber photonic microcell

5.2.1 Construction of a resonating HC-PBF photonic microcell

In order to implement long optical pathlength, a novel resonating HC-PBF photonic

microcell is proposed, as shown in Figure 5.1 (a). It is formed by sandwiching a piece of HC-PBF between two dielectric mirrors made at the ends of two SMFs, which forms a high finesse Fabry-Perot (F-P) cavity. The length of such a microcell can be from centimeters to meters, which is highly suitable for high sensitivity gas detection with long absorption pathlength. Figure 5.1 (b) shows the scanning electronic microscope (SEM) cross-section image of the HC-1550-06 fiber used in this investigation. The core diameter of the HC-PBF is $\sim 11 \mu\text{m}$. The SMFs with coated mirrors are directly aligned or spliced to the HC-PBF, and the bulky mode-matching lenses are not needed in this situation. The transmission loss of the HC-1550-06 fiber is very low ($\sim 24 \text{ dB/km}$ quoted from NKT Photonics website), which gives a loss of 0.0024 dB for $\sim 10 \text{ cm}$. For the purpose of gas filling into the hollow-core, a small gap ($< 1 \mu\text{m}$) can be kept at one or both of the HC-PBF/SMF joints. Alternatively, low-loss micro-channels may be made from the side of the HC-PBF to achieve faster gas filling into the hollow-core.

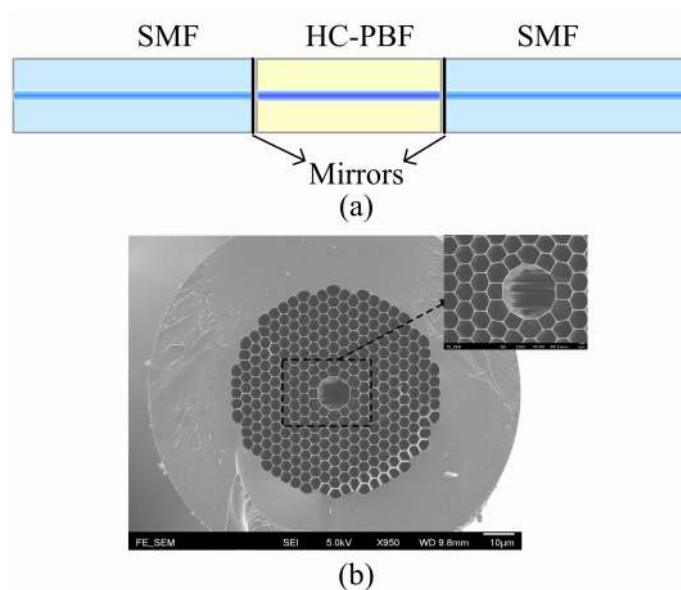


Fig. 5.1 (a) Schematic of the proposed resonating HC-PBF photonic microcell. (b) Scanning electron microscopy (SEM) image of the HC-1550-06 fiber's cross-section.

5.2.2 Fabrication of a resonating HC-PBF photonic microcell

5.2.2.1 Fiber preparation and mirror coating

The dielectric mirror we used is made by placing a number of dielectric layers on a polished SMF endface substrate, as shown in Figure 5.2. The dielectric mirrors consist of the alternating quarter-wave stacks of high-index and low-index materials, such as Titanium dioxide and silicon dioxide (TiO_2 and SiO_2 , refractive index $n_{\text{SiO}_2} = 1.455$ and $n_{\text{TiO}_2} = 2.5$). The coating typically has 19 layers of alternating dielectric materials and the thickness is 4.7 μm for high reflectivity in wavelength of 1550 nm.

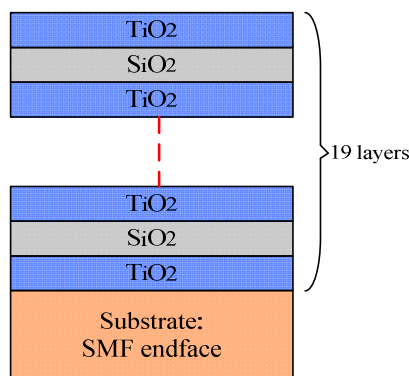


Fig. 5.2 Schematic of the dielectric mirrors.

As shown in Figure 5.3, the mirror coating process can be divided into the following procedures:

- (1) Firstly, a SMF is cleaved by a fiber cleaver, and then the cleaved SMF is inserted into the ferrule so that the cleaved endface can be maintained in the same plane with the ferrule and fixed with epoxy, shown in Figure 5.3(a).
- (2) This assembly is then end polished on the rotary polishing machine to flatten the surface of the cleaved fiber end shown in Figure 5.3(b), and then the flattened surface is checked individually for end contaminations.

(3) After inspecting, the assembly is coated by the ion beam sputtering process or thermal evaporation, shown in Figure 5.3(c).

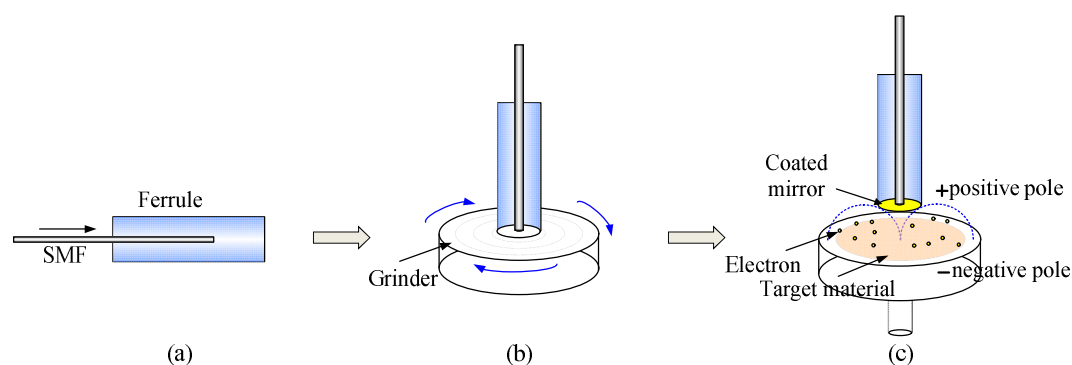


Fig. 5.3 Fabrication process of the dielectric mirror.

Figure 5.4 (a) shows the cross-section of the coated dielectric mirror on fiber end and Figure 5.4 (b) shows a bundle of fabricated SMF pigtailed with dielectric mirror.

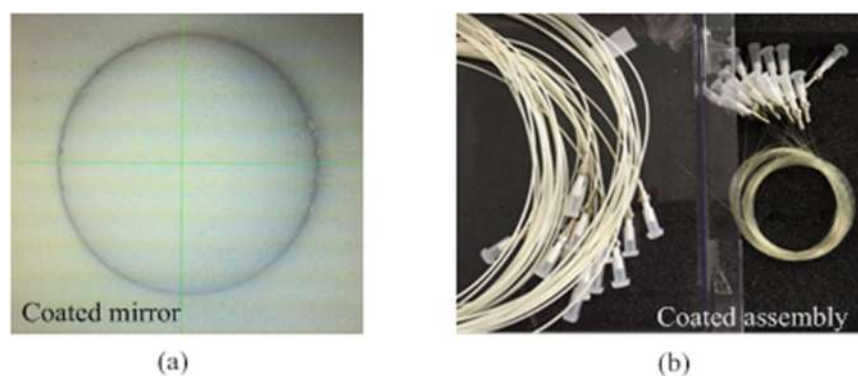


Fig. 5.4 The photos showing (a) the cross-section of the dielectric mirror and (b) a bundle of SMF pigtailed with dielectric mirror.

5.2.2.2 Evaluation of the mirror reflectivity and cavity finesse

After the fabrication of the fiber assembly with mirrors, we need to measure their reflectivity to select the mirrors with better performance to fabricate the cavity with higher finesse. Figure 5.5 shows the experimental setup for mirror reflectivity measurement. A broadband light source (BBS) is propagating into a prepared SMF pigtail with reflective mirror via an optical circulator, and then the reflective light is

received by an optical spectrum analyzer (OSA). Figure 5.6 shows the measured reflective spectrum of the fiber pigtail with mirrored end. It shows reflectivity of the mirror is from 90% to 99.4% at the wavelength from 1500 nm to 1600 nm. The corresponding theoretical finesse are calculated from 30-522 in this wavelength range.

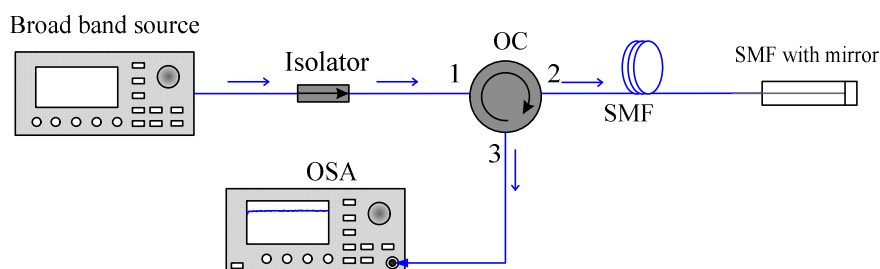


Fig. 5.5 Experimental setup for mirror reflectivity measurement.

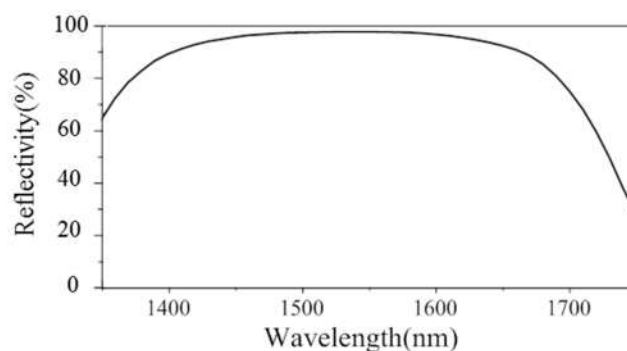


Fig.5.6 The measured reflectivity of the dielectric mirrors.

Actually not all the SMFs with coated mirrors can be used for the fabrication of the F-P cavity since the coating quality of each mirror is different, so high quality coated mirror should be selected in the first step. Here the method of forming an extrinsic Fabry-Perot cavity can be used to identify the quality of the mirror, and higher finesse of the extrinsic F-P cavity indicates the higher reflectivity of the mirror. The finesse F of a cavity is defined by $F=FSR/\delta\nu$, where FSR and $\delta\nu$ are the free spectral range and full-width half-maximum spectral width (FWHM: $\delta\nu$) of the cavity resonances. The extrinsic Fabry-Perot cavity is formed by aligning two pieces of SMFs with mirrored ends, shown in Figure 5.7.

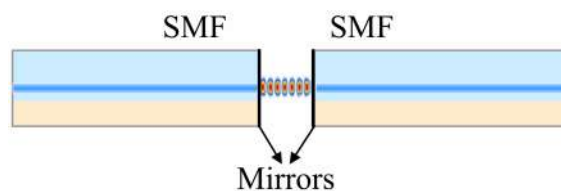


Fig. 5.7 Extrinsic Fabry-Perot cavity made by aligning two SMFs with mirrored ends.

The fabrication procedure is as followed, shown in Figure 5.8:

- (1) Two SMF pigtailed are coated with high reflective dielectric mirror by the process described in Section 5.2.2.1.
- (2) Two SMFs coated with mirror are butt connected to each other to form the extrinsic F-P cavity by mechanical splicing. With inner and outer diameter of $125\ \mu\text{m}$ and $2.5\ \text{mm}$, two fiber ferrules with the coated SMFs inserted were plugged into both sides of a mechanical splicer with an inner diameter of $2.5\ \text{mm}$, respectively. The splicer aligns the two ferrules and holds them together tightly with a small gap left between the ferrules.
- (3) With the aid of a microscope and two translation stages, a cavity length of different values was left between the two fiber ends via inspection from the microscope.

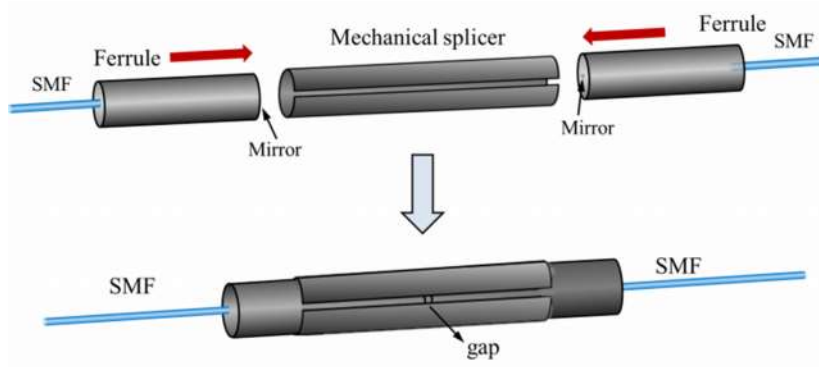


Fig. 5.8 Fabrication procedures of an extrinsic F-P cavity.

For the extrinsic F-P cavity, the cavity length is typically under the value of $\sim 20\ \mu\text{m}$ since the beam divergence at the exit of the SMF with mirrored end would result in

cavity loss which in turn reduces the finesse. Therefore the corresponding FSR of the transmission spectrum is typically significantly large. For example, a F-P with a cavity length of $20\ \mu\text{m}$ gives a FSR of $\sim 60\ \text{nm}$ at the wavelength of $1.55\ \mu\text{m}$. The transmission spectrum of the fabricated cavity can be measured by the experimental setup shown in Figure 5.9. The two SMF pigtails of the cavity are connected to a BBS and an OSA, respectively, to record the transmission spectrum.

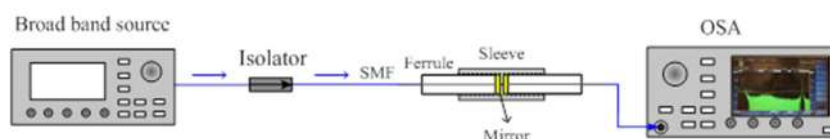


Fig. 5.9 Experimental setup for F-P cavity transmission measurement.

Figure 5.10 shows the measured transmission spectrum of the cavity with different cavity lengths. From this figure, we can see that the finesse for cavity length of $6\ \mu\text{m}$ is 55, corresponding to mirror reflectivity of 94%. The finesse decrease rapidly when the cavity length increases, the finesse becomes very small when the cavity length exceeds $20\ \mu\text{m}$. Therefore the length of an extrinsic F-P cavity is limited since the beam divergence at the output of the SMF would induce cavity loss, affecting the value of the cavity finesse.

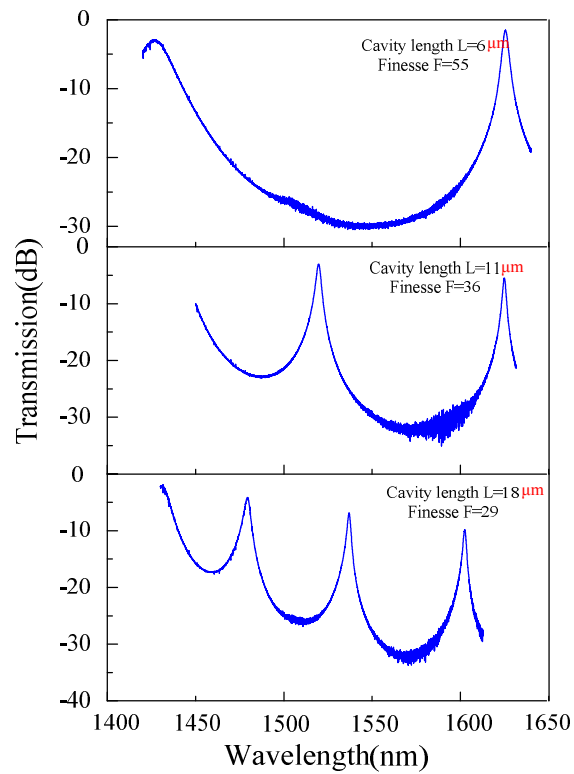


Fig. 5.10 Different finesse values for different cavity lengths.

For the cavity with higher reflective mirrors, the measured transmission spectrum is shown in Figure 5.11, the finesse is measured to be $89.1\text{nm}/0.29\text{ nm}=307$, corresponding to an effective mirror reflectivity of 99%, which can be used for fabrication of resonating HC-PBF photonic microcell.

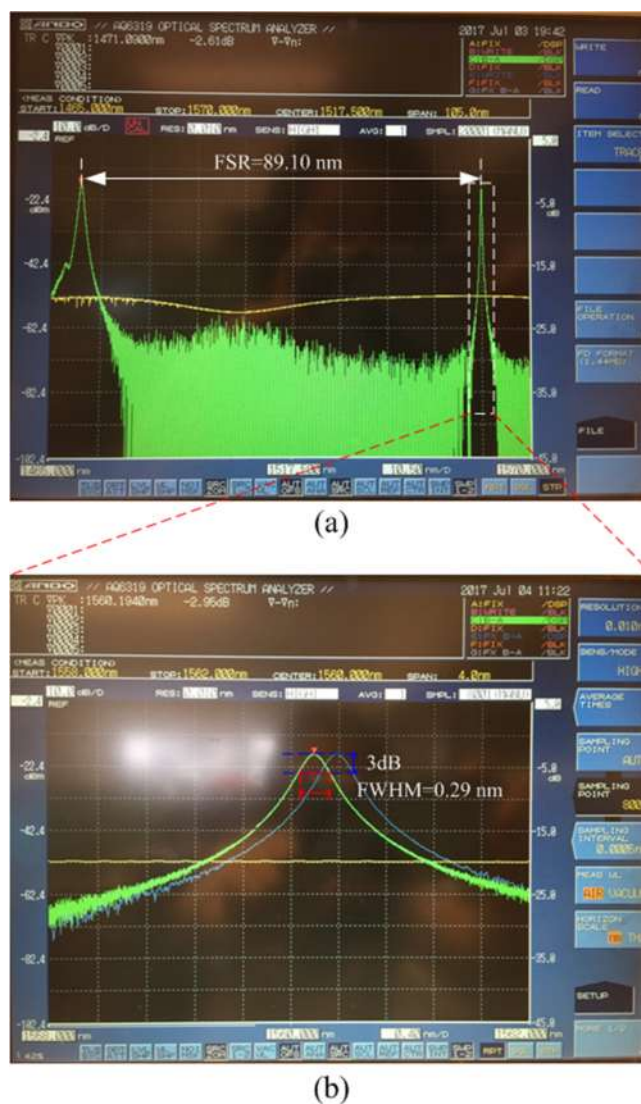


Fig. 5.11 Measured transmission spectrum of the F-P cavity with (a) wavelength from 1465 nm to 1570 nm, (b) wavelength from 1558 nm to 1562 nm.

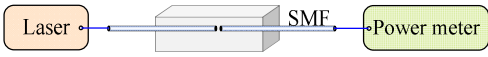
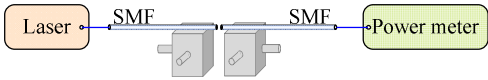
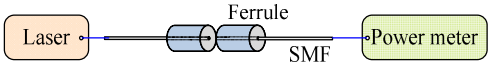
5.2.2.3 Alignment and test of between SMF and HC-PBF

One of the most difficult parts of the photonic microcell fabrication is to achieve a perfect alignment between the SMF and the HC-PBF. Before discussing the alignment of the HC-PBF microcell, we first consider the alignment between two SMFs and between the SMF and HC-PBF by different methods, including fiber fusion splicer as a standard reference for alignment, spatial translation stages and mechanical splicing.

1. Alignment between SMFs

As shown in Table 5.1, two SMFs are cleaved by fiber cleaver and then aligned to each other by fiber fusion splicer, spatial translation stages and mechanical splicing.

Table 5.1 Losses of different methods for alignment.

Methods of alignment	Alignment diagram	Alignment loss
Fiber fusion splicer		-1.20 dB
Spatial translation stages		-1.44 dB
Mechanical splicing		-1.27 dB

For fiber fusion splicer, two cleaved SMF ends are clamped inside a fusion splicer, and then the three dimensional controller of the splicer are adjusted to achieve the minimum alignment loss.

For spatial translation stages, two cleaved SMF ends are clamped on the surface of the stages, and the three dimensional controller of the stages are adjusted to achieve minimum loss.

For mechanical splicing, two cleaved SMF ends are inserted and fixed into the ferrules by epoxy, respectively. Both ferrules are inserted into a ceramic sleeve at both ends and approach to each other gradually to achieve minimum loss.

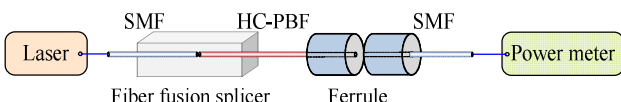
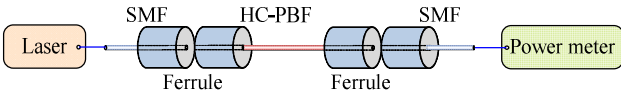
The other end of both SMF pigtails are connected to a laser source and a power meter respectively. The corresponding alignment losses for these three methods are measured to be -1.20 dB, -1.44 dB and -1.27 dB, respectively. Therefore the method of mechanical splicing for alignment between SMFs can be similar with the fiber fusion splicer, and the method of spatial translation stages induces higher loss compared with the other two methods. So in the following cavity alignment, we adopt the mechanical

splicing for cavity fabrication.

2. Alignment between SMF and HC-PBF

In order to investigate whether the mechanical splicing is suitable for the alignment between SMF and HC-PBF, we also compare the alignment losses between fiber fusion splicer and mechanical splicing, as shown in Table 5.2.

Table 5.2 Performance of different methods for alignment.

Methods of alignment	Alignment diagram	Alignment loss
Fiber fusion splicer		-5.43 dBm
Mechanical splicing		-5.62 dBm

(1) One end of a SMF and a HC-PBF are cleaved firstly, and then both cleaved ends are inserted and fixed into the ferrules by epoxy, respectively. Then two ferrules are inserted into a ceramic sleeve at both ends and approach to each other gradually to achieve minimum loss. This SMF/HC-PBF joint is regarded as the fixed end.

(2) The other end of the HC-PBF and one end of a new SMF are also cleaved and then clamped inside a fusion splicer, and the three dimensional controller of the splicer are adjusted to achieve a minimum alignment loss measured as -5.43 dB, showing that the whole alignment loss between two HC-PBF and SMF connections are -5.43dB which is used as a reference.

(3) Two cleaved fiber ends are taken out from the fusion splicer and inserted into the other two ferrules. Two ferrules are inserted into a ceramic sleeve at both ends and approach to each other gradually by the similar method as step (1). The alignment loss is measured to be -5.62 dB, showing that the additional loss induced by the misalignment

of the mechanical splicing is only ~ 0.2 dB. So we can adopt mechanical splicing for the cavity alignment in the following sections.

5.2.2.4 Fabrication of a resonating HC-PBF photonic microcell

As shown in Section 5.2.1, the resonating HC-PBF photonic microcell is formed by sandwiching a piece of HC-PBF between two dielectric mirrors made at the ends of two SMFs. The length of such a microcell can be from centimeters to meters, here the length of the HC-PBF is ~ 10 cm. The fabrication procedure of the microcell is illustrated in Figure 5.12:

(a) An cleaved SMF fiber is inserted and fixed to a standard fiber ferrule. The inner and outer diameter of the ferrule are $125 \mu\text{m}$ and 2.5 mm , respectively. This assembly is then end-polished and coated with a multilayer dielectric mirror with high reflectivity, for example $90\% \sim 99\%$ described in Section 5.2.2.1;

(b) Both ends of the HC-PBF are cleaved and inserted into other two ferrules carefully and fixed as an assembly with epoxy, and then both ends of the assembly are inspected for cleanness, as shown in Figure 5.12 (a);

(c) One ferrule with SMF mirror coated and one ferrule with HC-PBF are combined together by a mechanical splicer with an inner diameter of 2.5 mm , then two ferrules are aligned and holded together tightly. A small gap kept between the end-face of the HC-PBF and the mirrored end will facilitate gas filling into the hollow core. The ferrules with fibers and mechanical splicer are then fixed together with glue, as shown in Figure 5.12 (b) and (c);

(d) The other side of the HC-PBF in the fiber ferrule is similarly aligned to a SMF with a mirrored end, then the fabrication of the proposed HC-PBF Fabry-Perot cavity is finished, as shown in Figure 5.12 (d).

The length of HC-PBF microcell ranges from 5 to 10 cm, and longer cavity can also be made by this method.

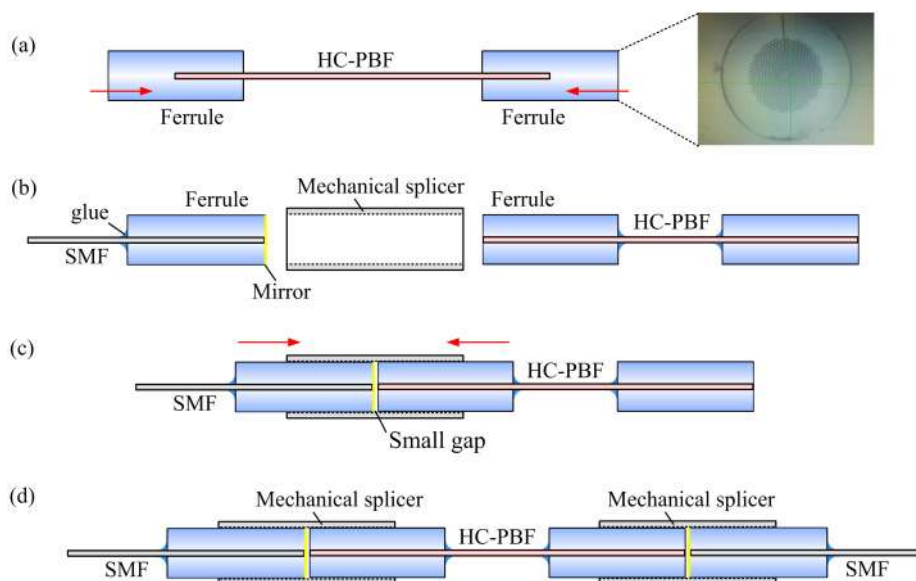


Fig. 5.12 Fabrication process of a resonating HC-PBF photonic microcell.

5.2.3 Characterization of a resonating HC-PBF photonic microcell

Characterization of a resonating HC-PBF photonic microcell can be described by the free spectral range (FSR)---the separation in frequencies/wavelengths between the two adjacent resonance peaks with $FSR=c/2nL$, n is the effective mode index of the HC-PBF and L the cavity length. For example, if a cavity length is 9.4 cm, the corresponding FSR would be 12.5 pm around 1532 nm. The full width at half maximum (FWHM) spectral width ($\delta\nu$) of the cavity resonances is also used for characterize the HC-PBF microcell, then the finesse of a cavity is described by $F=FSR/\delta\nu$ [1].

For the measurement of cavity transmission spectrum and finesse, the cavity length (or the laser wavelength) can be scanned periodically to couple the laser beam into the cavity. For a cavity length of 10 cm and a finesse of 100, the corresponding FSR is ~ 1.5 GHz or ~ 0.012 nm and the FWHM is calculated to be 0.12 pm. If the transmission

spectrum is measured by tuning the laser wavelength with a resolution of 0.1 pm of the ECDL, the transmission spectrum of the resonance will be undersampling. So here we measure the cavity transmission spectrum by modulating the cavity length.

The laser wavelength is fixed and we sweep the cavity length, so that the laser wavelength can couple into different cavity resonances one after the other in time. Figure 5.13 shows the sweeping process and the corresponding cavity transmissions. Figure 5.13 (a) shows the sweeping region indicated as the yellow region where two successive cavity resonances are swept across a fixed laser wavelength indicated as the red arrow. Figure 5.13 (b) depicts the cavity transmission in time when the cavity length is swept for two consecutive cycles. The different arrows indicate the alternating sweeping directions of the cavity length.

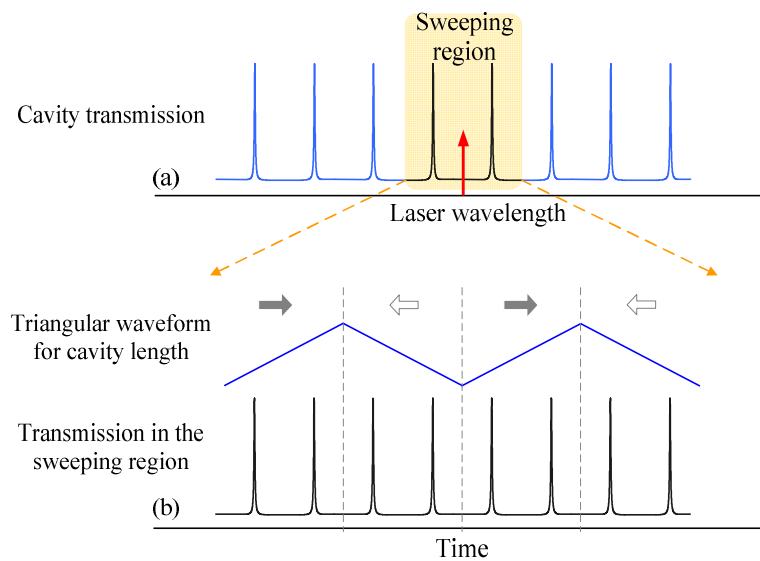
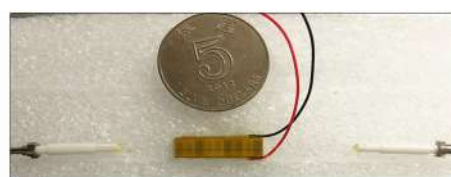


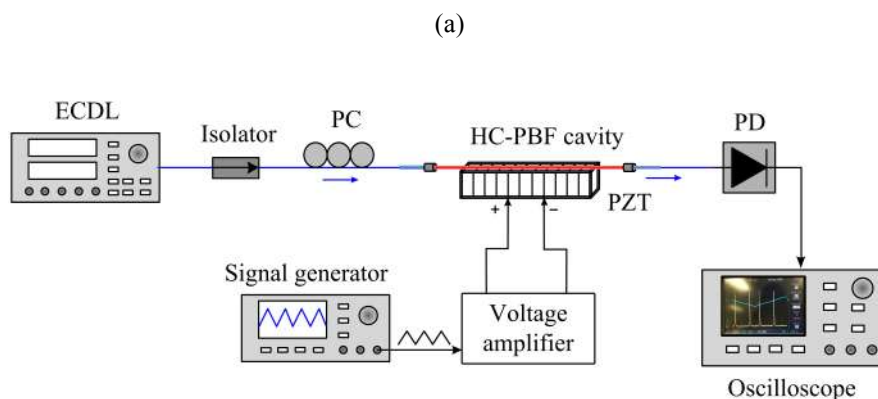
Fig. 5.13 Schematics showing (a) the two cavity resonances sweeping across a fixed laser wavelength and (b) the transmission of the cavity when the cavity length is swept periodically with a triangular wave.

Figure 5.14 shows the experimental setup for the transmission measurement of the microcell. The HC-PBF of the microcell is placed on a multilayer piezoelectric stack (PZT) and fixed with nail enamel shown in Figure 5.14 (a). Two SMF pigtails of the

cavity are connected to an external cavity diode laser (ECDL) and a photo-detector (PD), respectively. Laser wavelength is fixed while the cavity length is swept by the PZT by a triangular voltage with magnitude of ~ 10.5 V and frequency of 1 Hz by a signal generator. The cavity transmission spectrum can be recorded by a digital oscilloscope. Sweeping the cavity length allows the observation of the cavity transmission spectrum, as shown in Figure 5.14 (b).



(a)



(b)

Fig. 5.14 (a) A photo of the HC-PBF microcell fixed on the PZT. (b) Experimental setup for transmission measurement of the microcell.

The transmission spectrums of two HC-PBF microcells are shown in Figures 5.15 (a) and (b). The cavity length of these two gas cells are 9.4 and 6.75 cm, respectively. For the cavity length of 9.4 cm in Figure 5.15 (a), the laser wavelength is fixed to ~ 1532.8 nm, and the cavity finesse is calculated to be 68. Similarly, for the cavity length of 6.75 cm in Figure 5.15 (b), the laser wavelength is fixed to ~ 1530.3 nm, and the finesse is calculated to be 128.

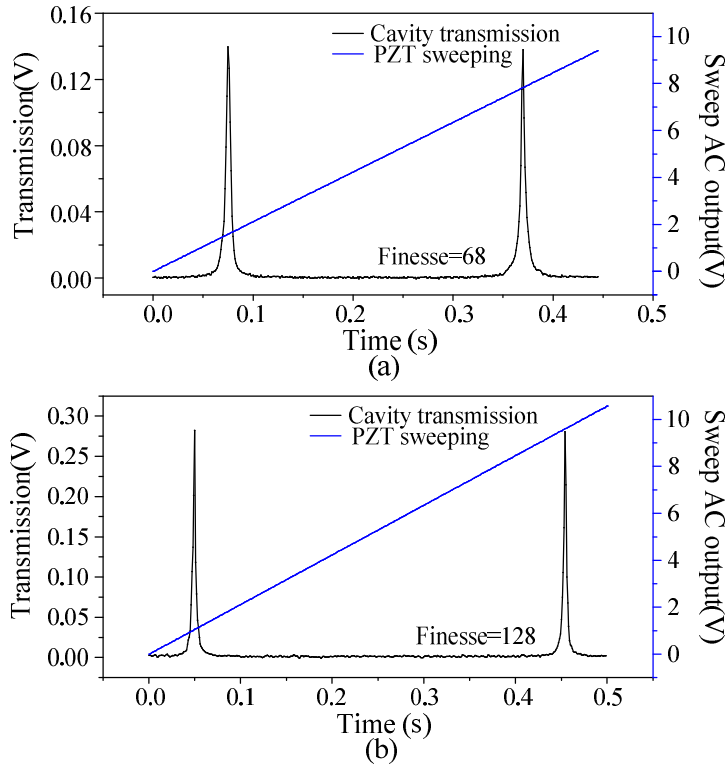
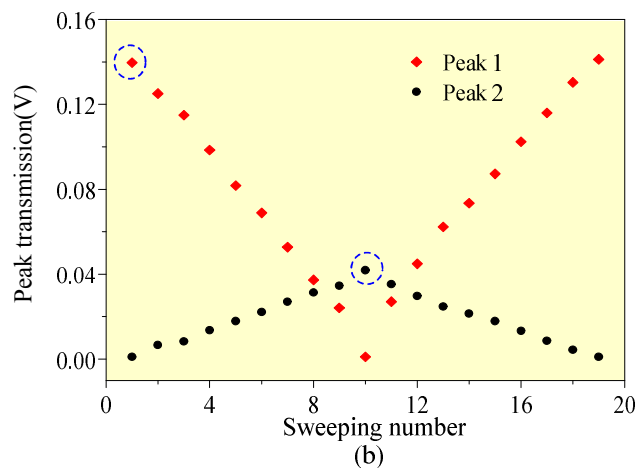
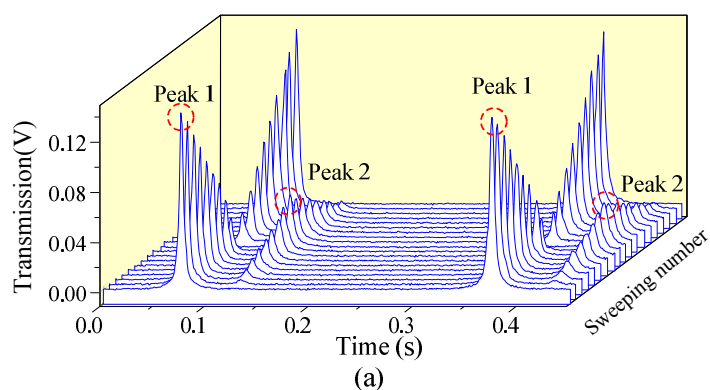


Fig. 5.15 Measured transmission spectrums of HC-PBF microcells with cavity length of (a) 9.4 cm and (b) 6.75 cm.

During the transmission measurement, the transmission spectrums are found to be polarization dependent and can be tuned by the polarization controller (PC) shown in Figure 5.16 (a). This may be due to the residual birefringence of the HC-PBF which has been observed previously [2, 3]. For the cavity with length of 9.4 cm, the transmission spectrums are recorded by tuning the PC continuously and the results are shown in Figure 5.16 (a). We can see that two resonances are shown within one FSR. The resonance peak indicated as “Peak 1” is strongest while the other resonance “Peak 2” disappears, and vice versa. For a clearer demodulation, the peak values of the two resonances in Fig. 5.16 (a) are indicated in Figure 5.16 (b) as red squares and black dots, respectively. Two sets of resonant peaks represent two polarization eigenstates of the HC-PBF and are orthogonal to each other. The transmission spectrums of the cavity are shown in Figure 5.16 (c) when the orientation of the incident light is on one of the

polarization eigenstates of the HC-PBF. The magnitude of Peak 1 is ~ 3.5 times higher than that of Peak 2, so two eigenstates suffer from different losses. The finesses for the two polarization states are measured to be 68 and 38, respectively. From Fig. 5.16 (c), the phase difference $\Delta\delta$ between the two polarization eigenstates is calculated to be $2\pi \times (51/297) = 1.079 \text{ rad}$ at $\lambda \sim 1532.8 \text{ nm}$. So the residual birefringence of the HC-PBF (Δn) is calculated to be [4]

$$\Delta n = \frac{\lambda \cdot \Delta\delta}{4\pi L} = 1.4 \times 10^{-6} \quad (5.1)$$



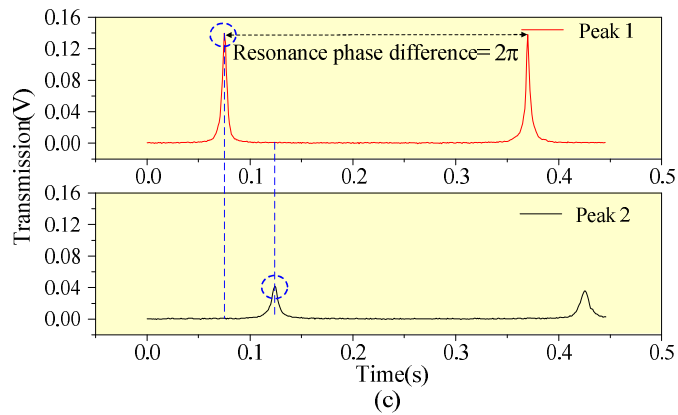


Fig. 5.16 (a) Transmission spectrums of the proposed cavity when the PC is adjusted continuously. (b) Peak values for Peaks 1 and 2 in (a). (c) Transmission spectrums when the polarization is on one of the eigenstates.

5.3 Summary

In this chapter, a novel resonating HC-PBF photonic microcell made by jointing a piece of HC-PBF with two SMFs with mirrored end is introduced. We first introduce the construction and fabrication of the HC-PBF microcell, then we present the characterization of the microcell including the measurement of its transmission and finesse. The resonating HC-PBF microcells with length from 5 to 10 cm can achieve cavity finesses from 50 to well over 100.

References of Chapter 5

- [1] G. Gagliardi and H.-P. Loock, *Cavity-Enhanced Spectroscopy and Sensing* (Springer, 2014).
- [2] X. Chen, M.-J. Li, N. Venkataraman, M. Gallagher, W. Wood, A. Crowley, J. Carberry, L. Zenteno, and K. Koch, "Highly birefringent hollow-core photonic bandgap fiber," *Opt. Express* 12, 3888-3893 (2004).
- [3] M. Wegmuller, M. Legré, N. Gisin, T. Hansen, C. Jakobsen, and J. Broeng, "Experimental investigation of the polarization properties of a hollow core photonic bandgap fiber for 1550 nm," *Opt. Express* 13, 1457-1467 (2005).

- [4] H. Chen, "Optical microwave and millimeter generation by using birefringent fiber FP cavity with pulse laser injection," *J. Infrared Milli. Waves* 28, 979-986 (2007).

Chapter 6

Resonating HC-PBF microcell DAS gas sensor

6.1 Introduction

Compared with the single pass SMF/HC-PBF/SMF absorption cell with long diffusion time, the resonating hollow-core fiber (HC-PBF) photonic microcell can achieve high sensitivity and fast response simultaneously. Such a cavity would enhance the effective absorption pathlength by a factor proportional to the cavity finesse. At the same time the fast response can be maintained by the use of a shorter length of HC-PBF. Moreover, the reduced cavity volume also minimizes the consumption of gas sample.

This chapter will introduce a resonating HC-PBF photonic microcell for high performance gas detection based on direct absorption spectroscopy (DAS). By using this resonating HC-PBF photonic microcell, the effective absorption path length can be enhanced by a factor proportional to the cavity finesse. The construction of this microcell has been described in Chapter 5. In this chapter, the gas detection experiments with a resonating HC-PBF photonic microcell based on DAS will be introduced.

6.2 Cavity enhancement of a resonating HC-PBF microcell for gas absorption

The basics of cavity enhancement with a resonating HC-PBF photonic microcell as gas absorption cell may be explained with the aid of Figure 6.1. We first consider an empty resonating HC-PBF microcell made by two identical mirrors with distance of L , so the transmission coefficients are $t_1=t_2=t$ and losses of the mirrors are $l_1=l_2=l$, and the round-trip cavity loss is then $L_{\text{cav}}=2(t+l)$, so the cavity finesse F may be expressed as [1, 2]

$$F = \frac{2\pi}{t_1 + l_1 + t_2 + l_2} = \frac{\pi}{t+l} \quad (6.1)$$

The resonant reflection R and transmission T of the microcell may be expressed respectively as [2]

$$R = \frac{P_r}{P_{in}} = \left(\frac{l}{t+l}\right)^2 \quad (6.2)$$

$$T = \frac{P_t}{P_{in}} = \left(\frac{t}{t+l}\right)^2 \quad (6.3)$$

where P_{in} , P_r and P_t represent input power, reflected power and transmitted power through the cavity, respectively.

When the microcell is filled with a weakly absorbing gas, a laser beam enters the microcell and travels back and forth (round-trip) many times inside the cell. Assuming that the gas absorption coefficient and concentration are respectively α and C , under the condition of $\alpha CL \ll t+l$, the resonant transmission as given in Eq. (6.3) may be re-written as

$$\begin{aligned} T' = \frac{P'_t}{P_m} &= \left(\frac{t}{t+l+\alpha CL}\right)^2 = \left[\frac{t(t+l-\alpha CL)}{(t+l+\alpha CL)(t+l-\alpha CL)}\right]^2 = \left[\frac{t(t+l-\alpha CL)}{(t+l)^2 - (\alpha CL)^2}\right]^2 \approx \left[\frac{t(t+l-\alpha CL)}{(t+l)^2}\right]^2 \\ &= \frac{t^2[(t+l)^2 - 2(t+l)\alpha CL + (\alpha CL)^2]}{(t+l)^4} \approx \left(\frac{t}{t+l}\right)^2 \left(1 - \frac{2\alpha CL}{t+l}\right) \end{aligned} \quad (6.4)$$

The absorption-induced relative change in the transmitted light signal through the microcell may be related to gas concentration by

$$S_{absorption} = \frac{P_t - P'_t}{P_t} = \frac{2\alpha CL}{t+l} = \frac{2F}{\pi} \cdot \alpha CL \quad (6.5)$$

Comparing this with a single-path non-resonating gas cell of the same length L , the use of a F-P cavity with finesse F enhances the signal change by a factor of $2F/\pi$, giving an

effective absorption path length of $(2F/\pi)L$. For example, if the cavity length L is 10 cm and finesse is 10^4 , the effective absorption path length becomes 640 m, indicating that an extremely long effective path length and hence high detection sensitivity could be obtained by use of a high finesse cavity.

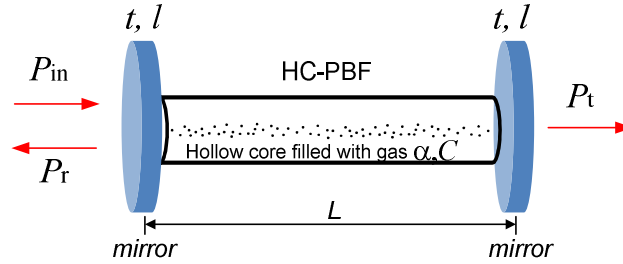


Fig. 6.1 Basics of cavity enhancement with a resonating HC-PBF photonic microcell for gas absorption. P_{in} , P_r and P_t denote respectively the cavity input, reflected and transmitted light powers.

6.3 Gas detection experiments based on direct absorption

6.3.1 Experimental setup

Figure 6.2 shows the experimental setup for gas detection based on DAS. The cavity length of the microcell is 9.4 cm and the FSR is 12.5 pm (1.6 GHz). The cavity finesse is measured to be 68. The P(13) absorption line of acetylene located in 1532.83 nm is used, and the linewidth of this line is ~ 40 pm (5.11 GHz) covering approximately ~ 3.2 FSR of the cavity, as shown in Figure 6.3 (a). The laser source used here is a distributed feedback (DFB) laser with its wavelength tuned to 1532.83 nm for the P(13) absorption line of acetylene. The laser wavelength can be scanned by thermal tuning via a temperature controller and modulated at a higher frequency via modulation of the current by laser controller simultaneously. The HC-PBF of the microcell is mounted on a multilayer piezoelectric stack (PZT) as mentioned in Chapter 5.2.3, and the PZT is used to tune the cavity length by applying a DC voltage so that one of the cavity resonances can be made to align to the target gas absorption line center. The cavity transmission is

detected by a photo-detector (PD). The output of PD is connected to a lock-in amplifier (Stanford research systems, SR830) at its second harmonic frequency.

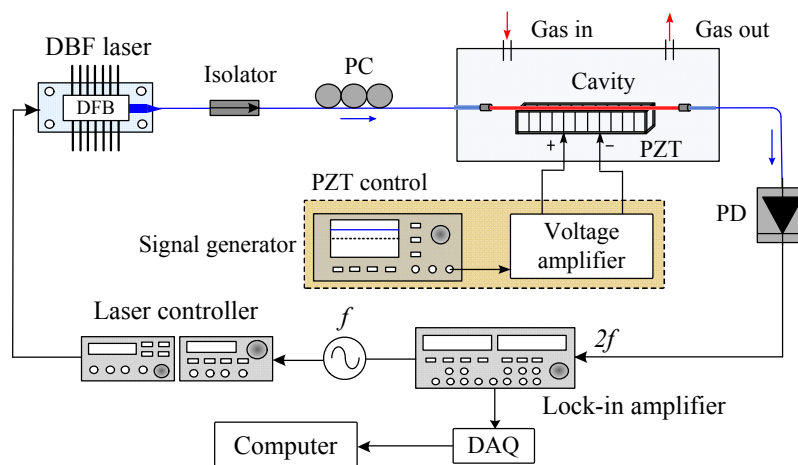


Fig. 6.2 Experimental setup for gas detection with the proposed resonating HC-PBF microcell.

Before gas detection experiments, a DC voltage is applied to the PZT stack to scan the cavity length, so that one of the cavity resonances can be made to align to the gas absorption line center. The procedure is as follows, as shown in Figure 6.3:

(1) The laser wavelength is firstly tuned to around the P(13) line and the cavity resonances near the absorption line can be observed by scanning the laser wavelength. The cavity resonances are typically not at the center of the absorption line but with a proper voltage of applied to the PZT (say ~ 3.5 V), one of the resonances can be made to align to the center of the line at 1532.83 nm, indicated as Resonant A in Figure 6.3 (a). This cavity resonance will be used for the gas detection experiment in the next step.

(2) As mentioned previously, the linewidth of P(13) line of acetylene is ~ 40 pm (5.11 GHz) which covers approximately 3.2 FSR of the cavity with length of 9.4 cm, as indicated in Figure 6.3 (a). So it may not be appropriate to operate the DFB laser at the adjacent cavity resonance of the absorption line center as a non-absorption reference. Therefore, the DFB laser can be adjusted to another cavity resonance indicated as

Resonance B at 1532.95 nm away from the gas absorption as a non-absorption reference, and the experiments are repeated with this resonance and compared with the results of Resonance A.

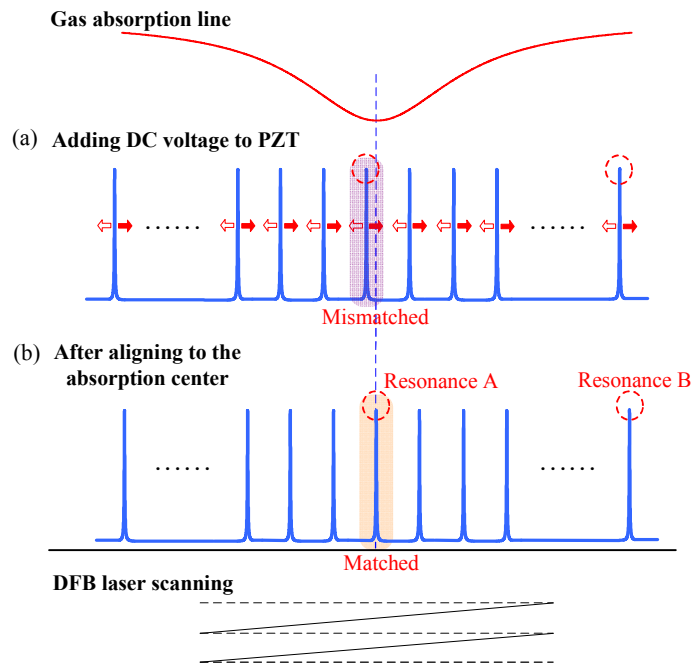


Fig. 6.3 Aligning process of a cavity resonance to the gas absorption line center. (a) Cavity resonances are not tuned to the absorption line center, (b) one of the resonances (Resonance A) is aligned to the center of an absorption line. Resonance B is away from the gas absorption line center. The wavelength of the DFB laser is tuned across to observe the resonances.

When the gas sample filling into the resonating microcell, the cavity resonance would shift slightly due to variation in gas composition and the environmental temperature. Then the voltage applied to the PZT will need to be fine-tuned to re-aligned the cavity resonance to the gas absorption line center.

The acetylene detection experiment was conducted with wavelength modulation spectroscopy and lock-in detection. The DFB laser wavelength was scanned across the Resonance A and it was modulated sinusoidally at frequency of 22.1 kHz with amplitude of 4 mV simultaneously. During the scanning, a lock-in amplifier is used to record the

second-harmonic of the modulation signal at 44.2 kHz. The laser power into the absorption cell was ~ 1.63 mW and acetylene concentration was ~ 550 p.p.m.. The time constant of the lock-in amplifier is 300 ms with a filter slope of 18 dB/Oct. All the experiments were carried out at atmospheric pressure and room temperature. The experiment was repeated for Resonance B, which is away from the gas absorption line.

6.3.2 Gas detection results

The second harmonic lock-in outputs when the laser wavelength was scanned across Resonance A and Resonance B are shown in Figures 6.4 (a) and (b), respectively. The black lines indicate the cavity filled with air while the red lines indicate the cavity filled with 550 p.p.m. acetylene balanced by nitrogen. In Figure 6.4 (a) for Resonance A, the signal variation due to gas absorption is 1.47 mV, corresponding to an absorbance of $1.47 \text{ mV}/6.84 \text{ mV}=21.5\%$. In Figure 6.4 (b) for Resonance B, we can see that the signal variation is negligible.

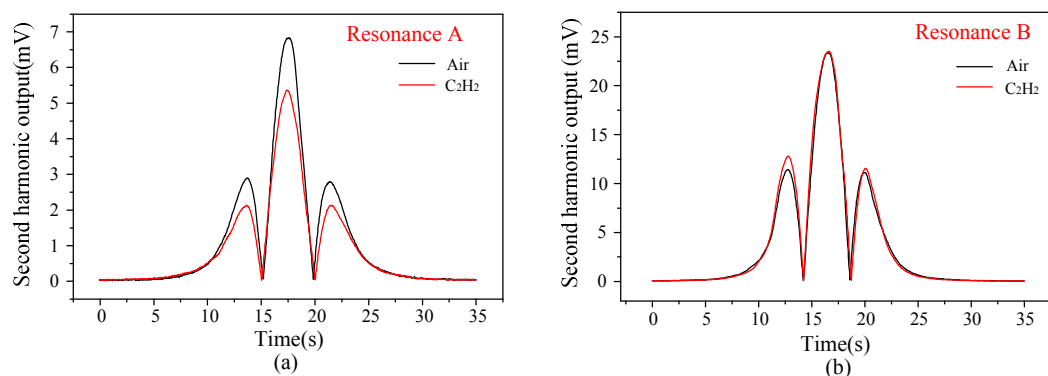


Fig. 6.4 Experimental results. (a) Second harmonic lock-in output signals when laser is scanned across a resonance at the gas absorption line center at 1,532.83 nm indicated as Resonance A. (b) Second harmonic lock-in output signals when laser is tuned across a F-P resonance away from gas absorption line center at 1,532.95 nm indicated as Resonance B. The black and red curves are respectively for the cavity filled with air and 550 p.p.m. acetylene balanced by nitrogen.

Experiments were repeated for different gas concentration of 357 p.p.m.

The second harmonic lock-in outputs when the laser wavelength was scanned across Resonance A and Resonance B are shown in Figures 6.5 (a) and (b), respectively. The black lines indicate the cavity filled with air while the red lines indicate the cavity filled with 357 p.p.m. acetylene balanced by nitrogen. In Figure 6.5 (a) for Resonance A, the signal variation due to gas absorption is 0.64 mV, corresponding to an absorbance of $0.64 \text{ mV}/5.69 \text{ mV}=11.32\%$. In Figure 6.5 (b) for Resonance B, we can see that the signal variation is negligible.

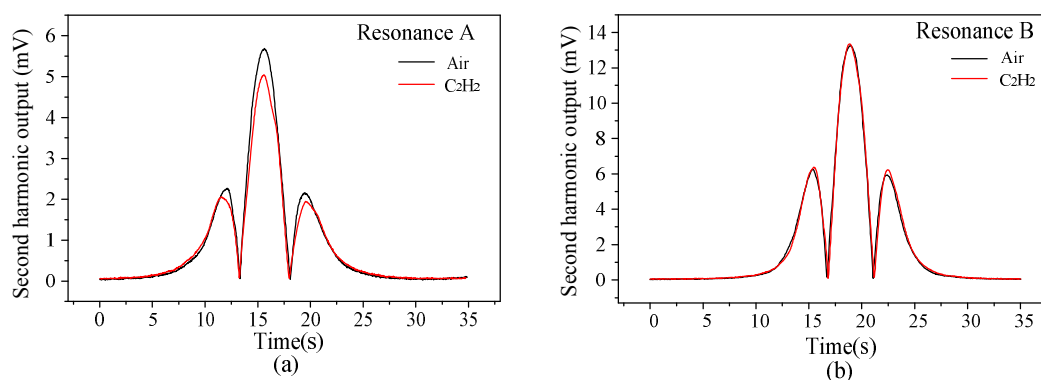


Fig. 6.5 Experimental results. (a) Second harmonic lock-in output signals when laser is tuned across a Fabry-Perot resonance at the gas absorption line center at 1,532.83 nm indicated as Resonance A. (b) Second harmonic lock-in output signals when laser is tuned across a Fabry-Perot resonance away from the gas absorption line center at 1532.89 nm indicated as Resonance B. The black and red curves are respectively for the cavity filled with air and 357 p.p.m. acetylene balanced by nitrogen.

Experiments were repeated for different gas concentration of 725 p.p.m.

The second harmonic lock-in outputs when the laser wavelength was scanned across Resonance A and Resonance B are shown in Figures 6.6 (a) and (b), respectively. The black lines indicate the cavity filled with air while the red lines indicate the cavity filled with 725 p.p.m. acetylene balanced by nitrogen. In Figure 6.6 (a) for Resonance A, the signal variation due to gas absorption is 2.85 mV, corresponding to an absorbance of $2.85 \text{ mV}/10.29 \text{ mV}=27.7\%$. In Figure 6.6 (a) for Resonance B, we can see that the signal variation is negligible.

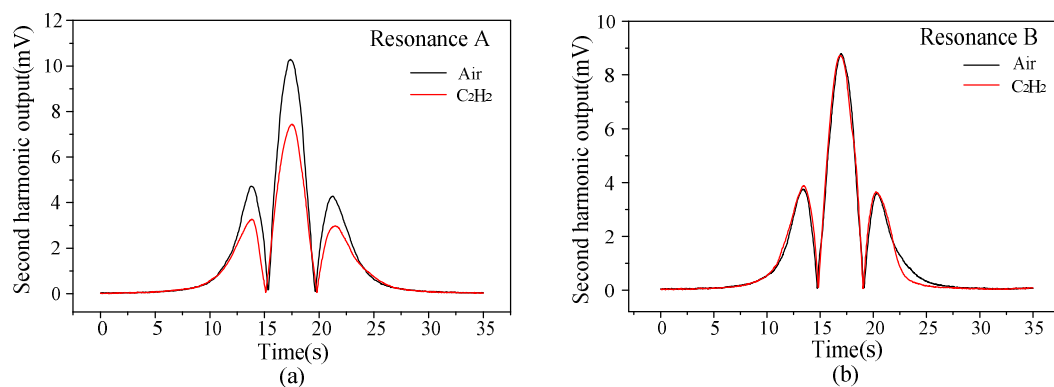


Fig. 6.6 Experimental results. (a) Second harmonic lock-in output signals when laser is tuned across a F-P resonance at the gas absorption line center at 1,532.83 nm indicated as Resonance A. (b) Second harmonic lock-in output signals when laser is tuned across a Fabry-Perot resonance away from the gas absorption line center at 1532.88 nm indicated as Resonance B. The black and red curves are respectively for the cavity filled with air and 725 p.p.m. acetylene balanced by nitrogen.

Figure 6.7 shows the absorption signal (%) as function of gas concentration. Curve fitting shows that it has a linear relationship ($r^2=0.9846$) with a slope of 0.039% per p.p.m.. According to the HITRAN 2004 database, the equivalent absorption length of the cavity is determined to be ~ 378 cm [3]. So the enhancement factor of $2F/\pi=40$ or a finesse of $F=62$, indicating an agreement with the measured value of 68 in Chapter 5.2.3.

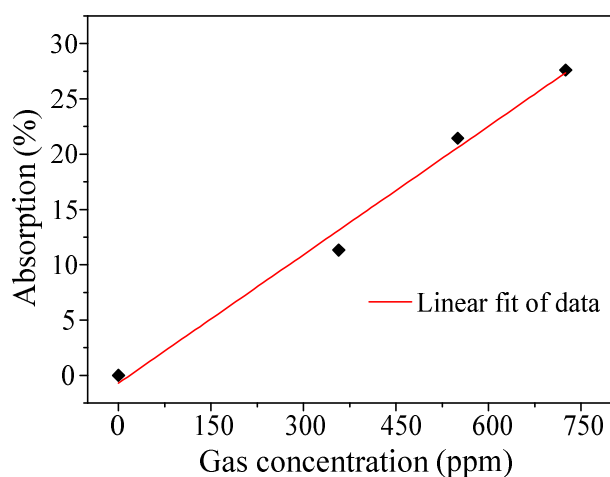


Fig. 6.7 Absorption signal as function of gas concentration.

The fluctuation of second harmonic peak signal are evaluated by repeatedly scanning the resonance at 1532.83 nm over a period of 8 min. The gas cell is filled with air. As shown in Figure 6.8, the standard deviation (s.d.) of fluctuation is 18.8 μV . So the signal to noise ratio (SNR) of $1.47 \text{ mV}/0.0188\text{mV}=78$ when the cavity is filled with 550 p.p.m. acetylene corresponding to an error in the gas concentration measurement of 7 p.p.m. for a SNR of unity, or an equivalent absorption-coefficient (NEA) of $7.35 \times 10^{-6} \text{ cm}^{-1}$. The time constant of the lock-in amplifier is 1s with a filter slope of 18dB Oct⁻¹.

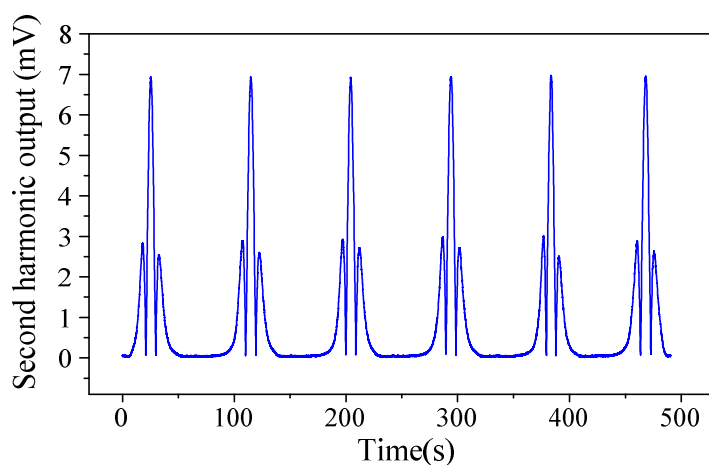


Fig. 6.8 Second harmonic lock-in output when the DFB laser wavelength is swept across the resonance at 1532.83 nm for ~500 s duration.

6.3.3 Comparison with a single-path non-resonating HC-PBF gas cell

An experiment with a non-resonating HC-PBF cell (single-path, without mirrors) with fiber length of 10.8 cm is also conducted to compare with the performance of the resonating HC-PBF microcell. The cell is made by fusion splicing one end of the HC-PBF to a cleaved SMF while the other end is butt-coupled to another cleaved SMF by use of an Ericsson FSU-975 fusion splicer. Figure 6.9 (a) shows the experimental setup for transmission measurement of the cell. The ECDL and PD are embedded in an

Agilent 81910A Photonic All-Parameter Analyzer. The wavelength of the ECDL is tuned from 1525 to 1535 nm with a resolution of 1 pm.

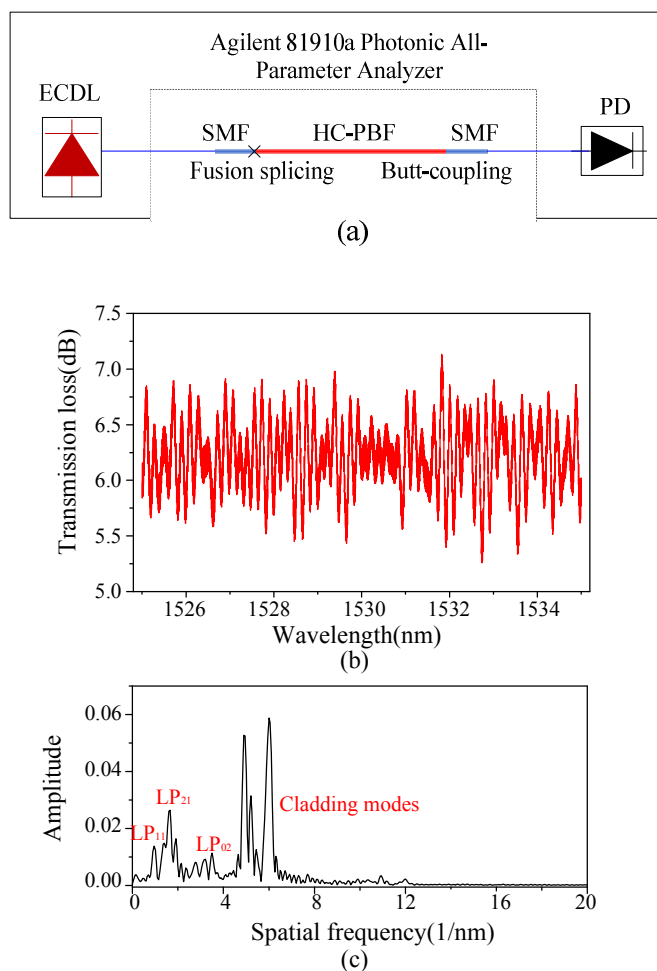


Fig. 6.9 (a) Experimental setup for measuring the transmission spectrum of a single-path cell. (b) Measured transmission spectrum of the HC-PBF cell. (c) Fourier transform of the spectrum in (b).

Figures 6.9 (b) and (c) show the measured transmission spectrum and its Fourier transform of the single-path HC-PBF cell. The quasi-periodic spectrum is observed and it may be due to interference between the fundamental core mode and different groups of higher order modes, which are labeled in the inset of Figure 6.9 (c). The performance of HC-PBF based sensors is typically limited by this modal interference (MI) which exists in current commercial HC-PBFs and leads to intensity fluctuation of the transmitted light [4-7]. Using HC-PBF longer than 10 m would reduce the MI considerably.

However for the investigation of short fiber sample here, the intensity fluctuation is large, resulting in large error in gas concentration measurement. Compared with a 7-cm long HC-PCF single-path gas cell which shows a NEC of 647 p.p.m. methane [8], or $1.63 \times 10^{-4} \text{ cm}^{-1}$ in NEA, the performance with a high finesse resonating HC-PBF photonic microcell is much better. This may be due to the effect of MI on gas detection, which is found being reduced significantly since the higher order modes suffer much larger loss after traveling many times within the high finesse cavity.

6.4 Summary

In this chapter, a resonating HC-PBF photonic microcell for high sensitivity gas detection based on DAS is introduced. Comparing with the single-path (without mirrors) HC-PBF gas cells of a similar length, a high finesse resonating HC-PBF microcell reduces significantly the effect of MI noise on gas detection. With a cavity length of 9.4 cm and finesse of 68, we demonstrated acetylene detection with a detection limit of ~ 7 p.p.m, 1-2 orders of magnitude better than a single-path HC-PBF sensor with a similar length [8] and comparable with that of a 13-m-long HC-PBF sensor [5].

References of Chapter 6

- [1] R. Van Zee and J. P. Looney, *Cavity-enhanced spectroscopies* (Academic Press, 2003).
- [2] L. S. Ma, J. Ye, P. Dubé, and J. L. Hall, "Ultrasensitive frequency-modulation spectroscopy enhanced by a high-finesse optical cavity: theory and application to overtone transitions of C_2H_2 and C_2HD ," *J. Opt. Soc. Am. B* 16, 2255-2268 (1999).
- [3] L. S. Rothman, D. Jacquemart, A. Barbe, D. C. Benner, M. Birk, L. Brown, et al., "The HITRAN 2004 molecular spectroscopic database," *J. Quant. Spectrosc. Radiat. Transfer.* 96, 139-204 (2005).
- [4] W. Jin, H. L. Ho, Y. C. Cao, J. Ju, and L. F. Qi, "Gas detection with micro- and nano-engineered optical fibers," *Opt. Fiber Technol.* 19, 741-759 (2013).

- [5] F. Yang, W. Jin, Y. Cao, H. L. Ho, and Y. Wang, "Towards high sensitivity gas detection with hollow-core photonic bandgap fibers," *Opt. Express* 22, 24894-24907 (2014).
- [6] J. Parry, B. Griffiths, N. Gayraud, E. McNaghten, A. Parkes, W. MacPherson, and D. Hand, "Towards practical gas sensing with micro-structured fibres," *Meas.Sci. Technol.* 20, 075301 (2009).
- [7] M. N. Petrovich, F. Poletti, and D. J. Richardson, "Analysis of modal interference in photonic bandgap fibres," 12th International Conference on Transparent Optical Networks (2010), pp. 1-4.
- [8] Y. Hoo, S. Liu, H. L. Ho, and W. Jin, "Fast response microstructured optical fiber methane sensor with multiple side-openings," *IEEE Photonics Technol. Lett* 22, 296-298 (2010).

Chapter 7

Resonating HC-PBF photonic microcell PT gas sensor

7.1 Introduction

This chapter will introduce a resonating hollow-core fiber (HC-PBF) photonic microcell for high performance gas detection based on photothermal (PT) spectroscopy. The cavity enhancement of such a resonating HC-PBF photonic microcell can simultaneously amplify the intracavity build-up intensity for the pump beam inside the HC-PBF and improve the slope of the operating point for the probe beam by a factor proportional to the cavity finesse. In this chapter, the cavity enhanced PT gas experiments using resonating HC-PBF photonic microcell will be introduced.

7.2 Basics of cavity-enhanced PT spectroscopy with a resonating HC-PBF microcell

The basics of cavity enhancement with a resonating HC-PBF photonic microcell as absorption cell may be explained with the aid of Figure 7.1(a). We first consider an empty resonating microcell made by sandwiching a short length of HC-PBF between two identical reflective mirrors. The transmission, reflection coefficient and the loss of the mirrors are denoted as t , r and l , with relationship of $t+r+l=1$. The cavity finesse F and the on-resonance cavity transmission T_{res} may be expressed as [1-3]:

$$F = \frac{\pi}{t+l} = \frac{\pi}{1-r} \quad (7.1)$$

$$T_{res} = \frac{t^2}{(1-r)^2} \quad (7.2)$$

then transmission coefficient t can be calculated as $t = \sqrt{T_{res}(1-r)^2}$. The enhancement factor E of the intracavity build-up intensity may be expressed by Eq. (7.1) as [1-3]:

$$E = \frac{I_c}{I_{in}} = t \left(\frac{1}{1-r} \right)^2 = t \left(\frac{F}{\pi} \right)^2 \quad (7.3)$$

where I_{in} and I_c represent the input intensity and the intracavity build-up intensity, respectively. Comparing this with a single-path non-resonating cell of the same length L , the use of a resonating microcell with finesse F enhances the intracavity build-up intensity by a factor of E . For example, if cavity finesse is 1000 and the on-resonance cavity transmission T_{res} is 0.95, the enhancement factor E is calculated to be 310. When the input power is 1 mW, then intracavity build-up power becomes 310 mW, which would be a huge enhancement for the intracavity intensity by use of a resonating HC-PBF photonic microcell.

The basic process of double-cavity-enhanced PT spectroscopy in a resonating HC-PBF photonic microcell filled with a weakly absorbing gas may be explained by Figure 7.1 (b). When a wavelength modulated pump light beam with its wavelength tuned to an absorption line of the target gas is coupled to one cavity resonance which is aligned to the center of the gas absorption line, it interacts with the target gas and the gas molecules will be excited to a higher energy state and then return to their initial state via molecular collision. This process is accompanied by periodic heat production, which modulates the local temperature, density and pressure, and hence the refractive index of the gas [4]. When a probe light beam is propagating along the same resonating HC-PBF microcell, the accumulated phase of the fundamental optical mode of the probe will be modulated, which can be detected by a HC-PBF F-P interferometry (FPI). For the pump beam, since the intracavity build-up intensity would be enhanced by a factor of E , the PT signal would be amplified. For the probe beam which is operating at the highest slope

point of a different cavity resonance where the gas absorption is minimal, the slope of the cavity resonance is proportional to the cavity finesse F , so the PT signal would also be amplified by this resonating microcell.

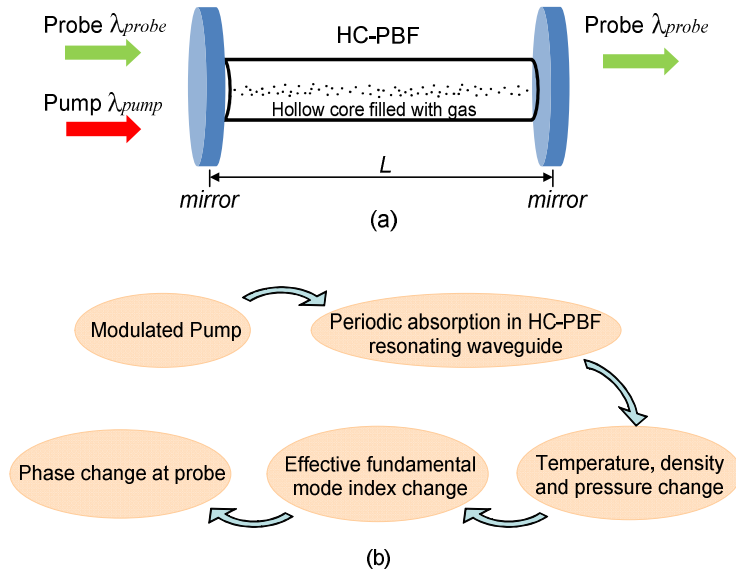


Fig. 7.1 Basics of cavity-enhanced PT spectroscopy. (a) Sketch of a resonating HC-PBF photonic microcell.

(b) Basic processes involved in producing phase modulation in a resonating HC-PBF photonic microcell.

7.3 Cavity-enhanced PT gas experiments with a resonating HC-PBF photonic microcell

7.3.1 Experimental setup

The fabrication process of a resonating HC-PBF photonic microcell and experimental setup for its transmission measurement have been described in Chapter 5, which will not be described in details here.

Figures 7.2 (a) and (b) show the measured transmission spectrums in different wavelength of a resonating HC-PBF photonic microcell with length of 6.2 cm. In Figure 7.2 (a), the laser wavelength is fixed to ~ 1532.8 nm, and the cavity finesse is measured to be 45. Similarly, in Figure 7.2 (b), the laser wavelength is fixed to ~ 1550.02 nm, and

the finesse is measured to be 41. These two wavelengths will be used for the photothermal gas experiments in this section.

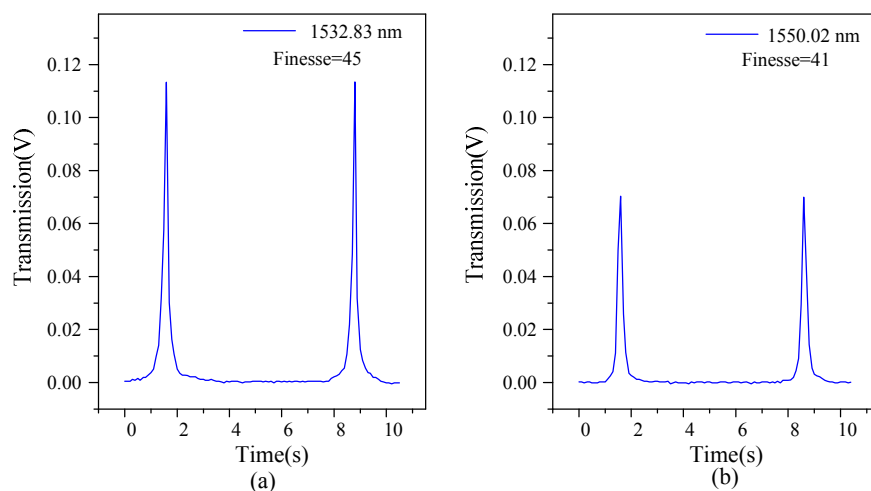


Fig. 7.2 Measured transmission spectrums of a resonating HC-PBF photonic microcell at wavelength of (a) 1532.83 nm and (b) 1550.02 nm.

Figure 7.3 shows the basic process for cavity-enhanced photothermal gas experiments with a resonating HC-PBF photonic microcell. The cavity length of the resonating microcell is 6.2 cm and the FSR is ~ 19 pm (2.43 GHz). The absorption line used is the P(13) line of acetylene centered at 1532.83 nm, and the linewidth of this line is ~ 40 pm (5.11 GHz) which covers approximately 2.1 FSR of the HC-PBF Fabry-Perot, as indicated in Figure 7.3. The pump wavelength is scanned slowly across the whole gas absorption line and the corresponding cavity resonances. When the pump wavelength is tuned to the cavity resonance which is aligned to the center of the gas absorption line, indicated as Resonance A, the absorption of the modulated pump results in phase modulation of the probe beam via PT effect within the cavity. Meanwhile, the wavelength of the probe beam is operating at a maximum slope point of a different cavity resonance where the absorption of acetylene is minimal, indicated as Resonant B in Figure 7.3. At the Fabry-Perot output, the phase modulation is converted to intensity modulation and is further detected by a lock-in amplifier.

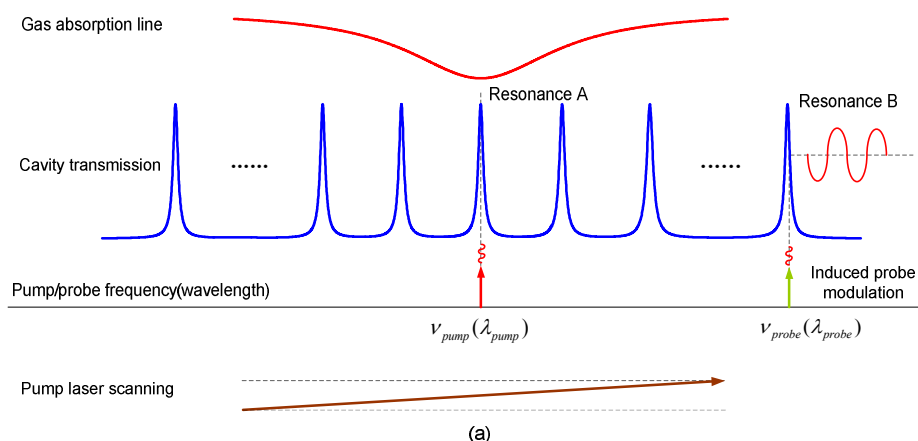


Fig. 7.3 Basic process for cavity-enhanced photothermal gas experiments. The pump laser is tuned to a cavity resonance (Resonance A) which is aligned to the center of the gas absorption line, while the probe laser is tuned to the highest slope point of another cavity resonance (Resonance B) which is away from the center of the gas absorption line.

Figure 7.4 shows the the pump-probe experimental setup for the cavity-enhanced photothermal gas experiments. A distributed feedback (DFB) semiconductor laser is used as the pump laser source (λ_{pump}) and its wavelength is slowly tuned across the P(13) absorption line of acetylene (C_2H_2) centered at 1532.830 nm. The laser nominal wavelength can be changed by thermal tuning via a temperature controller and can be modulated at a higher frequency of 22.4 kHz with amplitude of 10 mV via modulation of the current simultaneously. The modulated pump light is absorbed by gas sample and the heating of the gas sample will modulate the phase of the probe beam. An ECDL with output power of ~ 3 mW is used as the probe beam. The wavelength of the probe laser (λ_{probe}) is tuned to 1550.2 nm, corresponding to steepest slope of the cavity resonance, which produces the largest change in output intensity for a given phase modulation induced by PT effect. The transmitted probe light from the cavity was detected by a PD. The output from the PD is demodulated by a lock-in amplifier (Stanford research systems, SR830) at its second harmonic frequency (i.e., 44.8 kHz). The pump power used is 116.7 mW and the acetylene concentration in the gas cell is 100 parts-per-million

(ppm). The time constant of the lock-in amplifier is set to 3 s with a filter slope of 18 dB Oct⁻¹. During this process, the operating point of the probe laser wavelength is maintained from the DC component of the transmitted output of the Fabry-Perot shown in the oscilloscope.

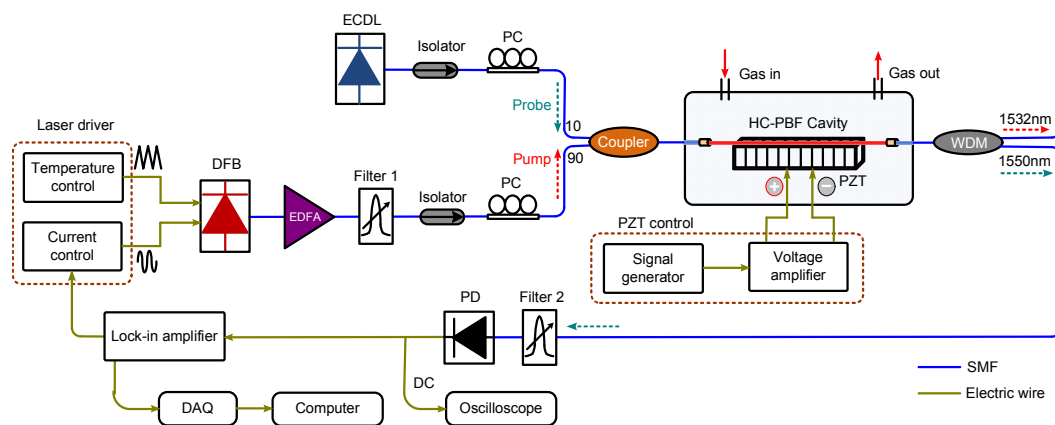


Fig. 7.4 Experimental setup of the PT gas detection with a resonating HC-PBF photonic microcell. Blue line, optical fiber; greenline, electrical cable; ECDL, external cavity diode laser; DFB, distributed feedback laser; PC, polarization controller; PZT, piezoelectric stack; WDM, wavelength division multiplexer; PD, photo-detector; DAQ, data acquisition

7.3.2 Experimental results for gas detection

7.3.2.1 Test of lower detection limit

Figure 7.5 shows the second harmonic lock-in output when the pump wavelength was tuned across the P(13) line of acetylene and the corresponding cavity resonances. Figure 7.5 (a) shows second harmonic signal when the gas cell is filled with 100 ppm acetylene balanced by nitrogen. The second harmonic signal becomes maximal near the gas absorption line center at 1532.83 nm and becomes minimal away from the gas absorption line. Figure 7.5 (b) shows second harmonic output when the gas cell is filled with nitrogen, showing that the signal becomes minimal. From Figure 7.5, we can see

that there exists a small background thermal signal which may be induced by the absorption of the dielectric mirror materials.

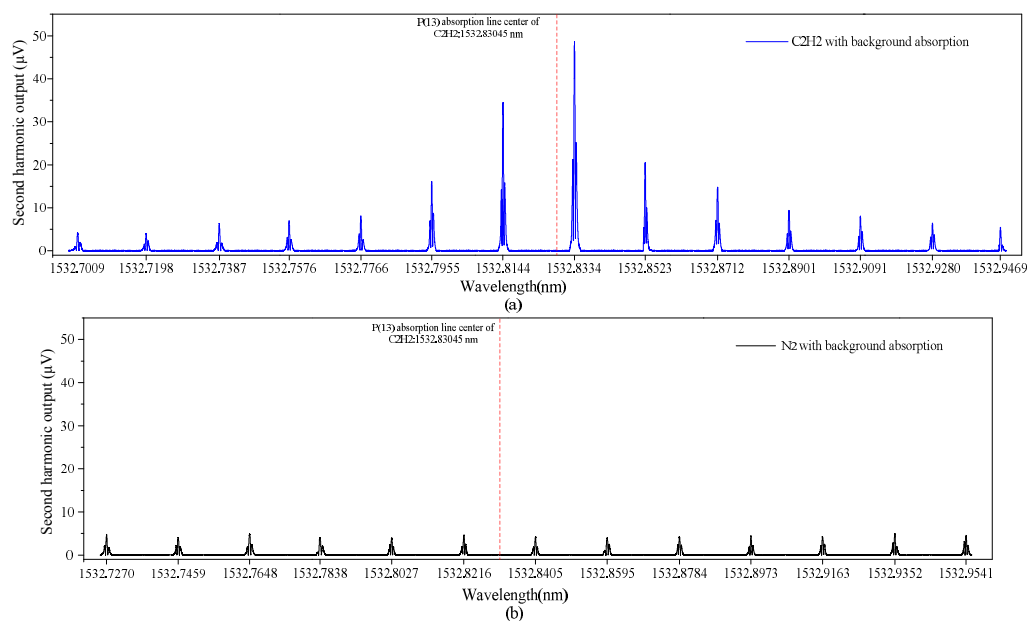


Fig. 7.5 Second harmonic lock-in output when pump laser is tuned across the P(13) line of acetylene and the corresponding cavity resonances. The gas cell is filled with (a) 100 ppm acetylene balanced by nitrogen and (b) nitrogen, respectively.

In order to obtain the maximal PT signal at the absorption center of 1532.83 nm in Figure 7.5, a small DC voltage (~ 1.5 V in our experiment) is applied to the PZT to tune the cavity length of the resonating microcell, so that one resonance which is located near 1532.83 nm can be made to align precisely to the center of the absorption line, indicated as Resonant A in Figure 7.3. Figure 7.6 (a) shows the second harmonic output when pump laser is tuned across the Resonant A at the center of the absorption line when the gas cell is filled with 100 ppm acetylene. Figure 7.6 (b) shows the second harmonic output when pump laser is tuned across the one of the cavity resonances near the absorption line when the gas cell is filled with nitrogen. The peak values of the second harmonic signal in Figure 7.6 (a) and (b) are $52.0 \mu\text{V}$ and $4.3 \mu\text{V}$, respectively, so the PT signal induced by acetylene absorption is $\sim 47.7 \mu\text{V}$. The second harmonic lock-in output

when the pump is tuned to the off cavity resonance and the probe is operating at the maximum slope of the cavity resonance is shown in Figure 7.6 (c). The standard deviation (s.d.) of the noise over ~ 6.5 -min duration is $0.06 \mu\text{V}$, not much larger than the noise level when the pump is off ($0.05 \mu\text{V}$), giving a signal to noise ratio (SNR) of 795. The lower detection limit for a SNR of unity is estimated to be 126 ppb in terms of noise equivalent concentration (NEC) for a detection bandwidth of 0.031 Hz.

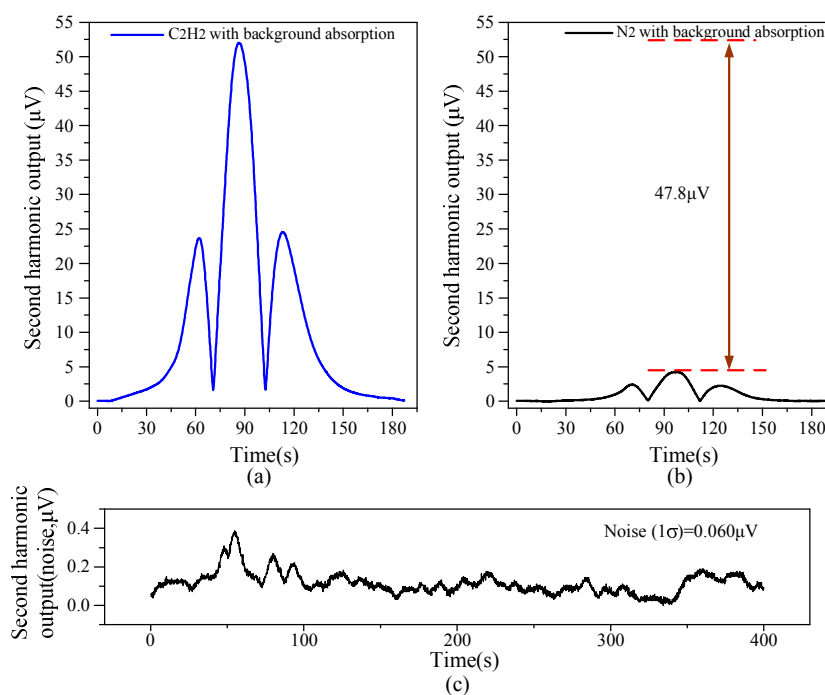


Fig. 7.6 (a) Second harmonic output when pump laser is tuned across the cavity resonance at the center of the absorption line when the gas cell is filled with 100 ppm acetylene. (b) Second harmonic output when pump laser is tuned across the one of the cavity resonances near the absorption line when the gas cell is filled with nitrogen. (c) Second harmonic output when the pump is tuned to the off cavity resonance.

Figure 7.7 (a) shows the peak values of the second harmonic signal in Figure 7.5 (a), and Figure 7.7 (b) shows the normalized peak values in Figure 7.5 (a) combined with the peak value in Figure 7.6 (a). The blue squares indicate the corresponding normalized peak values and the red dashed line is the Lorentz fitting of the normalized peak values while the black solid line is the normalized P(13) absorption line of acetylene based on

HITRAN 2004 database [5]. The Lorentz fitting of the peak values is in agreement with the acetylene absorption line, indicating that the second harmonic signal is induced by acetylene absorption.

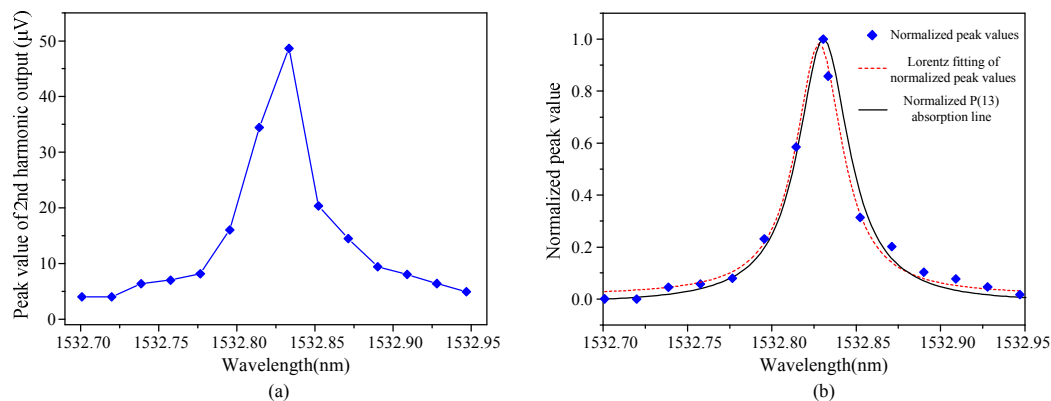


Fig. 7.7 (a) The peak values of the second harmonic signal in Fig. 7.5 (a). (b) The normalized peak values in Fig. 7.5 (a) and Fig. 7.6 (a). Blue squares: the normalized peak values; red dashed line: Lorentz fitting of the normalized peak values; Black solid line: normalized P(13) absorption line of acetylene.

Figure 7.8 (a) shows the second harmonic lock-in outputs (signal) for different pump power levels delivered to the resonating microcell when the pump wavelength was tuned across Resonance A at the center of the P(13) absorption line of acetylene. The peak values of second harmonic signal and the s.d. of the noise for different pump power levels are shown in Figure 7.8 (b). The signal and noise values are shown in red squares and blue circles respectively, showing that the second harmonic signal increases approximately linearly with pump power, while the noise level shows little variation.

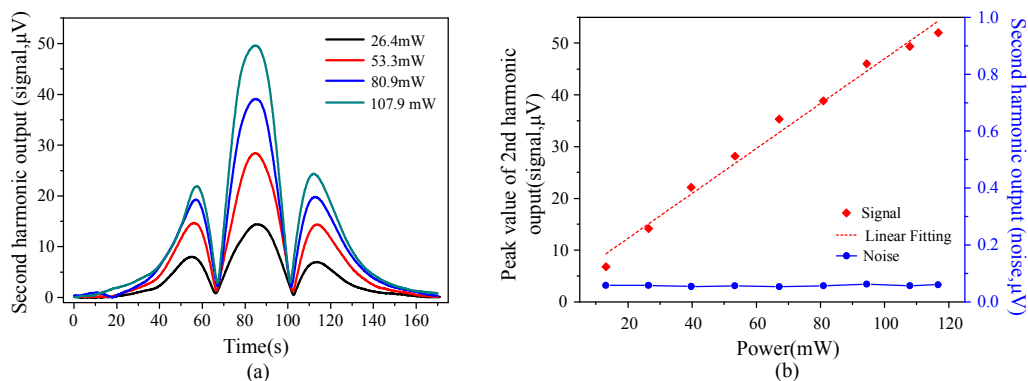


Fig. 7.8 (a) The second harmonic outputs (signal) for different pump power levels delivered to the HC-PBF cavity when the pump wavelength was tuned across the cavity resonance at the center of P(13) absorption line. (b) The peak values of second harmonic signal (red squares) and the s.d. of the noise (blue circles) as functions of pump power level.

7.3.2.2 Cavity enhancement for the probe beam operating at different slope points of the cavity resonance

As mentioned earlier, the wavelength of the probe laser should be operating at the maximum slope point of the cavity resonance to maximize the PT signal. We now investigate and compare the performances of the gas detection system when the wavelength of probe beam is operating at different slope points of the cavity resonance. As shown in Figure 7.9, the wavelength of the probe beam will be operating at five different points (Point 1-5). Among these points, Point 5 is the maximum slope point, while Point 2 is the minimum slope point and Point 1 is the zero slope point. The experimental system is the same with the setup shown in Figure 7.4 but the wavelength of the probe beam was tuned from Point 1 to Point 5 according to the DC voltage output from the oscilloscope in Figure 7.4, while the modulated pump beam is scanned across Resonance A at the center of absorption line.

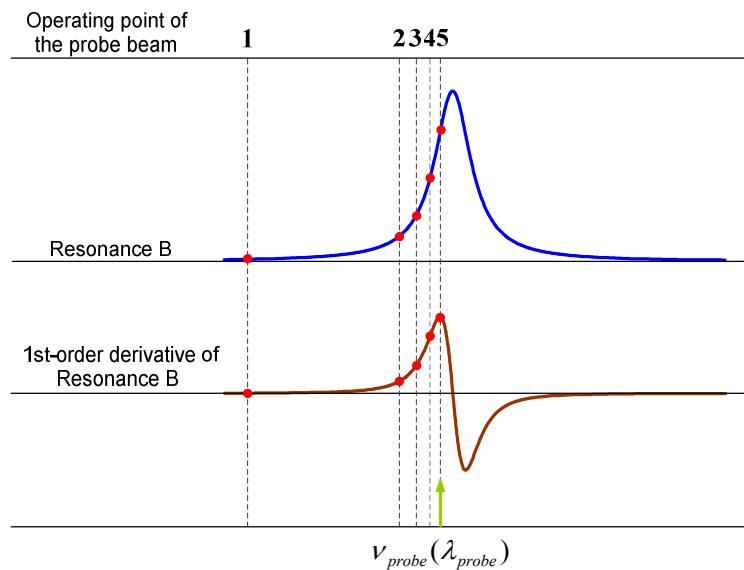


Fig. 7.9 Schematic showing the wavelength of the probe beam operating at five different points (Point 1-5). Blue line: cavity resonance at 1550 nm (Resonance B); Brown line: 1st order derivative of Resonance B.

Figure 7.10 (a) shows the second harmonic lock-in outputs (signal) for the wavelength of the probe beam operating at five different points (1-5) when the pump wavelength was tuned across Resonance A at the center of P(13) absorption line. The peak values of the second harmonic signal when the probe wavelength is operating at Point 5 and Point 2 are 52.0 μV and 2.5 μV , respectively, showing ~ 20 times enhancement when the probe wavelength is operating at the maximum slope point of the cavity resonance. The peak values of second harmonic signal and the s.d. of the noise when the probe beam operating at Points 1 to 5 are shown in Figure 7.10 (b). The green squares show the peak values of the second harmonic signals and blue circles indicate the s.d. of the noise values for different operating points. From Figure 7.10 (b), the second harmonic signals increase with the slope value of the cavity resonance while the noise level remained in a relatively plane level.

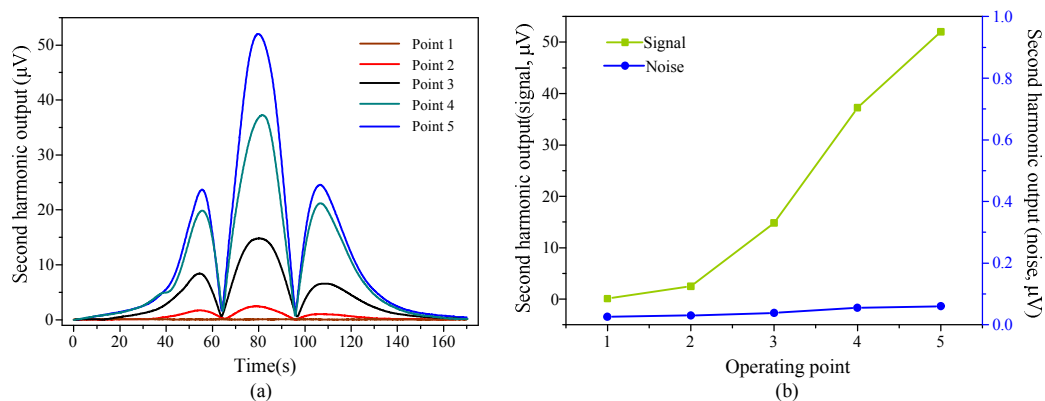


Fig. 7.10 (a) The second outputs (signal) for the wavelength of the probe beam operating at five different points (1-5) when the pump wavelength was tuned across Resonance A at the center of P(13) absorption line. (b) The peak values of second harmonic signal (green squares) and the s.d. of the noise (blue circles) when the probe wavelength operating at different points.

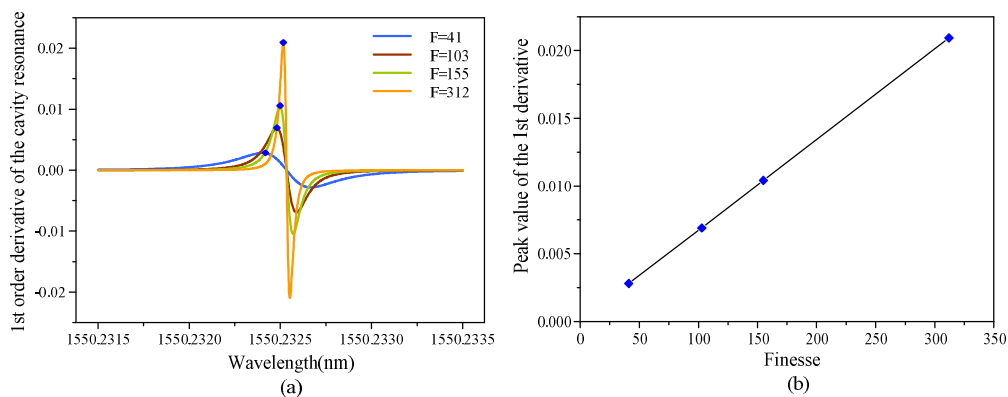


Fig. 7.11 (a) Theoretical calculation of the 1st order derivative of a resonating HC-PBF microcell with different finesse. (b) Peak values of 1st order derivative as functions of cavity finesse.

Moreover, Figure 7.11 shows the theoretical calculation of the 1st order derivative of a resonating HC-PBF microcell with different values of cavity finesse. The cavity length is set to be 6.2 cm. Figure 7.11 (a) shows the FWHM of the cavity becomes narrow and Figure 7.11 (b) shows the maximum values of 1st order derivative indicated as the blue squares increase with the cavity finesse. For a cavity finesse of 312, the peak value is ~ 8.4 times higher than the finesse of 41. So the current gas detection sensitivity

may be improved to ~15 ppb when using a resonating HC-PBF microcell with finesse of 312.

7.3.2.3 Cavity enhancement for the intracavity build-up intensity of the pump beam

According to the Eq. (7.3) from Section 7.2, the intracavity build-up intensity will be enhanced by a factor of $E=t(F/\pi)^2$, which is related to the transmission coefficient t of the mirror and the cavity finesse F . We also carried out investigation on the cavity enhancement for the intracavity build-up intensity of the pump beam. For the current resonating HC-PBF microcell, the relevant parameters can be calculated by Eq. (3) and are listed in Table 7.1.

Table 7.1. Parameters of the current resonating HC-PBF microcell

On-resonance cavity transmission T_{res}	Reflection coefficient of the mirror r	Cavity finesse F
0.075	0.928	45
Transmission coefficient of the mirror t	Cavity enhancement factor E	
0.01976	4	

For the current resonating HC-PBF microcell, the cavity enhancement factor E is 4 which may be induced by the loss between the misalignment of mirror and the HC-PBF. However, we can still reduce the loss by using an optimal alignment technique or using concave mirrors which can reduce the light dispersion before entering into the HC-PBF [6]. Let us consider a simple situation that the loss between two mirrors and HC-PBF is greatly reduced, then it becomes a simple extrinsic fiber Fabry Perot cavity made by aligning two pieces of SMFs with mirrored ends, as shown in Figure 7.12. The cavity transmission can be measured by connecting both SMF pigtailed of the cavity to a broadband light source (BBS) and an optical spectrum analyzer (OSA), respectively.

Figure 7.13 shows the measured transmission of such a cavity. The FSR is measured to be 83.2 nm, corresponding to a cavity length of 13.5 μm . The cavity finesse is estimated to be 75 at the wavelength of 1472.8 nm and 314 at the wavelength of 1556 nm. The on-resonance cavity transmission T_{res} is measured to be ~ 0.72 . Similarly, for a resonating HC-PBF microcell, it is still possible to achieve a finesse of ~ 300 when using an optimal alignment technique. For a finesse of 307, the enhancement factor E as a function of on-resonance cavity transmission T_{res} can be calculated and shown in Fig 16(a). For $T_{\text{res}}=0.72$ and $F=307$, the enhancement factor E would be 84 for a resonating HC-PBF microcell. We can infer that the lower detection limit for gas detection would be below ~ 6 ppb with an enhancement factor E of 84.

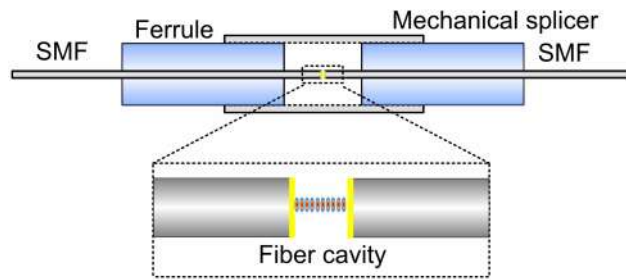


Fig. 7.12 Schematic of an extrinsic fiber Fabry Perot cavity.

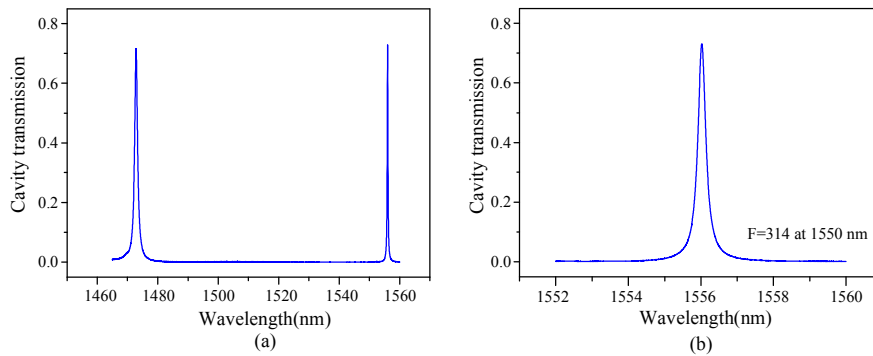


Fig. 7.13 The measured transmission of an extrinsic F-P cavity at (a) wavelength of 1465~1560 nm and (b) wavelength of 1552~1560 nm.

Figure 7.14 shows the calculated relationship between the enhancement factor E and the cavity finesse for a given T_{res} of 0.9. This result clarifies that the cavity finesse

does play an important role in the enhancement factor of the intracavity build-up intensity. When the cavity finesse increases to 1500, the enhancement factor E would become higher than 500, which would be a huge enhancement for the intracavity build-up intensity. For example, if the input power is 1 mW, the intracavity build-up power would become 500 mW, which is very important for photothermal gas detection technique since the PT signal is proportional to the optical intensity inside the gas cell. Therefore, the performances of the PT gas sensor may be improved by increasing the cavity finesse to achieve sub-ppb level detection sensitivity.

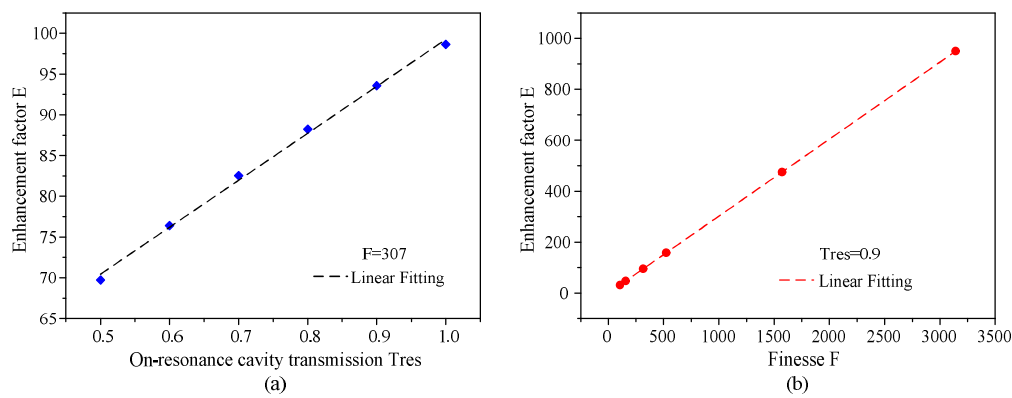


Fig. 7.14 (a) The calculated enhancement factor E as a function of on-resonance cavity transmission T_{res} for a given finesse of 307. (b) The calculated relationship between the enhancement factor E and the cavity finesse for a given T_{res} of 0.9.

7.3.3 Comparison with a resonating HC-PBF photonic microcell based on DAS

As shown in Chapter 6, a resonating HC-PBF photonic microcell based on DAS exhibits a detection limit of ~ 7 p.p.m. Compared with the same microcell based on PT effect, the detection sensitivity of 126 ppb is 1-2 orders magnitude better than the resonating gas cell based on DAS, showing an enhancement based on the PT effect.

7.4 Summary

In this chapter, a resonating HC-PBF photonic microcell for high sensitivity gas detection based on PT spectroscopy is introduced, including the basics of the cavity enhanced PT spectroscopy and the gas experiments results. With a cavity length of 6.2 cm and finesse of 45 for pump beam and 41 for probe beam, we demonstrated acetylene detection with a detection limit of ~ 126 ppb, 1-2 orders of magnitude better than a high finesse HC-PBF sensor with a similar length of 9.4 cm based on direct absorption [7]. The cavity enhancement of such a high finesse resonating HC-PBF gas cell can simultaneously amplify the intracavity build-up intensity for the pump beam inside the HC-PBF and improve the slope of the operating point for the probe beam by a factor proportional to the cavity finesse.

The performance of all fiber double-cavity-enhanced photothermal gas sensor can be further improved by using optimal alignment techniques to improve the enhancement factor E for the intracavity build-up intensity within the resonating waveguide. Theoretical calculation shows that the lower detection limit for gas detection would become ~ 6 ppb for an enhancement factor E of 84. The double-cavity-enhanced PT gas sensor enables higher intracavity build-up intensity and allows us to use shorter length of HC-PBF, which can be used to develop all-fiber gas sensors with high sensitivity and fast response.

References of Chapter 7

- [1] R. Van Zee and J. P. Looney, Cavity-enhanced spectroscopies (Academic Press, 2003).
- [2] L. S. Ma, J. Ye, P. Dubé, and J. L. Hall, "Ultrasensitive frequency-modulation spectroscopy enhanced by a high-finesse optical cavity: theory and application to overtone transitions of C_2H_2 and C_2HD ," J. Opt. Soc. Am. B 16, 2255–2268 (1999).

-
- [3] A. Foltynowicz, Fiber-laser-Based Noise-Immune Cavity-Enhanced Optical Heterodyne Molecular Spectrometry, Doctoral Thesis, Umeå University, Sweden 2009.
- [4] W. Jin, Y. Cao, F. Yang, and H. L. Ho, “Ultra-sensitive all-fibre photothermal spectroscopy with large dynamic range,” *Nat. Commun.* 6, 6767 (2015).
- [5] L. S. Rothman, D. Jacquemart, A. Barbe, D. C. Benner, M. Birk, L. Brown, M. Carleer, C. Chackerian, Jr, K. Chance, L. Coudert, V. Dana, V. Devi, J. Flaud, R. Gamache, A. Goldman, J. Hartmann, K. Jucks, A. Maki, J. Mandin, S. Massie, J. Orphal, A. Perrin, C. Rinsland, M. Simth, J. Tennyson, R. Tolchenov, R. Toth, J. Auwera, P. Varanasi, and G. Wagner, “The HITRAN 2004 molecular spectroscopic database,” *J. Quant. Spectrosc. Radiat. Transfer.* 96, 139–204 (2005).
- [6] D. Hunger, T. Steinmetz, Y. Colombe, C. Deutsch, T. W. Hänsch, and J. Reichel, “A fiber Fabry–Perot cavity with high finesse,” *New J. Phys.* 12, 065038 (2010).
- [7] Y. Tan, W. Jin, F. Yang, Y. Qi, C. Zhang, Y. Lin, and H. L. Ho, “Hollow-core fiber-based high finesse resonating cavity for high sensitivity gas detection,” *J. of Lightwave Technol.* 35, 2887–2893 (2017).

Chapter 8

Conclusion and future work

8.1 Conclusion

In this thesis, several all optical fiber photothermal spectroscopic sensors have been demonstrated to significantly enhance gas detection sensitivity. The contributions of this thesis are listed as follows.

(1) We introduced an acoustic detector based on the low finesse F-P cavity with multilayer graphene diaphragm, including its fabrication, the sensitivity and frequency response of the acoustic detector. By operating at one of the mechanical resonances of the 2.5 mm-diameter diaphragm, the sensitivity for acoustic detection is enhanced and a noise equivalent minimum detectable pressure of $\sim 2 \mu\text{Pa}/\text{Hz}^{1/2}$ at 10.1 kHz is achieved. We also tested the long term stability of the acoustic detection system, and design a feedback loop control system to stabilize the operating Q -point in the interference spectrum.

(2) We demonstrated the acetylene detection based on the photoacoustic effect by using the fabricated acoustic detector in (1). By operating at the resonance of the nano-mechanical resonator, the SNR is enhanced, and a lower detection limit for acetylene with the NEC of ~ 120 ppb and NNEA of $9.782 \times 10^{-8} \text{ cm}^{-1}\text{WHZ}^{-1/2}$ are achieved. Theoretical calculation demonstrates that the performances of the PA gas sensor can be further enhanced by increasing the Q -factor value at lower pressures to achieve ppb level detection sensitivity.

(3) We presented an all-fiber resonating HC-PBF photonic microcell by sandwiching a piece of HC-PBF between two SMFs with mirrored ends. The high

reflectivity mirrors (~99%) form high finesse Fabry-Perot cavities. We have made several HC-PBF Fabry-Perot gas cells with length from 5 to 10 cm and cavity finesse from 50 to well over 100, achieving effective path length of several meters. Such microcells achieve long effective path length with short length of HC-PBFs, which can be used for gas detection with high sensitivity and fast response.

(4) With a cavity length of 9.4 cm and finesse of 68, we demonstrated acetylene detection with a detection limit of ~7 p.p.m, 1-2 orders of magnitude better than a single-path HC-PBF sensor with a similar length and comparable with that of a 13-m-long HC-PBF sensor. Comparing with the single-path (without mirrors) HC-PBF gas cells of a similar length, the high finesse HC-PBF Fabry-Perot cavity reduces significantly the effect of modal interference noise on gas detection.

(5) We demonstrated a resonating HC-PBF photonic microcell for high sensitivity gas detection based on PT spectroscopy. With a cavity length of 6.2 cm and finesse of 45 for pump beam and 41 for probe beam, we demonstrated acetylene detection with a detection limit of ~126 ppb, 1-2 orders of magnitude better than a high finesse HC-PBF sensor with a similar length of 9.4 cm based on direct absorption [19].

8.2 Future work

We have demonstrated all optical fiber gas sensors based on photothermal spectroscopy to significantly enhance gas detection sensitivity. Several suggestions given as follows can be further investigated.

(1) The performance of optical fiber PAS system for gas detection can be further improved by increasing the power of the pump beam since the PA signal is proportional to the pump power level. Using a larger-diameter graphene nano-mechanical resonator can also increase the acoustic detection sensitivity. A resonant PA cell with its acoustic

resonant frequency matched to that of the nano-mechanical resonator will also be used to further enhance the gas detection sensitivity.

(2) We can infer that the Q -factor of the graphene nano-mechanical resonator in vacuum would become larger, then the performances of the PA gas sensor would be improved to ppb level detection sensitivity.

(3) For the resonating HC-PBF photonic microcell, the value of finesse is in the level of ~ 100 , so we will improve the cavity finesse by using mirrors with higher sensitivity of 99.99% and using an optimal alignment technique. Alternatively, fabricating a concave mirror on the endface of the SMF pigtail can also improve the cavity finesse.

(4) For the cavity-enhanced photothermal gas sensor with a resonating HC-PBF photonic microcell, a servo system by locking the cavity resonance precisely and stably to the center of a gas absorption line will be used to reduce the fluctuation in the gas detection system, so that the performance for gas detection can be further improved.